

# Hall Resistance Characterization of Thermoelectric Materials; Subgap Leakage Measurement of Josephson Junctions

by

Tianze Zou

A thesis  
presented to the University of Waterloo  
in fulfillment of the  
thesis requirement for the degree of  
Master of Science  
in  
Physics (Nanotechnology)

Waterloo, Ontario, Canada, 2020

© Tianze Zou 2020

## **Author's Declaration**

I hereby declare that I am the sole author of this thesis. This is a true copy of the thesis, including any required final revisions, as accepted by my examiners.

I understand that my thesis may be made electronically available to the public.

## Abstract

The thesis has two parts. The first part is the Hall measurement of thermoelectric materials which are promising energy sources in the future. By characterizing the Hall resistance at different environments, their charge carrier density and mobility can be calculated, which is important to explain their unique electrical and thermal properties at different temperatures. However, due to the geometry of the samples, the strong thermoelectric properties of the materials, and some electrical noise sources of the experimental setup, the measurement uncertainty is questionable.

In this thesis, a DC Hall measurement setup and an AC Hall measurement setup are built which are designed for the electrical conductivity measurement and the Hall resistance measurement of bulky bar samples made of thermoelectric materials. The measurement uncertainty caused by different noise sources are characterized and then compared with the theoretical predictions. The conclusion is that both setups have their unique advantages and limitations. It is found that the AC method has higher measurement speed than the DC method. The usage of a low-noise transformer in the AC Hall measurement and the PI temperature control system can reduce the measurement uncertainty.

The second part of the thesis is about the subgap leakage measurement of  $Nb/AlO_x/Nb$  Josephson junctions which are important in the applications of quantum computing. The subgap leakage current at low temperature is caused by the intrinsic defects of the junctions, which limits their behaviour. Therefore, the superconducting properties of the junctions at low temperatures need to be characterized by the subgap leakage measurement.

In this thesis, the junctions are mounted in a dry adiabatic demagnetization refrigerator(ADR) and cooled down to as low as  $130\text{ mK}$ . A voltage-bias circuit and a current-bias circuit for the measurement are designed and used. A NbTi superconducting magnet is made to provide magnetic fields to suppress the supercurrent of the junctions. The I-V curves of some junctions are measured which show the information of their subgap regions, the temperature dependence of their subgap leakage currents and their response to the magnetic field. The conclusion is that the subgap leakage measurement can be done with this low-temperature measurement setup. Details of the design are described in this thesis.

## Acknowledgements

The first person I want to thank is my supervisor Jan Kycia who gives me a lot of support, not only in research but also in my experience being an international student in Canada. I want to thank my group members Nick Cockton and Taylor Fraser who I enjoy working together with. I want to thank former group members Jeff Mason, David Pomaranski and Cliff Plesha who shared with me their knowledge and taught me skills. I also want to thank to Hiruy Haile who helps me in the machine shop.

I want to thank my committee members Holger Kleinke, Adrian Lupascu and Zbig Wasilewski for giving me a lot of advice. I want to thank Holger's group members Parisa Jafarzadeh, Leila Macario and Yixuan Shi who provided me with thermoelectric samples and gave me support in the Hall measurement. I thank Loren Swenson and his research group from D-wave inc., and Alan Kleinsasser from JPL for giving our group a good opportunity to start the subgap leakage measurement project and providing devices.

Finally, I would like to say thank you again to all the people who made this thesis possible. I could not push forward without your help.

## **Dedication**

This is dedicated to the people who I work together with, and to my parents who support me all the time.

# Table of Contents

List of Figures	ix
List of Tables	xv
<b>I Hall resistance characterization of thermoelectric materials</b>	<b>1</b>
<b>1 Hall measurement Introduction</b>	<b>2</b>
1.1 Hall measurement . . . . .	2
1.2 Thermoelectric materials . . . . .	3
1.2.1 Introduction of thermoelectric materials . . . . .	3
1.2.2 Information from Hall measurement . . . . .	4
1.2.3 Information of Samples . . . . .	6
1.3 Review of Hall measurement setups . . . . .	6
1.3.1 Literature review . . . . .	6
1.3.2 Thanh Lê's Hall measurement setup . . . . .	8
1.4 Challenges . . . . .	8
1.5 Motivations . . . . .	9
<b>2 Hall measurement Setup</b>	<b>10</b>
2.1 Sample holder . . . . .	10

2.2	Temperature control . . . . .	13
2.3	DC Hall measurement setup . . . . .	15
2.4	AC Hall measurement setup . . . . .	18
2.5	Measurement steps and measurement speed . . . . .	23
<b>3</b>	<b>Measurement errors and the noise</b>	<b>24</b>
3.1	Possible sources of errors in the Hall measurement . . . . .	24
3.2	Noise level . . . . .	28
3.2.1	Introduction to the noise spectrum . . . . .	28
3.2.2	Spectrum analyzer . . . . .	30
3.2.3	Spectrum of Hall voltage leads . . . . .	31
3.2.4	Conclusions from the spectrum . . . . .	39
<b>4</b>	<b>Hall measurement results and discussion</b>	<b>40</b>
4.1	Temperature dependence of the electrical resistivity . . . . .	40
4.2	DC Hall measurement . . . . .	42
4.2.1	Noise from thermal EMF . . . . .	42
4.2.2	DC Hall measurement - before fixing the GPIB problem . . . . .	46
4.2.3	DC Hall measurement - after fixing the GPIB problem . . . . .	49
4.3	AC Hall measurement . . . . .	52
4.3.1	AC measurement with the transformer . . . . .	52
4.3.2	AC Hall measurement without the transformer . . . . .	60
4.4	Discussions . . . . .	63
4.4.1	Comparison of the three Hall measurement methods . . . . .	63
4.4.2	Normalized Hall resistance $R_H$ . . . . .	64
4.4.3	Measurement speed . . . . .	66
4.5	Summary . . . . .	66
4.6	Conclusions . . . . .	67
4.7	Future work . . . . .	67

<b>II</b>	<b>Subgap Leakage measurement of Josephson Junctions</b>	<b>69</b>
<b>5</b>	<b>Introduction</b>	<b>70</b>
5.1	Introduction of Josephson junctions and subgap leakage measurement . . .	70
5.2	Subgap leakage current . . . . .	71
5.3	I-V curves of Josephson junctions . . . . .	72
5.3.1	Current bias . . . . .	72
5.3.2	Voltage bias . . . . .	74
5.3.3	Magnetic suppression . . . . .	77
5.4	Temperature dependence . . . . .	78
5.5	Motivation and challenges . . . . .	78
<b>6</b>	<b>Subgap leakage measurement setup</b>	<b>80</b>
6.1	Sample preparation . . . . .	80
6.2	Current bias circuit . . . . .	83
6.3	Voltage bias circuit . . . . .	84
6.3.1	Electrochemical effects . . . . .	85
<b>7</b>	<b>Subgap leakage measurement: results and discussions</b>	<b>86</b>
7.1	Current bias versus voltage bias . . . . .	86
7.2	Magnetic suppression . . . . .	91
7.3	Temperature dependence . . . . .	93
7.4	Summary . . . . .	97
7.5	Future work . . . . .	97
	<b>References</b>	<b>98</b>
	<b>Glossary</b>	<b>103</b>

# List of Figures

1.1	The Hall effect illustration. When current $I_x$ is along x-axis and magnetic field $B$ is along z-axis, the Hall voltage is along y-axis. . . . .	3
1.2	Carrier concentration of doped thermoelectric material $Mg_{2.08}Si_{0.4-x}Sn_{0.6}Sb_x$ at high temperature[6]. Varying $x$ changes the composition and temperature dependence of the charge carrier concentration of the compound. . . . .	5
1.3	The sample with rectangular bar geometry in traditional Hall measurement. [37] Lead A and F are for the current; lead C and D are for the Hall voltage measurement; lead B and E are for the electrical conductivity measurement. . . . .	7
2.1	Hall measurement sample holder box illustration. The aluminum sample holder and the six pogo pins are mounted at the center of the box. . . . .	11
2.2	Picture of the Hall measurement sample holder box and the sample holder. . . . .	12
2.3	Illustration of the PI temperature control system run by a LabVIEW program. The Peltier cooler. A temperature can be set from 15 °C to 30 °C with an uncertainty of $\pm 0.05$ °C. . . . .	14
2.4	DC Hall measurement setup illustration.[25] . . . . .	16
2.5	Example of voltage data from a measurement cycle in DC Hall measurement. The five voltage steps correspond to the cycle: $(+B, +I) \rightarrow (+B, -I) \rightarrow (-B, +I) \rightarrow (-B, -I) \rightarrow (0, 0)$ . It takes about five minutes per cycle . . . . .	17
2.6	The typical frequency response curves of PAR 190 transformer.[3] $P_1S_3$ corresponds to the $\times 1000$ gain, and $P_2S_3$ corresponds to the $\times 100$ gain. $R_1$ is the loading impedance of the transformer. . . . .	19
2.7	AC Hall measurement setup illustration: (a) without transformer, (b) with transformer . . . . .	20

2.8	Example of the voltage signal read from the AC Hall measurement. The voltage steps in the graph from left to right correspond to $+B \rightarrow -B \rightarrow 0$ . Every three steps is a measurement cycle which takes about 1 minute. . . .	22
2.9	Experiment steps of the Hall measurements and the measurement speed of each step. If taking the same amount of $R_H$ data points, the AC Hall measurement is about four times faster than the DC Hall measurement with the same sensitivity. . . . .	23
3.1	Illustration of misalignment voltage $V_M$ caused by imperfect alignment of two Hall voltage leads. . . . .	26
3.2	Temperature difference through the circuit may generate thermal EMF, $V_T$ , by Seebeck effect. The sources of $V_T$ are the thermoelectric sample and the electrical joints through the circuit. . . . .	27
3.3	Typical voltage spectrum showing the noise at certain frequencies[19]. . .	29
3.4	The circuit illustration of measuring noise spectrum from a sample. The signal is amplified by the PAR 113 preamplifier with $G=100$ and DC coupling, and then sent to a HP 3562a spectrum analyzer. . . . .	30
3.5	The background spectrum of the Ks sample mounted on the sample holder compared to that of a $10 \Omega$ resistor. The signal from the sample is amplified by the PAR 113 preamplifier with $G = 100$ . The $1/f$ noise is caused by the PAR 113. . . . .	32
3.6	The spectrum of the Ks sample if the magnet power supply is on or not, and if the PI control is running or not. The harmonic peaks are significant when magnet power supply and PI control are running at the same time. .	33
3.7	The spectrum of graphite sample when observing GPIB low frequency noise. The harmonic peaks (green line) proves the sample is not the noise source. Unplugged the BNC-2110/NI-PCI 6251 DAQ lowered the noise. . . . .	35
3.8	The spectrum of Ks sample after fixing the GPIB problem. The scan frequency combines $0.01 \sim 1 Hz$ and $1 \sim 50 Hz$ . The three lines overlap each others, which shows the temperature drift around the sample does not cause extra $1/f$ noise. . . . .	36
3.9	The spectrum of Ks sample when running the DC Hall measurement program. Switching magnetic field caused significant magnetic EMF noise peaks at $f = 20 Hz$ and $40 Hz$ . . . . .	37

3.10	The spectrum of Ks sample when running the AC Hall measurement. Switching magnetic field causes significant noise with $f = 20 \text{ Hz}$ . . . . .	38
4.1	The electrical resistivity of sample Ks at $T=20.5 \text{ }^\circ\text{C}$ with different excitation currents. $\rho$ changes quickly when $I > 15 \text{ mA}$ , so $I = 12 \text{ mA}$ was chosen as the best excitation current. . . . .	41
4.2	Thermal EMF measurement of sample Ks at different temperatures. $\Delta T = T_{\text{room}} - T_{\text{sample}}$ and $T_{\text{room}} = 20.85 \text{ }^\circ\text{C}$ . In the lower part, $V_{\text{raw}}=V_{\text{T}}+V_{\text{offset}}$ which is shown as purple points. The purple line is the smoothed line calculated from the average of every adjacent 50 data points. . . . .	43
4.3	Thermal EMF measurement of sample Ks at $20.0 \text{ }^\circ\text{C}$ , with $I = 0$ and $B = 0$ . The figure is the zoom-in version of 30 ~ 46 min of Fig: 4.2. Ideally, the $V_{\text{H}}$ should be zero because of no excitation current or magnetic field being applied; however, the calculated $V_{\text{H}}$ are in $\pm 2 \text{ nV}$ due to the drifting $V_{\text{T}}$ . . . . .	44
4.4	$V_{\text{T}}$ of three samples, measured by Agilent 34420a voltmeter. $\Delta T = T_{\text{room}} - T_{\text{sample}}$ . Thermoelectric sample Ks has higher $V_{\text{T}}$ than non-thermoelectric solder sample and graphite sample. The $V_{\text{T}}$ when using non-thermoelectric samples may be caused by the thermocouple effect of the contacts within the leads. . . . .	45
4.5	Voltage signal measured in DC Hall measurement. The PI temperature control did not work in the first 100 minutes, and then started to control $T$ to $26.0 \text{ }^\circ\text{C}$ . . . . .	46
4.6	Calculation result of the Hall measurement in Fig: 4.5 before fixing the GPIB problem. (a)-(d) are the Hall voltage $V_{\text{H}}$ , misalignment voltage $V_{\text{M}}$ and thermal EMF $V_{\text{T}}$ of the DC Hall measurement. (e) is the temperature in the sample holder box which rises in the first 100 minutes; the PI temperature control starts to work at $t = 100 \text{ min}$ which stabilizes $T$ to be $26 \text{ }^\circ\text{C}$ . (f) shows the $R_{\text{H}}$ during the measurement. (b) and (f) shows that in this situation, using PI temperature control causes higher measurement uncertainty than not using it. . . . .	48
4.7	Raw voltage data of DC Hall measurement after fixing the GPIB problem. The temperature was controlled to $19.8 \text{ }^\circ\text{C}$ before time $t=150 \text{ min}$ , and the temperature control was off after $t=150 \text{ min}$ . The $V_{\text{raw}}$ spike at $150 \text{ min}$ was due to suddenly turning off the temperature control . . . . .	50

4.8	<p>Voltages in the DC measurement, with and without temperature control after fixing the GPIB problem. (a)-(d) are the <math>V_H</math>, <math>V_M</math> and <math>V_T</math> of the DC Hall measurement. The spike was caused by turning down the PI temperature control. (e) the temperature was at <math>20\text{ }^\circ\text{C}</math> in the first 150 minutes with the temperature on and rose to <math>30\text{ }^\circ\text{C}</math> the temperature control off. (f) shows <math>R_H = (8.43 \pm 0.0092) \times 10^{-8}\text{ V.m/AT}</math> with the temperature control on and <math>R_H = (8.39 \pm 0.0094) \times 10^{-8}\text{ V.m/AT}</math> without the temperature control. The temperature control did not improve the measurement uncertainty because of the drifting <math>V_T</math> . . . . .</p>	51
4.9	<p>The raw voltage data of the AC Hall measurement with the transformer. (a) and (b) show the glitches from the magnetic EMF; (c) shows the voltage graph after cleaning the glitches by programming. <math>V_{\text{offset}} = +7.697\text{ }\mu\text{V}</math> . . . . .</p>	53
4.10	<p>Voltage measured in the AC Hall measurement of sample Ks with the transformer, <math>T=23\text{ }^\circ\text{C}</math> under the PI temperature control. There were 100 measurement cycles; it took 70 seconds to run each cycle. (a) is the current, (b) and (d) are the voltage <math>V_x - V_{\text{offset}}</math> when the magnetic fields were +B and -B; (c) is the calculated Hall voltage <math>V_H</math>; (e) is <math>T_s</math>; (f) is <math>R_H = (7.996 \pm 0.001) 10^{-8}\text{V.m/AT}</math>. . . . .</p>	55
4.11	<p>Temperature dependence of <math>R_H</math>, <math>n</math>, <math>\sigma</math>, and <math>\mu</math> in the room temperature range. <math>R_H</math> and <math>n</math> are temperature independent; <math>\sigma</math> and <math>\mu</math> change linearly along with temperature. . . . .</p>	56
4.12	<p>The voltage data of the AC Hall measurement with the transformer but without temperature control. The voltage shown in the figure is after taking the transformer <math>\times 100</math> gain into account. The voltage drifted about <math>+200\text{ nV}</math> in 120 minutes. <math>V_{\text{offset}} = +10.84\text{ }\mu\text{V}</math>. . . . .</p>	58
4.13	<p>Details of the AC Hall measurement without temperature control. (a) is the excitation current. (b) and (d) are the voltage data when magnetic fields were +B and -B. (c) is the calculated Hall voltage. (e) is the temperature, <math>T_s</math>, during the test; it kept below <math>20.5\text{ }^\circ\text{C}</math> in the first 40 measurement cycles and rose quickly to <math>20.5\text{ }^\circ\text{C}</math> due to the heat from the magnet. (f) <math>R_H = (8.25 \pm 0.001) \times 10^{-8}\text{V.m/AT}</math> in the first 40 measurement cycles, and <math>R_H = (8.25 \pm 0.002) \times 10^{-8}\text{V.m/AT}</math> in the rest 60 measurement cycles. The temperature drift increased the uncertainty of <math>R_H</math>. . . . .</p>	59
4.14	<p>Voltage in the AC Hall measurement without the transformer. <math>T = 23.0\text{ }^\circ\text{C}</math> by the PI temperature control. <math>V_{\text{offset}} = -7.858\text{ }\mu\text{V}</math>. In this figure, the voltage noise is more significant than that in Fig: 4.9. . . . .</p>	61

4.15	The AC Hall measurement without the transformer. (a) is the excitation current. (b) and (d) are the voltage data when the magnetic fields were $+B$ and $-B$ . (c) is the calculated Hall voltage. (e) is the temperature $T_s$ under temperature control during the test. (f) $R_H = (8.59 \pm 0.014) \times 10^{-8} V \bullet m/AT$	62
4.16	$(\Delta R_H/R_H)$ % of different measurements. The dash lines are the theoretical limit of the methods only considering the electronic noise from the electronics.	65
5.1	Hysteresis I-V curve of unshunted Josephson junctions.[44] The errors indicate how junction voltage $V$ change along with bias current $I$ .	73
5.2	subgap leakage curve of a Nb Josephson junction at $T = 0.8 K$ . Its critical current $I_c$ is changed by applied magnetic field. [31]	74
5.3	Typical 4.2 K I-V curves for (a) low critical current density $J_c$ , (b) high $J_c$ junctions and (c) Ohm's law prediction.[23]	75
5.4	Theoretical I-V characteristics used to describe the junctions: (a)an ideal tunnel junction; (b)a junction with pinholes; (c) Ohm's law.[23]	76
5.5	Maximum supercurrent of Josephson junctions suppressed by magnetic flux.[44]	77
5.6	Subgap leakage current temperature dependence in the experiment. [31] The curves are linear above $T = 1 K$ which follows the BCS theory prediction; they are flattened when $T < 1 K$ .	78
6.1	The copper sample holder, without(left) and with(right) the copper shield, for the subgap leakage measurement.	81
6.2	Experimental steps of subgap leakage measurement.	82
6.3	Current bias circuit of the subgap leakage measurement	83
6.4	Voltage bias circuit of the subgap leakage measurement	84
6.5	A dirty switch in the safety box covered by soldering flux. The red circle in the figure shows the dirty lead of the switch and the remaining flux	85
7.1	I-V curves of junction JJ1-0.4um at $T = 2.7 K$ and different magnetic fields, $B$ , measured by the current bias method. The curves are hysteretic. The critical current $I_c$ decreases when increasing $B$ .	87

7.2	I-V curves of junction JJ1-0.4um at $T = 2.7 K$ and different magnetic field, measured by the voltage bias method. The solid lines are from the experiment which are non-hysteresis. The dash lines are from the prediction of using current bias in the same experiment, which match the I-V curves in Fig: 7.1. . . . .	88
7.3	The log(I)-V curves of junction JJ1-0.4um at $T = 2.7 K$ by using the voltage bias method, which use the same data of Fig: 7.2. It shows that the subgap current is the lowest near $V_{junction} = 2.0 mV$ . When increasing the magnetic field, the height of the peaks decreases. . . . .	89
7.4	Normalized I-V curve of three Nb Josephson junctions on a same chip: junction-0.7um(blue), junction-0.8um(orange), and junction-1.0um(green). The curves are measured only when increasing the bias voltage $V_{junction}$ . The red dashed line represents Ohm's law. $T = 2.6 K, B = 0 mT$ . . . . .	90
7.5	The maximum supercurrent of junction JJ1-0.4um at 2.7 K, changed by the applied magnetic field $B$ . . . . .	91
7.6	The relationship between the maximum supercurrent and the magnetic flux of junction JJ1-0.4um at $T = 2.7K$ . The calculation is based on Eq. 5.5. . . . .	92
7.7	The I-V curves of junction JJ1-0.4um by voltage bias at $B=66 mT$ and different temperatures. The current at $V_{junction} = 0.5 mV$ was used to determine the subgap current, $I_{sg}$ . It is seen to stay at the same level, $1 pA$ , when $T < 1.0 K$ ; it is seen to increase along with temperature when $T > 1.0 K$ . The reason which causes peaks at $V_{junction} = \pm 0.25 mV$ and $\pm 0.25 mV$ is still not fully understood. . . . .	94
7.8	I-V curves of junction JJ2-4um by voltage bias at $B=74 mT$ and different temperature. The black arrows are the drift directions of the current along with the bias voltage method. . . . .	95
7.9	Temperature dependence curves of normalized subgap resistance of different junctions. Their trend follows the prediction of the BCS theory when $T > 1.0 K$ . . . . .	96

# List of Tables

3.1 Possible sources of errors in the Hall measurement . . . . .	25
------------------------------------------------------------------	----

## Part I

# Hall resistance characterization of thermoelectric materials

# Chapter 1

## Hall measurement Introduction

### 1.1 Hall measurement

The Hall measurement provides the characterization of the charge carrier density of metal or semiconductor materials. For the rectangular bar sample shown in Fig: 1.1, when the current is applied along the  $x$  direction, and the magnetic field is along the  $z$  direction, an electrical potential is generated along the  $y$  direction because of the equilibrium of the electric force and the Lorentz force:

$$qE = Bqv \quad (1.1)$$

The Hall resistance  $R_H$  is

$$R_H = \frac{V_H t}{IB} \quad (1.2)$$

where  $V_H$  is the Hall voltage,  $t$  is the thickness of the sample,  $I$  is the excitation current and  $B$  is the applied magnetic field.

The charge carrier density  $n$  is

$$n = -\frac{1}{R_H e} \quad (1.3)$$

where  $e = 1.6 \times 10^{-19} J/C$ . If the electrical conductivity,  $\sigma$ , of the sample is also known, then the charge carrier mobility,  $\mu$ , is

$$\mu = R_H \sigma \quad (1.4)$$

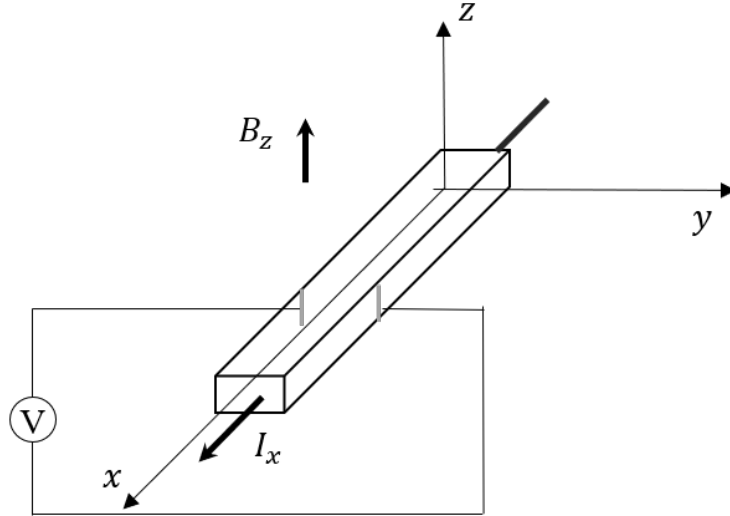


Figure 1.1: The Hall effect illustration. When current  $I_x$  is along x-axis and magnetic field  $B$  is along z-axis, the Hall voltage is along y-axis.

## 1.2 Thermoelectric materials

### 1.2.1 Introduction of thermoelectric materials

Thermoelectric materials can transfer heat to electrical energy and vice versa. They have some applications such as Peltier coolers and thermocouples. Certain physical properties are usually measured in order to compare the thermoelectric properties among materials.

The Seebeck coefficient is

$$\alpha = \frac{8\pi^2 k_B^2}{3eh^2} m^* T \left(\frac{\pi}{3n}\right)^{\frac{2}{3}} \quad (1.5)$$

where  $m^*$  is the effective mass of the carrier and  $n$  is the charge carrier density.

The quality of thermoelectric materials is characterized by measuring the figure-of-merit:

$$zT = \frac{\alpha^2 T}{\rho \kappa} \quad (1.6)$$

where  $\rho$  is the electrical resistivity and  $\kappa$  is the total thermal conductivity.

$\kappa$  is decided by the charge carrier term,  $\kappa_e$ , and the lattice term,  $\kappa_L$ :

$$\kappa = \kappa_e + \kappa_L \quad (1.7)$$

and:

$$\kappa_e = L\sigma T \quad (1.8)$$

where  $L$  is the Lorenz factor, and  $\sigma$  is the electrical conductivity. Some thermoelectric materials with high thermoelectric efficiency have low thermal conductivity and high electrical conductivity.[42] One of the ideas to lower thermal conductivity but not change electrical conductivity is to design materials with low  $\kappa_L$ .

Some materials are doped with external elements in order to improve their thermoelectric properties. One example is to substitute Ag atoms by Cu in  $Ag_2Se_{0.5}Te_{0.5}$ (AST) to form  $Cu_xAg_{2-x}Se_{0.5}Te_{0.5}$  structure.[26] The maximum power factor,  $PF$ , and figure of merit,  $ZT$ , were achieved when  $x=0.1$  as compared to when  $x=0.01$ , which confirmed the positive effect of doping.

Good thermoelectric materials are usually heavily doped semiconductors and have a high  $zT$  coefficient. Their charge carrier densities are in the range of  $10^{18}cm^{-3}$  to  $10^{21}cm^{-3}$  and often show weak temperature dependence near room temperature. Changing the concentration of the doped elements in the materials can change the thermoelectric properties such as  $\alpha$ ,  $\rho$  and  $zT$ . [42]

## 1.2.2 Information from Hall measurement

The Hall measurement measures charge carrier density,  $n$ , and mobility,  $\mu$ , which are useful when studying the thermoelectric materials. As Eq.1.5,  $\alpha$  is related to  $n$ , so the change of  $\alpha$  as well as  $zT$  may be determined by the change in  $n(T)$  when studying single compositions.  $\mu$  is related to scattering time,  $\tau$ , and effective mass,  $m^*$ , of the charge carrier: [10]

$$\mu = e \frac{\tau}{m^*} \quad (1.9)$$

which is related to the mechanisms of electron conduction. Since the thermoelectric properties of the materials are often changed along with the concentration of doped elements in the compounds, it is interesting to know how the changes in  $x$  related to the values of  $n$  and  $\mu$ .

Fig: 1.2 shows the carrier concentration of doped  $Mg_{2.08}Si_{0.4-x}Sn_{0.6}Sb_x$  versus temperature measured from the Hall measurement.[6] The sum of the proportions of Si and Sb elements equals 0.4; the larger  $x$  value represents more doping of Sb. Around room temperature,  $T = 300 K$ , the carrier concentration increases from  $10^{19} cm^{-3}$  when  $x = 0$  to the level of  $10^{21} cm^{-3}$  when  $x = 0.072$ . The substitution of  $Si$  by  $Sb$  increases the carrier concentration. Changing the  $x$  value also changes the temperature dependence of the

carrier concentration. When  $x < 0.036$ , the samples are slightly doped and clearly show strong temperature dependence; when  $x > 0.036$ , the samples are heavily doped and show weak temperature dependence. This transition may correspond to the Mott transition of doped semiconductors.[10]

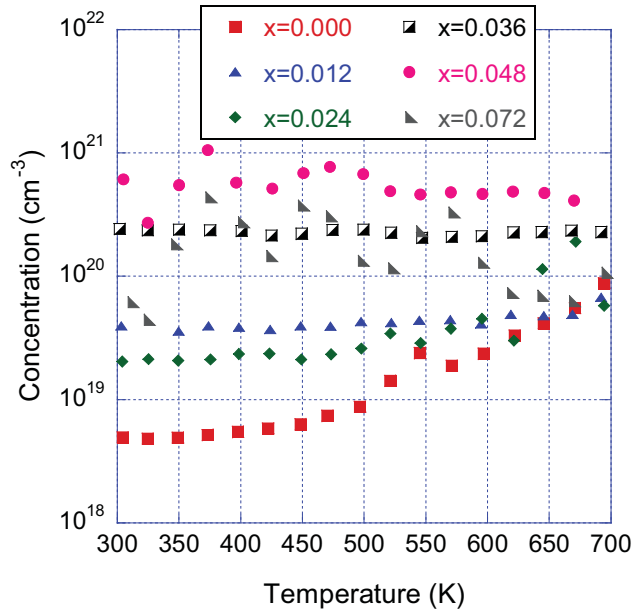


Figure 1.2: Carrier concentration of doped thermoelectric material  $Mg_{2.08}Si_{0.4-x}Sn_{0.6}Sb_x$  at high temperature[6]. Varying  $x$  changes the composition and temperature dependence of the charge carrier concentration of the compound.

### 1.2.3 Information of Samples

The thermoelectric samples involved in this thesis were provided by professor Holger Kleinke's group at the University of Waterloo. The samples were doped semiconductors synthesized by high-temperature melting and then hot-press sintering. The  $n$ ,  $\sigma$  and  $\mu$  of the samples needed to be characterized by Hall measurement. Some of the samples were  $Mg_2Si_{0.3}Sn_{0.67}Bi_{0.03}/SiC$  composites,  $Ba_3Cu_{16-x}Se_{11-y}Te_y$ , and  $BaCu_{6-x}Se_{1-y}Te_{6+y}$ . [28][21][22]

## 1.3 Review of Hall measurement setups

### 1.3.1 Literature review

The traditional Hall measurement uses rectangular bar samples, shown in Fig: 1.3, whose working principle is based on the definition of  $R_H$  in Eq.1.2.[37] This method can measure the  $\sigma$  and  $R_H$  without rewiring the sample. With proper electronics and sufficient integration time, the accuracy of the method is ultimately limited by the geometrical parameters: the width and the thickness of the sample, and the distance,  $d$ , between the electronic contact points. The excitation current,  $I_x$ , and magnetic field,  $B_z$ , are typically DC. Since the voltage offsets such as the thermal EMF and misalignment voltage are significant during the measurement, these offsets need to be determined and analyzed by measuring the Hall voltage multiple times with different polarity of  $I_x$  and  $B_z$ . [8]

Recently, many Hall measurement setups have been designed to measure the Hall coefficient and electrical conductivity of samples with unique chemical compositions. Most of them are based on the Van der Pauw (VDP) method. The temperature range of the measurements varies depending on the materials.

Borup et al. developed three similar VDP Hall measurement setups in Caltech, JPL and Aarhus University. [9] The sample holder contained four rods which could be pressed on the sample to form electrical connections. The temperature was controlled by the PID method. The temperature range could be from room temperature to 1000 °C. Electromagnets were used which provided magnetic field up to 2.0 T. Some of the samples were n-type  $Mg_2Si$ , indium doped  $PbTe_{1-y}Se_y$  alloys and  $Cu_7PSe_{6x}S_x$ . [4][39]

Adnane et al. developed a VDP Hall measurement setup with a permanent magnet instead of an electromagnet. The magnetic field was up to 0.4 T. The measurement temperature can be up to 700 °C. The samples were doped silicon. [1]

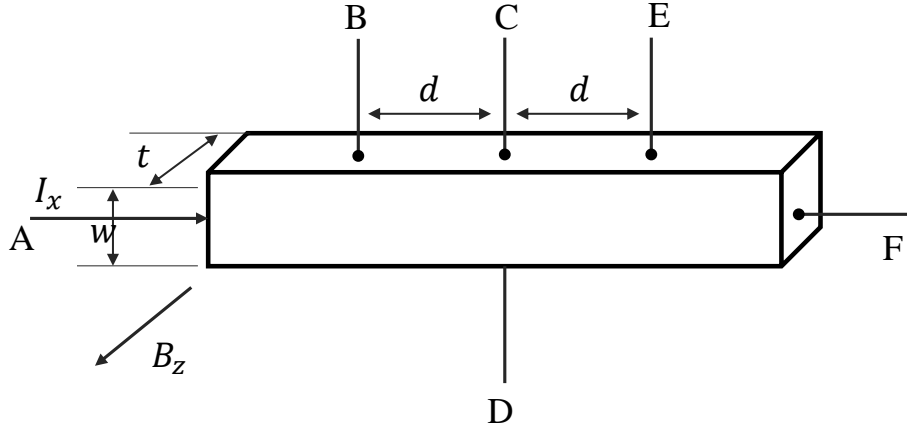


Figure 1.3: The sample with rectangular bar geometry in traditional Hall measurement. [37] Lead A and F are for the current; lead C and D are for the Hall voltage measurement; lead B and E are for the electrical conductivity measurement.

Gunes et al. designed a Halbach array to provide an AC magnetic field in the Hall measurement.[15] VDP technique was used. This setup had a high measurement speed because of the rotating magnetic field up to 1.0 T, which took about 5 seconds to obtain a Hall coefficient data point. However, the noise level of thermal EMF was not under discussion in the article. 20 % Sr-doped  $BiCuSeO$  was tested at different temperatures. Its charge carrier density increased along with temperature, with about 5 % error bar.

There may be some limitations when the Hall resistance of thermoelectric materials was measured by these setups. First, based on the literature review, the voltage offsets caused by the thermoelectric effect and the electrical conductivity of the samples were noted but not fully considered. The common technique was to proceed with the measurement over a large temperature range between each data point. The accuracy of Hall measurement at a certain temperature was rarely discussed in these reports. Second, some VDP method setups were not suitable for bulky samples with a relatively large thickness. The reason is that the setups make electrical contact by pressing four probes to the top surface of the sample. When applied with the excitation current, more electrons pass the top region of the sample than the lower region; in other words, the equipotential field lines are not parallel in the region between the current leads. In addition, With thicker samples, the Hall voltages that are produced are very small.

### 1.3.2 Thanh Lê’s Hall measurement setup

A DC Hall measurement setup was built up by Thanh Lê in our group in order to test thermoelectric samples from professor Kleinke’s group.[25] This setup applied a DC current to the sample and measured the Hall voltage by an Agilent 34420a nano-voltmeter. It could provide a DC magnetic field up to  $0.5 T$ . There was no temperature control in this setup. The Hall measurement was at room temperature. The samples were connected to copped leads by silver paint. The lithographically patterned palladium gold pads were deposited at the contact positions of the samples, which could improve the electrical conductance at the contacts and prevent the samples from reacting with the silver paint. Some thermoelectric samples were characterized by this setup. Their Hall resistance uncertainties were too high to be helpful to study the thermoelectric properties of the samples. Therefore, this setup needed some improvements for convenience and accuracy. The sources of errors had to be identified.

## 1.4 Challenges

A new setup should be designed for the Hall measurement of thermoelectric materials. The challenges are from the geometry and special thermoelectric properties of the samples, the low-level  $V_H$  signal, the noise sources, and the measurement setup.

From Eq.1.2, for the same  $I$  and  $B$ , it is preferred to have samples with small thickness to enlarge the  $V_H$  signal. However, some samples prepared by sintering are likely to break when the thickness is smaller than  $1mm$ . Thus the Hall measurement setup should be able to measure bulky samples.

For the measurement connection, there are usually six electrical leads connecting to the sample. The two leads that are placed furthest along the length are the current leads, while the other four leads are used to measure the voltage signal. The uncertainties of the sample geometry parameters are usually high, which causes the high uncertainty of the electrical conductivity measurement and the Hall measurement.

The electrical and mechanical properties of thermoelectric materials limit the level of Hall voltage signal. From Eq. 1.2, the level of  $V_H$  signal is related to  $t$ ,  $I$  and  $B$ . Raising  $I$  will eventually cause Joule heating problems. The  $B$  is limited by the maximum power of the magnet. For example, assume there is a sample with charge concentration  $= 10^{19} cm^{-3}$  and thickness  $t = 1 mm$ . By using  $10 mA$  excitation current and  $0.5 T$  magnetic field, the Hall voltage  $V_H = 3 \times 10^{-7} V$ , or  $300 nV$ . The low voltage signal requires proper considerations about the sources of errors; otherwise, the signal may be buried in the noise.

When measuring the Hall voltage, the voltage signal,  $V_o$ , contains not only the Hall voltage,  $V_H$ , but also the misalignment voltage,  $V_M$ , and the thermal EMF,  $V_T$ .  $V_M$  is from the ohmic resistance of the sample between two misaligned sense leads.  $V_T$  is from the temperature gradient within the circuits.  $V_o$  can be written as:  $V_o = V_H + V_T + V_M$ . Theoretically,  $V_M$  and  $V_T$  can be canceled by multiple steps of voltage signal measurement with the different directions of the excitation current or the magnetic field. However, it cannot completely eliminate the voltage offset caused by temperature drift. It has been reported that  $V_T$  and  $V_M$  could be highly temperature-sensitive which makes the Hall measurement challenging when the drifting offset is much larger than  $V_H$ .<sup>[9]</sup> A temperature control system may reduce the drifting by stabilizing the sample temperature. If not working properly, the temperature control can introduce a different noise source.

As the experiment measuring low-level voltage signals, there are some general things to be considered such as the proper circuit design, proper shielding and well-defined connections.<sup>[19]</sup> The noise caused by random errors needs to be evaluated and controlled to a reasonable level.

## 1.5 Motivations

The motivation of developing the Hall measurement technique is to accurately measure the charge carrier density,  $n$ , and charge carrier mobility,  $\mu$ , of the thermoelectric samples with different chemical compositions and preparation proceeds. The goals are: build up a reliable Hall measurement system for bulky thermometric samples, study the noise sources in the Hall measurement, and minimize the measurement uncertainty.

Lê's DC Hall measurement setup was improved. A new sample holder and a PID temperature control system were added to this setup. An AC Hall measurement setup was designed and built. The DC Hall measurement setup provided a DC current to the sample and used a nano-voltmeter to measure the Hall voltage. The AC Hall measurement setup applied AC current to the sample and measured the Hall voltage signals by a lock-in amplifier.

The first part of the thesis is to present the details of the two setups, including a sample holder using mechanical contact to the sample and a PID temperature control system. The second part is to discuss the possible noise source and voltage offset of the Hall measurement based on the setup. Noise-frequency spectrum figures will also be presented in this part. The third part is to discuss the measurement results from the DC and AC Hall measurement of a thermoelectric sample around room temperature.

# Chapter 2

## Hall measurement Setup

### 2.1 Sample holder

The sample holder and its sample holder box are shown in Fig: 2.1 and Fig: 2.2. The sample holder is a machined rectangular aluminum block, placed in the center of Fig: 2.2. It has 2.5 inches in length and 1.6 inches in width. It is mounted tightly to the aluminum box by two screws. There are two traces, perpendicular to each other, on the top side of the sample holder. Four white plastic blocks with six pogo pins are in the traces. Two of the blocks can move back and forth so that samples with different lengths are easy to fit. The third block can be rotated in a small angle range. The fifth plastic block glued at the center of the sample holder is the spacer for the sample. The six gold pogo pins are used to make mechanical and electrical contact with the sample.[36][11] They are also connected to the black pin connector by copper wires. A K-type thermocouple is taped to the aluminum box by copper tape with electrically insulating epoxy, which is designed to measure the temperature of the box. A Peltier cooler is glued by thermally conductive epoxy to the top of the box. The box is surrounded by one-inch-thick polystyrene foam, which is a thermal insulator.

Fig: 2.1 is the illustration of the sample holder. Six pogo pins, ordered from McMaster-Carr Supply Company,[11] are labeled A-F. Leads A and B are for current, using waffle pogo pin tips with 0.75" head diameter for maximum contact surface area. Leads C and E are the sense leads which are to measure Hall voltage. Leads C and D are for electrical conductivity measurement. Lead F is usually for supporting the sample. The connection to lead D can be switched to lead F by using the electronic switch. Leads C to F use 30° spear tips for good oxidized sample layer penetration. The traces and plastic pin holders

are accurately machined to minimize the misalignment between lead C and lead E. The typical dimension of the sample is  $7.6\text{ mm} \times 2.5\text{ mm} \times 1.3\text{ mm}$ .

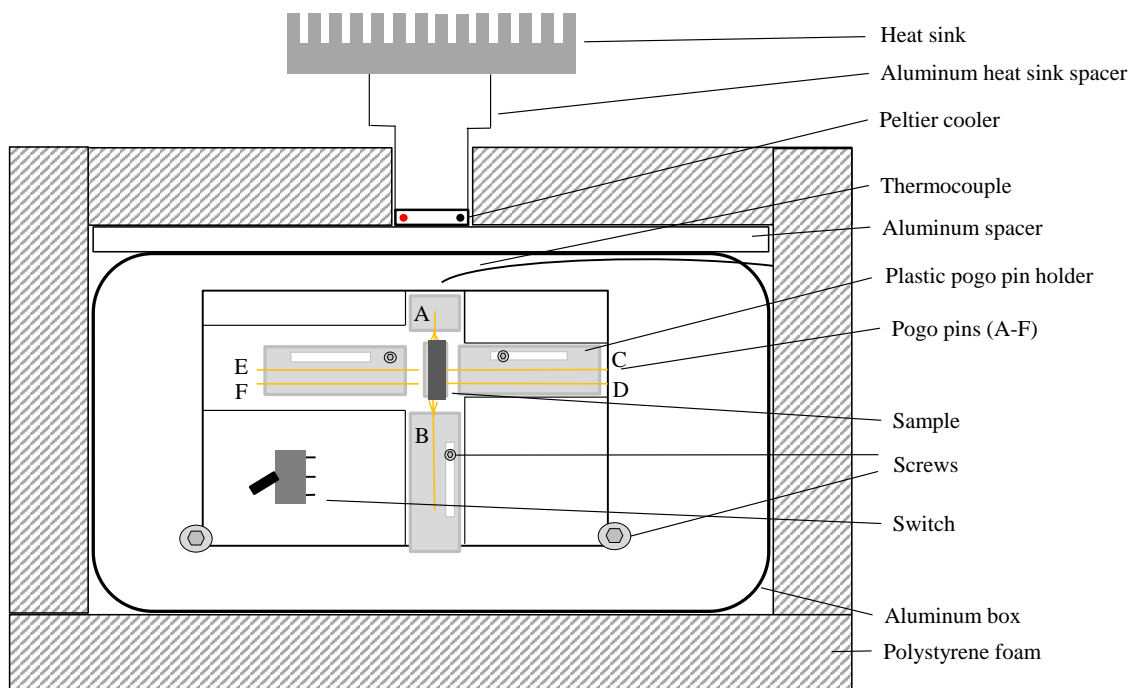


Figure 2.1: Hall measurement sample holder box illustration. The aluminum sample holder and the six pogo pins are mounted at the center of the box.

There are some reasons for choosing pogo pins instead of using lithographically patterned pads and chemical joints such as silver epoxy. The first reason is the time for sample preparation. It takes hours to wait for the electrically conductive epoxy to be fully dry. Once the epoxy is dry, it is impossible to trim the alignment between the sense leads. Secondly, the chemicals may react with the sample and change its composition. The third reason is that the Hall measurement requires a small contact area of voltage leads to the sample; however, it is hard to control the painting area of the epoxy. The contact pads can be relatively large with inconsistent contact resistance, which makes the true distance between contact points hard to determine. Compared with the chemical joints, the pogo pins have some advantages. It usually takes 10 minutes to mount or dismount the sample, which is convenient. The tips of the pogo pins can be chosen from various shapes and sizes. The misalignment voltage can be reduced by slightly pushing the sense pins with tweezers when the pins are touching the sample. The contact points are relatively small, allowing an accurate measurement of the distance of the sense probes for four-wire resistance measurement.

On the other hand, the contact resistance at the sample-pin joints may be a problem. It is usually  $5 \Omega \sim 15 \Omega$  but can be over  $100 \Omega$ , depending on the electrical conductivity of the samples. This may be because of the metal-semiconductor joint since the samples are semiconductors, and the pogo pins are gold-coated copper. It could also be due to the oxidization of the sample surface. High contact resistance may cause high noise and Joule heating problems.



Figure 2.2: Picture of the Hall measurement sample holder box and the sample holder.

## 2.2 Temperature control

The thermocouple and the Peltier cooler are used to control the box temperature by the PID control method. This method calculates the temperature difference and then outputs a voltage to the cooler. “P” is “proportion”, “I” is “integral” and “D” is “derivative”. “P” is the most basic parameter in temperature control. It can hold the temperature near the set point on its own. “I” can minimize the difference between the real temperature and the set point. “D” is good for speeding up the transitions from one temperature to another but can introduce an enhancement of noise; for this system, “D” is not used, so the temperature control system is represented as “PI control”. The PI control VI in LabVIEW is based on:

$$u = K_p e + K_I \int e dt \quad (2.1)$$

where  $u$  is the output signal,  $e$  is the error between the input value and the goal value,  $K_p$  and  $K_I$  are the proportion and integral gains.[43]

The PI temperature control system is shown in Fig: 2.3. The temperature is measured by the thermocouple and amplified by the LT1025 thermocouple cold junction compensator. The output voltage from the thermometer is read by an Agilent 34401a voltmeter. The voltage to temperature relation is  $10 \text{ mV}/^\circ\text{C}$ . A LabVIEW program operates the PI control system.

The Hall measurement requires a magnet to provide magnetic fields. It generates a significant amount of heat when running and raises the temperature of the sample holder. The Hall measurement might be affected by the drifting temperature. Therefore, the PI temperature control was set up to reduce the measurement uncertainty caused by the temperature change. At the same time, it is necessary to discuss that the noise might be introduced by using the PI control system.

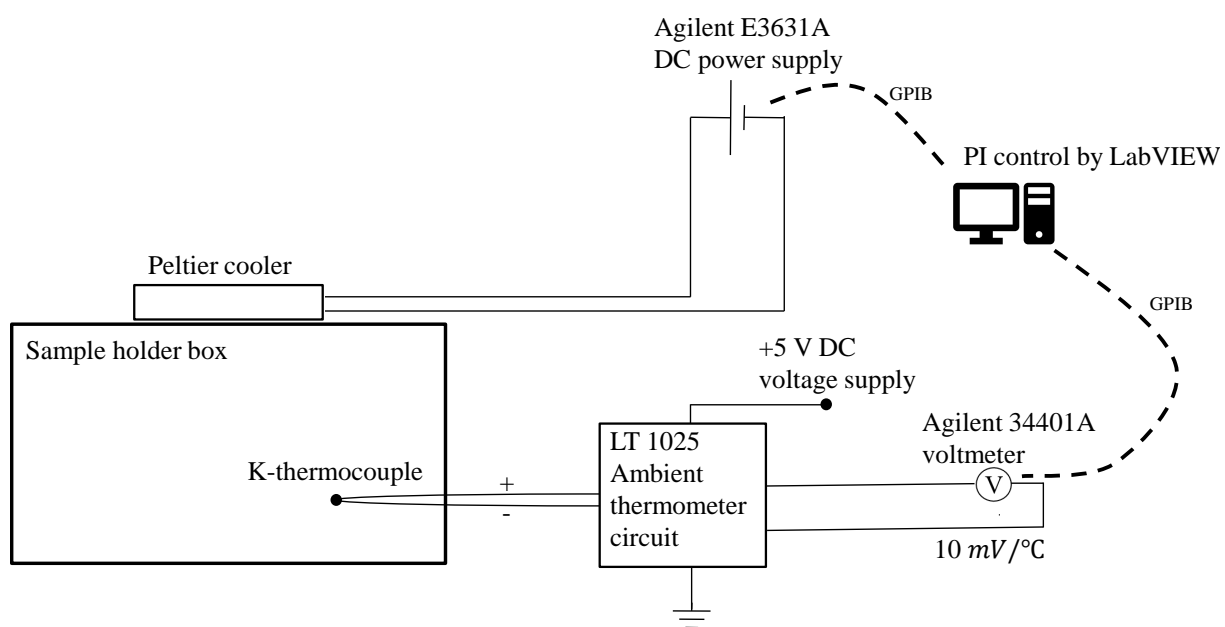


Figure 2.3: Illustration of the PI temperature control system run by a LabVIEW program. The Peltier cooler. A temperature can be set from 15 °C to 30 °C with an uncertainty of  $\pm 0.05$  °C.

## 2.3 DC Hall measurement setup

The DC Hall measurement setup is shown in Fig: 2.4. [25] The setup can be introduced based on the part inside or outside the copper shield room. The sample holder box and the magnet are inside the shield room, the electronic leads of which are connected to the outside through the connectors on the wall of the shield. The copper shield is designed to shield the high-frequency signals such as radio waves from the internet and radio broadcasting systems. The shield is good for low-temperature measurement but not for the Hall measurement at room temperature. The heat generated from the magnet is difficult to remove from the shield room when the door of the shield room is closed. Outside the shield room, a stable-current-source circuit provides the excitation current to the sample with the range of 1 *mA* to 150 *mA*. An Agilent 34420a nano-voltmeter reads the DC voltage signal from the sample. A Kepco BOP power generator provides current to the magnet. The +5 V DC voltage to the DC Dual cold junction compensator is provided by an NI-PCI 6251 DAQ interface, which also measures the temperature from thermocouples.

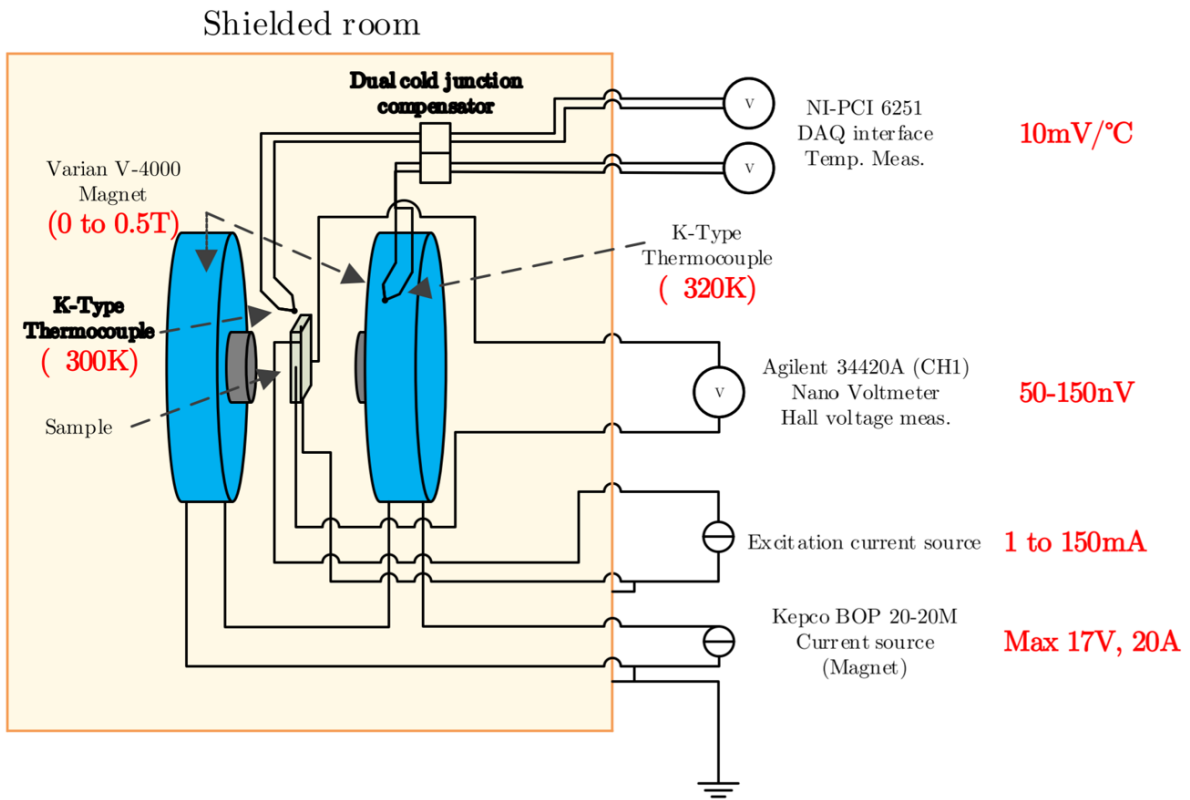


Figure 2.4: DC Hall measurement setup illustration.[25]

The DC Hall measurement is controlled by a LabVIEW program. It needs to run a five-step cycle to obtain an  $R_H$  data point, and each step uses different excitation current or magnetic field. Step one is to turn the current from initial value  $I = 0$  to  $+I$ , and the magnetic field changes to  $+B$  from  $B = 0$ . Step two is to change the current to  $-I$ , which has the opposite direction of the current in step one but the same magnitude; the magnetic field is  $+B$ . The current and the magnetic field are  $(-I, +B)$  in step three and  $(-I, -B)$  in step four. In step five, the current and the magnetic field are back to zero. Fig: 2.5 is an example of DC Hall measurement voltage data.

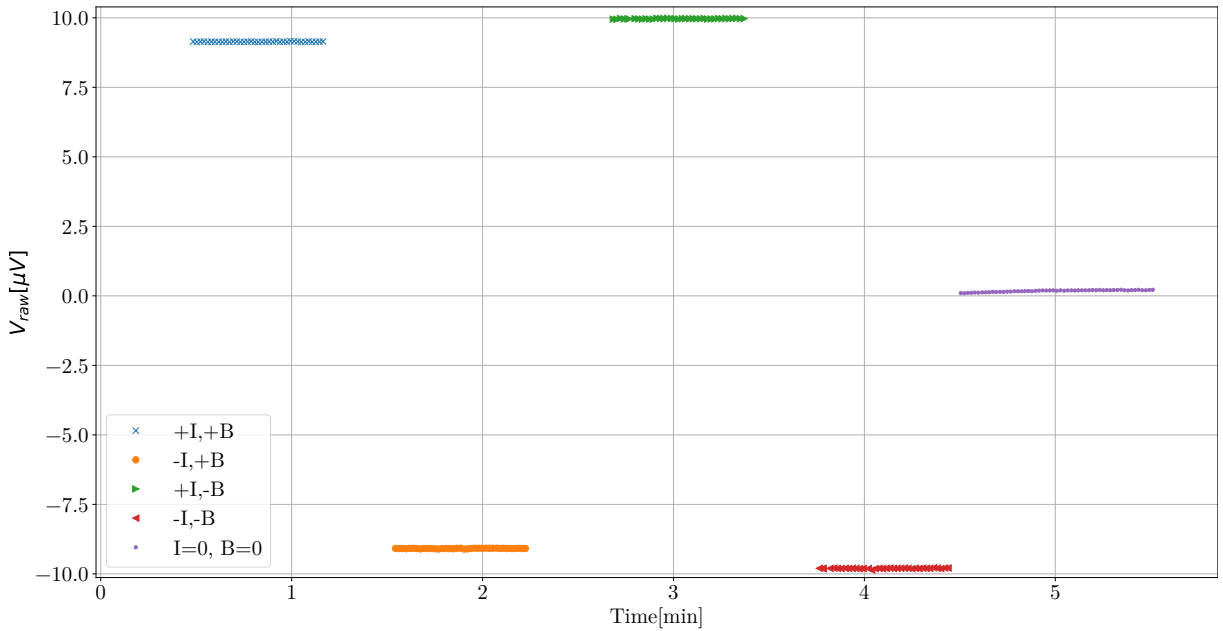


Figure 2.5: Example of voltage data from a measurement cycle in DC Hall measurement. The five voltage steps correspond to the cycle:  $(+B, +I) \rightarrow (+B, -I) \rightarrow (-B, +I) \rightarrow (-B, -I) \rightarrow (0, 0)$ . It takes about five minutes per cycle

If the voltages from the first four steps are set to be  $V_1$ ,  $V_2$ ,  $V_3$ , and  $V_4$ , then:

$$\text{Hall voltage, } V_H = \frac{V_1 - V_2 - V_3 + V_4}{4} \quad (2.2)$$

$$\text{Thermal EMF, } V_T = \frac{V_1 + V_2 + V_3 + V_4}{4} \quad (2.3)$$

$$\text{Misalignment voltage, } V_M = \frac{V_1 - V_2 + V_3 - V_4}{4} \quad (2.4)$$

## 2.4 AC Hall measurement setup

The AC measurement applies an AC excitation current to the sample and measures an AC voltage signal from the sample. The setup is shown in Fig: 2.7. It uses the same sample holder, temperature control system and the magnet as the DC measurement setup. Instead of using a DC excitation current, an SR 830 lock-in amplifier provides the AC current with a certain frequency,  $f_1$ , to the thermoelectric sample. The  $R_1$  resistor behaves as the current-limiting resistor when the sample has high electrical conductivity. A second lock-in amplifier, using the output voltage from the first one as the reference, measures the voltage across the resistor  $R_2$  for calculating the excitation current. The voltage signal, at  $f = f_1$ , from the sample is measured by the first lock-in amplifier. The magnetic field is provided by the same magnet as in the DC measurement setup.

A PAR 190 low-noise transformer can be used to increase the voltage signal from the sample. The transformer has a  $\times 100$  gain option and a  $\times 1000$  gain option. The functionality of the transformer is also decided by its loading resistance and its input voltage frequency, which follows the frequency response curves in Fig: 2.6.[3] The frequency of the AC voltage is chosen to be  $15.125\text{ Hz}$  for the best frequency response. The input impedance of the transformer is about  $600\ \Omega$  at this frequency. When using the  $\times 100$  gain, its loading impedance needs to be much smaller than  $50\ \Omega$  to prevent losing the gain.

The SR 830 lock-in amplifier measures the magnitude of the voltage at its input with the same frequency as its output voltage: [40]

$$\begin{aligned} V &= V_{\text{sig}} V_L \sin(\omega_r t + \theta_{\text{sig}}) \sin(\omega_L t + \theta_{\text{ref}}) \\ &= 1/2 V_{\text{sig}} V_L \cos([\omega_r - \omega_L]t + \theta_{\text{sig}} - \theta_{\text{ref}}) - 1/2 V_{\text{sig}} V_L \cos([\omega_r + \omega_L]t + \theta_{\text{sig}} - \theta_{\text{ref}}) \end{aligned} \quad (2.5)$$

where  $V_{\text{sig}}$  is the input signal voltage,  $V_L$  is the lock-in reference voltage,  $\omega_r$  is the input signal frequency, and  $\omega_L$  is the lock-in reference frequency. After a low pass filter, the voltage signal with  $\omega_r = \omega_L$  remains. The noise signal, far from the Hall voltage signal frequency such as the  $V_T$ , is filtered by the lock-in amplifier.

The SR830 lock-in amplifier can use the offset function to measure the small voltage change with high resolution. If the input voltage signal is  $V_i$ , a constant offset voltage  $V_{\text{offset}}$  can be set so that the measured voltage by the lock-in amplifier  $V_o$  is

$$V_o = V_i - V_{\text{offset}} \quad (2.6)$$

When  $V_o$  is much smaller than  $V_i$ , the sensitivity of measuring  $V_o$  can be better than that of measuring  $V_i$ , which improves the detection of small voltage change.

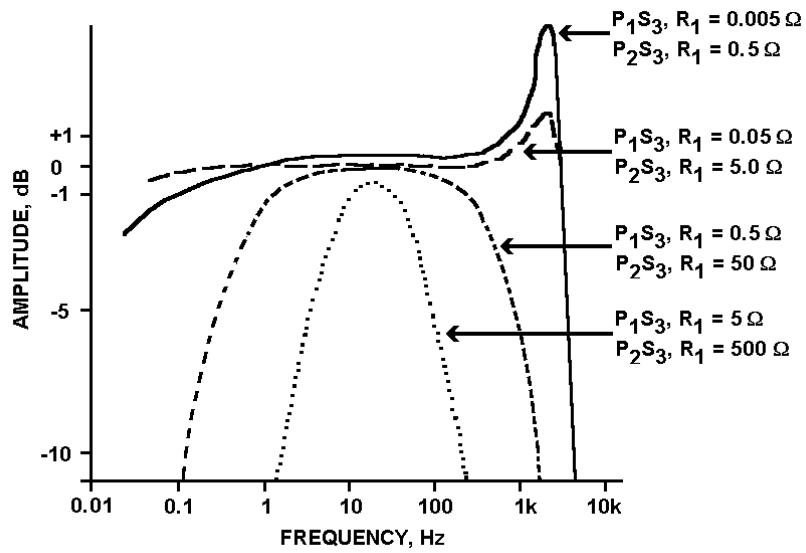
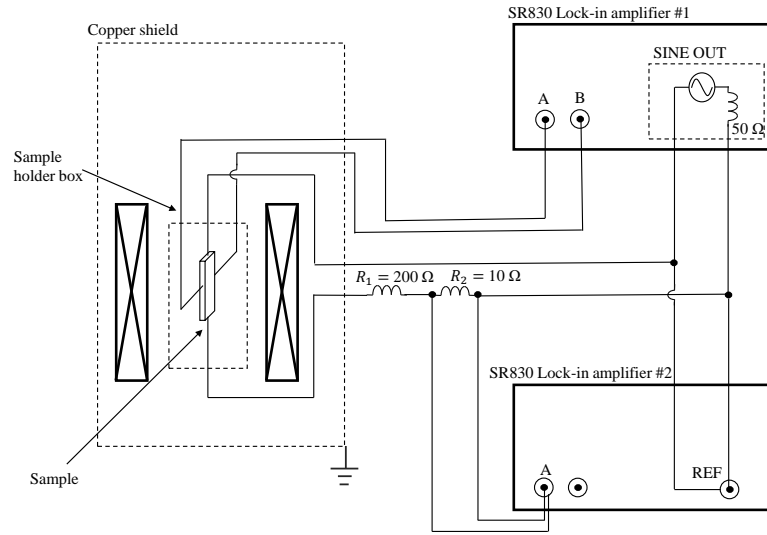
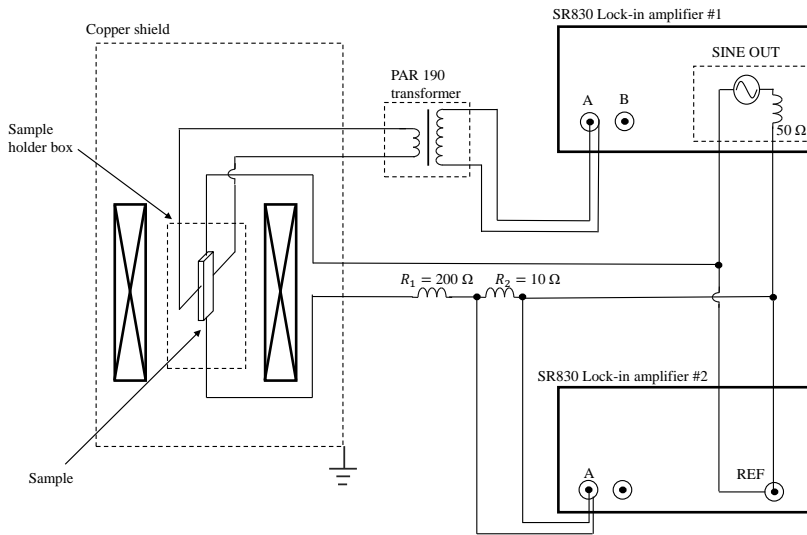


Figure 2.6: The typical frequency response curves of PAR 190 transformer.[3]  $P_1S_3$  corresponds to the  $\times 1000$  gain, and  $P_2S_3$  corresponds to the  $\times 100$  gain.  $R_1$  is the loading impedance of the transformer.



(a) AC Hall measurement setup without transformer



(b) AC Hall measurement setup with transformer

Figure 2.7: AC Hall measurement setup illustration: (a) without transformer, (b) with transformer

Fig: 2.8 shows an example of an AC Hall measurement with the transformer. The lock-in amplifier can be used to delete an offset voltage during the voltage measurement so that high-resolution mode can be applied.

In an AC Hall measurement cycle, there are three steps where the magnetic fields are  $+B$ ,  $-B$  and 0 while the current is not changed. The voltages recorded in the first two steps are  $V_1$  and  $V_2$ . The Hall voltage with current  $I$  and magnetic field  $B$  is

$$V_H = (V_1 - V_2)/2 \tag{2.7}$$

When not using the transformer, the sample voltage signal,  $V_x$ , is directly sent to the lock-in amplifier, the voltage value that is recorded is  $(V_x - V_{\text{offset}})$ .

If using the transformer, the voltage signal sent to the lock-in amplifier has been increased by a factor of 100. For the comparison between the measurements with and without the transformer, the voltage data in Fig: 2.8 is shown after considering the gain of the transformer.

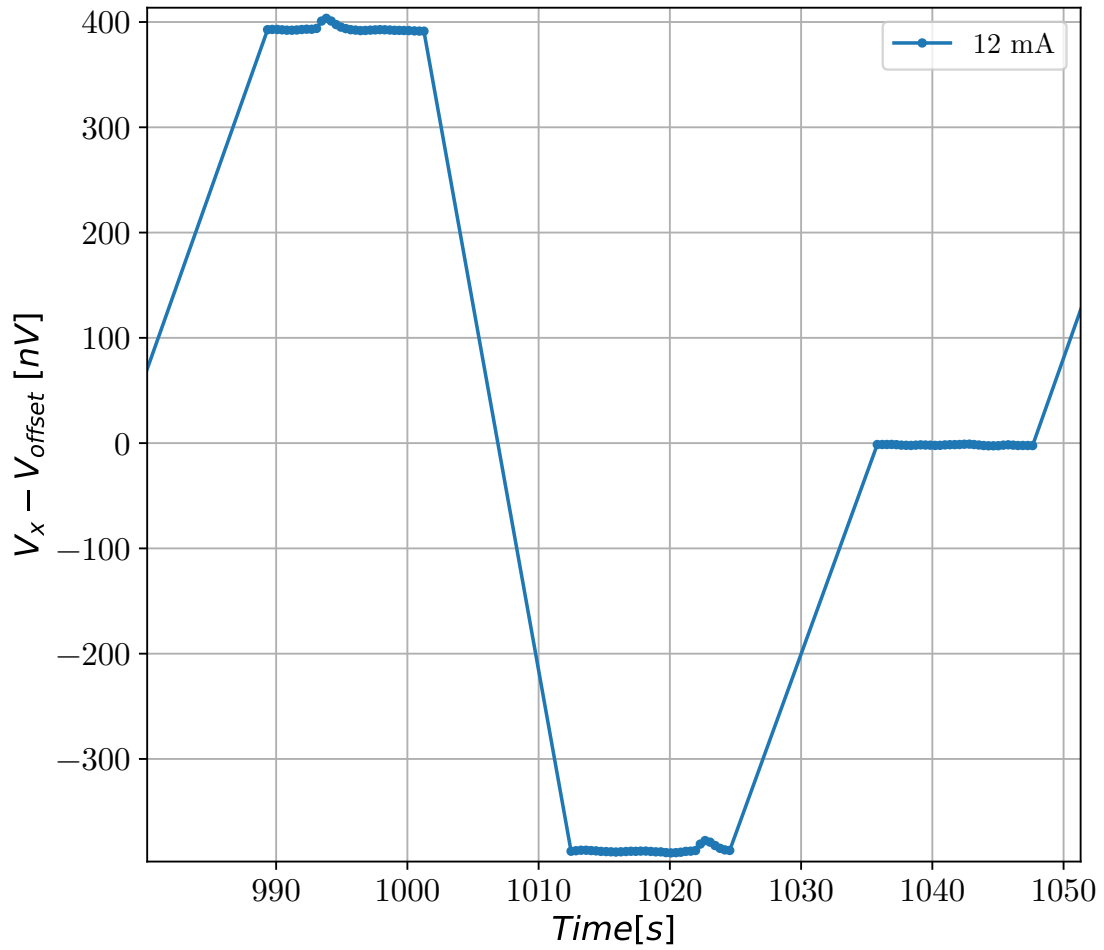


Figure 2.8: Example of the voltage signal read from the AC Hall measurement. The voltage steps in the graph from left to right correspond to  $+B \rightarrow -B \rightarrow 0$ . Every three steps is a measurement cycle which takes about 1 minute.

## 2.5 Measurement steps and measurement speed

The steps of the Hall measurement are shown in Fig: 2.9. Assume a sample is ready to be tested. It takes about 15 to 30 minutes in total to mount the sample on the sample holder, adjust the pogo pins and reduce the contact resistance. If the temperature needs to be set, the temperature control needs to run 20 minutes before the temperature is steady.

The DC and AC Hall measurement setups share the same loops inside the shield room, but they use different current supplies and voltmeters. For that reason, only one of the setups can be run at the same time. It has been seen that the AC Hall measurement, for the same sensitivity, is about four times faster than the DC Hall measurement. If taking 100 data points of  $R_H$ , the AC Hall measurement requires 1.7 hours, while the DC Hall measurement requires 8.3 hours. Therefore, the AC Hall measurement is recommended for a faster test.

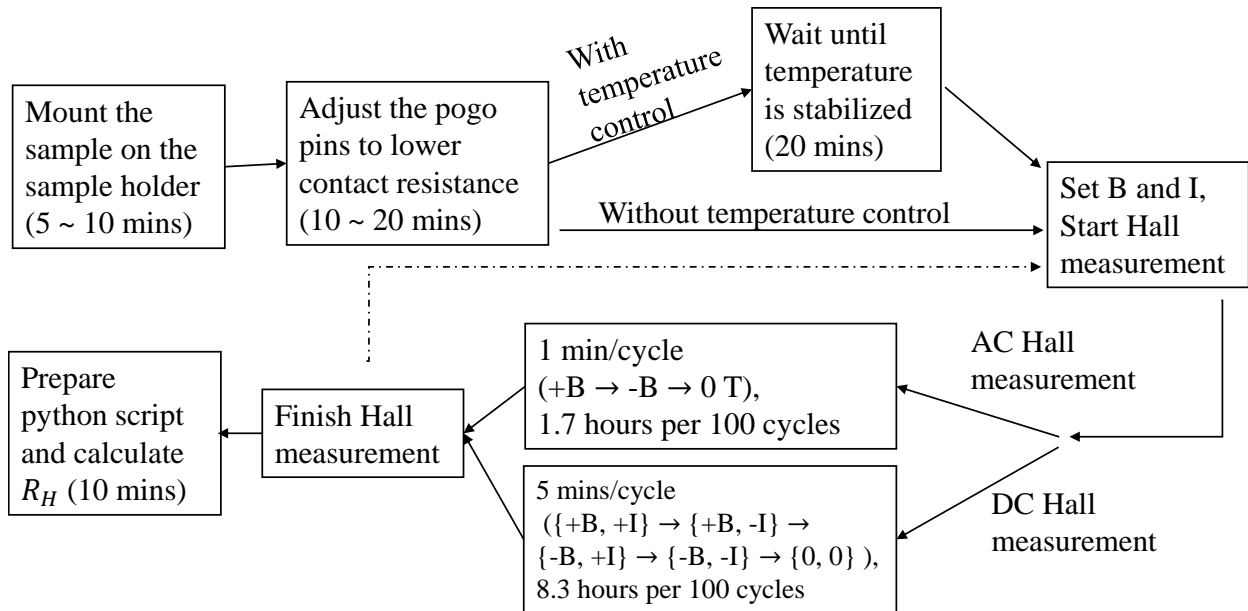


Figure 2.9: Experiment steps of the Hall measurements and the measurement speed of each step. If taking the same amount of  $R_H$  data points, the AC Hall measurement is about four times faster than the DC Hall measurement with the same sensitivity.

# Chapter 3

## Measurement errors and the noise

When measuring the electrical signals, there are some sources of errors in the measurement, such as ground loops, drifting temperatures, and the drifting magnetic field. Therefore, it is essential to understand the composition of the signals, the instrument precision, and the noise.

The first part of the chapter is the general knowledge of electrical signals and measurement errors, and how they are involved in the Hall measurement. The second part is to compare the noise spectrum of different setups and to characterize their noise level.

### 3.1 Possible sources of errors in the Hall measurement

The measurement errors can be divided into two categories: systematic errors and random errors.[32]

The common types of electronic noise: Johnson noise, shot noise and 1/f noise.[18, ch.8] There is usually more than one noise source in the measurement. If the noise follows the Gaussian distribution, the rough calculation of total noise caused by two independent noise sources is[33, p.19]

$$V_o^2 = V_1^2 + V_2^2 \quad (3.1)$$

Where  $V_o$  is the root mean square (RMS) of the total noise,  $V_1$  and  $V_2$  are the RMS of two noise signals. Note that the noise is more complicated than an RMS value; therefore, the source generating the source must be considered when doing the calculation.

Systematic errors	Random errors
Environment disturbance: <ul style="list-style-type: none"> <li>• High frequency wireless signal pickup</li> <li>• Temperature drift</li> </ul>	Electronic noise: <ul style="list-style-type: none"> <li>• thermal noise</li> <li>• 1/f noise</li> </ul>
Problems of the circuit and connections: <ul style="list-style-type: none"> <li>• Voltage loading error</li> <li>• Common mode rejection ratio problem</li> <li>• Misalignment voltage <math>V_M</math></li> <li>• Thermal EMF <math>V_T</math></li> </ul>	Scale and sensitivity: <ul style="list-style-type: none"> <li>• Voltmeters</li> <li>• Current supply</li> </ul>
Act of measurement: <ul style="list-style-type: none"> <li>• Sample self-heating</li> <li>• GPIB low frequency noise</li> <li>• Magnetic EMF</li> </ul>	
Sample geometry and distance between probes	

Table 3.1: Possible sources of errors in the Hall measurement

**Thermal noise:** also called Johnson noise which is caused by the unbiased movement of the electrons in the materials, which follows

$$V = \sqrt{4k_B T R \Delta f} \quad (3.2)$$

where  $R$  is the resistance and  $\Delta f$  is the frequency bandwidth.

Thermal noise is a fundamental noise in the sample, the leads, the amplifiers and transformers, and the voltmeters. It is the theoretical limit of the noise level. The thermal noise behaves as Gaussian noise; therefore, by increasing the reading time constant, the thermal noise of the detected signal can be reduced.

**Misalignment voltage:** misalignment voltage,  $V_M$ , depends on the sample resistance between the two Hall voltage leads and the excitation current, shown in Fig: 3.1. Furthermore, it is directly related to  $\rho$  by the Ohm's law:

$$V_M = IR_M = I\rho(T)\frac{l}{A} \quad (3.3)$$

where  $l$  is the misalignment distance between two sense probes, and  $A$  is the cross-sectional area of the sample. The change of  $V_M$  may estimate the temperature drift of the sample is a noise source.

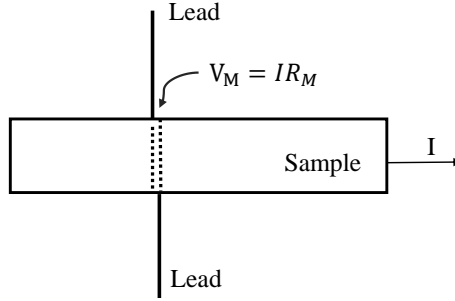


Figure 3.1: Illustration of misalignment voltage  $V_M$  caused by imperfect alignment of two Hall voltage leads.

**Thermal EMF:** thermal EMF is the small voltage caused by temperature difference. One source of such noise is the thermoelectric samples themselves with an internal temperature gradient. In the sample in which a DC current flows, there is a voltage caused by the Peltier effect parallel with the current direction; furthermore, if the sample is near a magnetic field, voltage caused by the Ettingshausen effect will be generated perpendicular to the current direction.[37] The thermal EMF may also exist at the joints of two different materials like a thermocouple. In Fig: 3.2, there are two voltage leads connecting the sample and the DC voltmeter. The temperature of the leads near the sample are  $T_1$  and  $T'_1$  while the temperature of those near the voltmeter are  $T_2$  and  $T'_2$ . The sample in this thesis is usually a semiconductor, and the leads are metal. The thermal EMF that is measured by the voltmeter is

$$V_T = S_1(T_2 - T_1) + S_o(T'_1 - T_1) + S_2(T'_1 - T'_2) \quad (3.4)$$

where  $S_o$ ,  $S_1$  and  $S_2$  are the Seebeck coefficient of the sample and the two leads. Assume  $T'_1 = T_1 + \delta T$ ,  $T_2 - T_1 = \Delta T$ , and  $T_2 = T'_2$  are the room temperature, then Eq.3.4 turns into:

$$V_T = S_o\delta T + (S_1 - S_2)\Delta T \quad (3.5)$$

which shows that the circuit behaves as a thermocouple. Ideally, if carefully choosing the materials of the connection leads and the soldering joints,  $S_1$  can be approximately equal to  $S_2$ .

Usually, the thermal EMF is detected as DC voltage, so its noise should be considered in the DC Hall measurement. When using the AC current, the direction of the current changes at a relatively high frequency compared with the steps used in the DC method. The thermal EMF related to the Peltier effect can be minimized. On the other hand, as the Hall voltage signal is an AC voltage with a certain frequency, the lock-in amplifier can

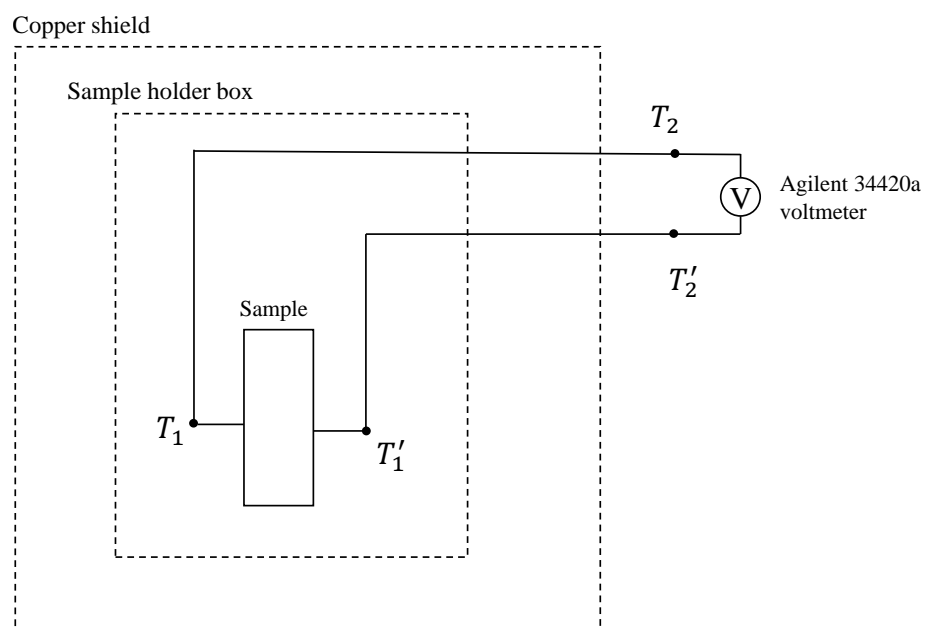


Figure 3.2: Temperature difference through the circuit may generate thermal EMF,  $V_T$ , by Seebeck effect. The sources of  $V_T$  are the thermoelectric sample and the electrical joints through the circuit.

measure the signal with narrow bandwidth at the frequency. This ignores or filters the effect of the DC thermal EMF.

**Temperature drift:** the heat sources that can change the sample temperature are the sample itself and the magnet. Usually, the thermoelectric sample is a semiconductor that has low electrical conductivity; furthermore, the contact resistance between the gold pogo pins and the sample is larger than  $1 \Omega$ . Therefore, the excitation current should be carefully selected to avoid the self-heating problem of the sample. The electromagnet is the other heat source when a large current is applied to it to provide a large magnetic field. The magnet does not have a cooling system. If it runs with  $B=0.5 T$ , the temperature inside the sample holder box can be raised by  $2 ^\circ C$  per hour, or  $0.03 ^\circ C$  per minute. If not replacing it with a water-cooling magnet, another solution would be to use a Peltier cooler combined with the PID temperature control system to stabilize the sample temperature.

**Common mode rejection ratio (CMRR):** to measure a differential voltage, There is an input  $A$  and an input  $B$ , and the measured signal is the voltage difference between  $A$  and  $B$ . [18] The gain of the two inputs  $G_A$  and  $G_B$  are ideally the same, and  $V_{\text{measure}} = G(V_A - V_B)$ ; however, there is slight difference between  $G_A$  and  $G_B$  which causes the measurement result to be  $V_{\text{measure}} = G_A V_A - G_B V_B$ .

**Interference:** The interference refers to the noise caused by sources outside the measurement circuit.[41] The common external noise sources are the high-frequency wireless network signals, the power line pickup, and the mechanical vibrations.

**Induced EMF:** In the Hall measurement, one specific external noise is the induced EMF. In this case, the loops on the aluminium sample holder have large open areas. When changing the magnetic field during the Hall measurement, the magnetic flux through the loops generated significant voltage. Therefore, the voltmeters should not start to read the voltage until the magnetic field is steady.

## 3.2 Noise level

### 3.2.1 Introduction to the noise spectrum

As discussed in the previous section, some noise sources should be considered during the Hall measurement. A simple way to distinguish the noise sources is to measure the noise spectrum by a dynamic signal analyzer, which can present the noise per  $\sqrt{Hz}$  in a certain frequency range. Fig: 3.3 is the illustration of some typical noise shown in a noise spectrum. The  $1/f$  noise is proportional to the reciprocal value of the signal frequency, which is

significant at low frequencies. The white noise is shown as a horizontal line across all frequency regions. There are some peaks at certain frequencies on the spectrum, such as the power line pickup noise at 60 Hz.

The noise spectrum presents the frequency range and the amplitude of the noise. They can also help to choose the frequency regions for the AC Hall measurement, where the noise is relatively low. The noise caused by the temperature drift, such as the thermal EMF, is considered at an extra-low frequency range, which is smaller than 0.01 Hz and may not be seen in the spectrum.

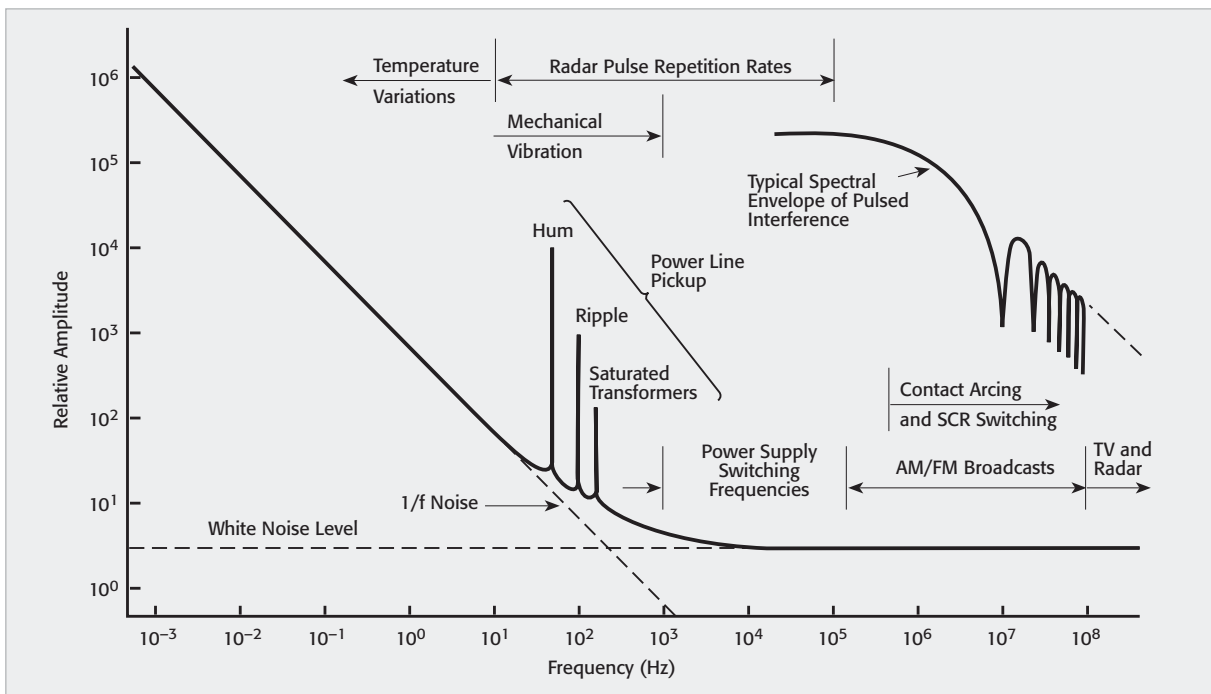


Figure 3.3: Typical voltage spectrum showing the noise at certain frequencies[19].

### 3.2.2 Spectrum analyzer

There are some noise sources in the Hall measurement which are expected to be presented in the noise spectrum: the thermal noise corresponding to the resistance the connection circuits, the ground loop, the GPIB communication, the switching of the magnetic field, and the PI temperature control.

The noise spectrum is characterized by the HP 3562a dynamic signal analyzer. The voltage from certain leads of the Hall measurement sample is increased by the PAR 113 preamplifier and then sent to the spectrum analyzer. Figure: 3.4 shows the illustration of the circuit. Remind that the extra noise from the PAR 113 preamplifier is mixed into the signal from the sample, so the noise figure (NF) of the PAR 113 should be considered.[20] The loading resistance at the input of the PAR 113 is  $10\ \Omega$ , most of which is the contact resistance between the sample and the pogo pins.

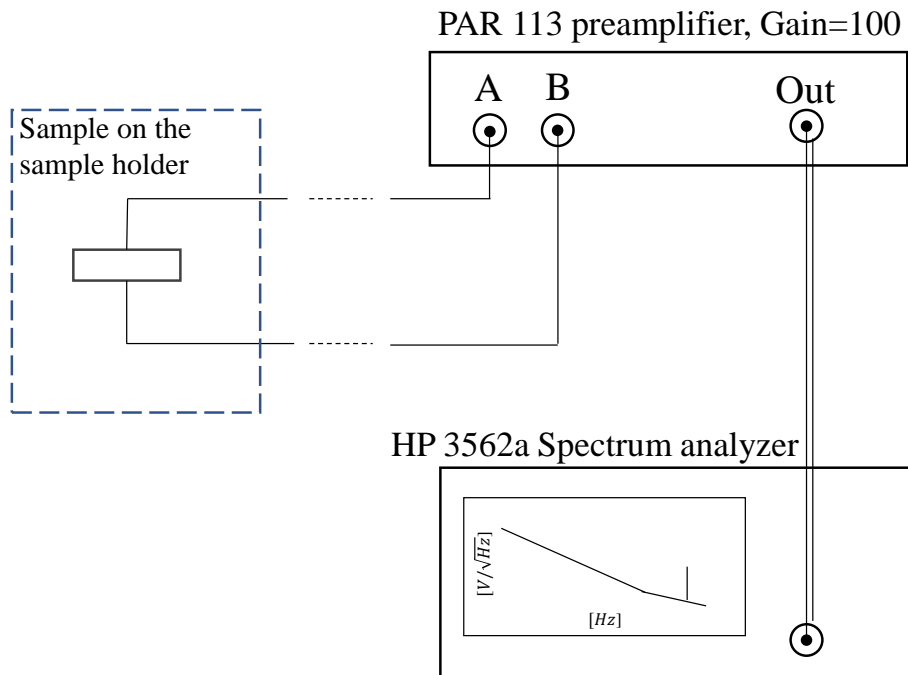


Figure 3.4: The circuit illustration of measuring noise spectrum from a sample. The signal is amplified by the PAR 113 preamplifier with  $G=100$  and DC coupling, and then sent to a HP 3562a spectrum analyzer.

### 3.2.3 Spectrum of Hall voltage leads

The noise spectrum graphs in this subsection show the noise level in both the DC and the AC Hall measurement setup. The goal is to characterize the thermal noise, the  $1/f$  noise, the thermal EMF drift at extra low frequency, and the unknown noise sources.

Fig: 3.5 shows the background noise spectrum of the Ks sample mounted on the sample holder (the orange line). “Background noise spectrum” means no instrument of the Hall measurement setup is turned on. The y-axis is the noise level in the unit of  $V/\sqrt{Hz}$  which directly analyzes the output signal of the PAR 113 preamplifier with gain  $G = 100$ . The x-axis is the frequency which is chosen to be up to  $50 Hz$ . Since the measurement frequency in AC Hall measurement is  $15.125 Hz$ , a vertical dash line is labeled in the graph to point out its position on the x-axis.

There are two blue lines in the Fig: 3.5. The solid blue line is the noise spectrum from a  $10 \Omega$  regular resistor being amplified by the PAR 113 with  $G=100$ . The blue line is the theoretical noise spectrum at the PAR 113 output with  $G=100$  and  $10\Omega$  loading resistance, which is calculated based on the noise figure information from the PAR 113 manual. The three lines have the same  $1/f$  noise trend, which indicates that the  $1/f$  noise of the orange line is caused by the PAR 113. The Ks sample shows the same noise level as a  $10 \Omega$  resistor which matches the contact resistance.

In Fig: 3.6, there are some harmonic peaks with  $nf_0 = 0.236nHz$  when running the power supply of the magnet and the PI control at the same time. While the magnet power supply is on but the PI control is not running, the harmonic peaks are insignificant. At the frequencies below  $1 Hz$ , the noise of the harmonic peaks is about four times as large as the thermal noise of a  $10 \Omega$  resistor at room temperature, which is about  $1.6 nV/\sqrt{Hz}$ ; it is much smaller than the DC voltage reading noise of the Agilent 34420a nano-voltmeter. At  $f = 15.125 Hz$ , the frequency of the AC Hall measurement, the noise level is almost the same as the thermal noise. Therefore, the harmonic peaks might cause large uncertainty in the DC Hall measurement but not in the AC Hall measurement.

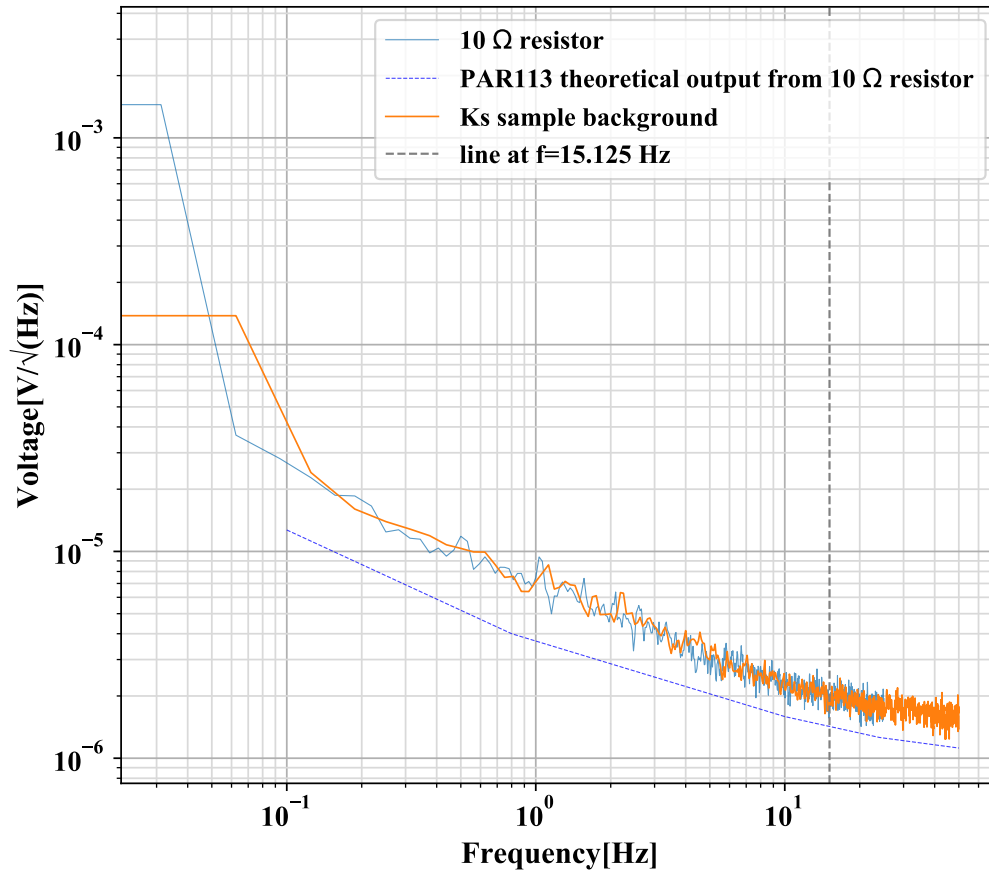


Figure 3.5: The background spectrum of the Ks sample mounted on the sample holder compared to that of a 10  $\Omega$  resistor. The signal from the sample is amplified by the PAR 113 preamplifier with  $G = 100$ . The 1/f noise is caused by the PAR 113.

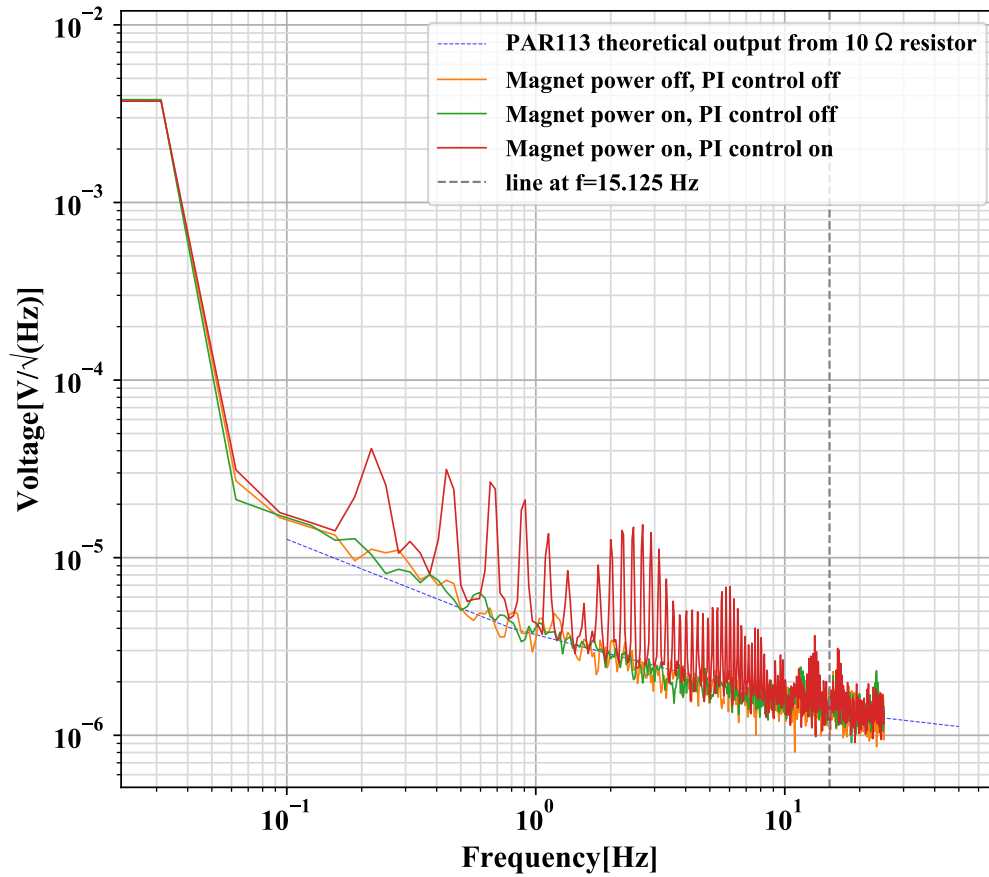


Figure 3.6: The spectrum of the Ks sample if the magnet power supply is on or not, and if the PI control is running or not. The harmonic peaks are significant when magnet power supply and PI control are running at the same time.

To make sure if the harmonic peaks are caused by the thermoelectric properties of the sample, a graphite sample was used in the tests in Fig: 3.7. Considering the computer and the magnet power supply are dirty power sources, optical fibers were used to isolate them from the rest of the instruments. Because the harmonic peaks appear when there is communication through GPIB, more tests were done focusing on the GPIB connections. The first test was to disconnect the GPIB cable to the magnet power supply and run the PI control program. The magnet power supply was on during the test. As the orange line in Fig: 3.7, there were no harmonic peaks seen. The second test was to connect the GPIB cable to the magnet power supply and then repeated the first test. There were some significant harmonic peaks seen, shown as the green line. Comparing the first and the second test, there might be noise sent to the magnet power supply through the GPIB cable which caused the peaks. The third test was to unplug the BNC-2110 accessory and repeat the second test, shown in the red line. The harmonic peaks dropped to a small level. Based on the tests shown in Fig: 3.7, the source of the harmonic peak was the NI-PCI 6251 DAQ interface (NI 6251) and NI BNC-2110 accessory (BNC-2110).

The possible reason for the problem was the computer noise passing through the GPIB cable. The BNC-2110 was the +5V voltage source to the dual cold junction compensator directly from the computer, so they shared the same ground. The computer is considered as the high noise source whose ground should be separated from those of noise-sensitive instruments.[27] When the GPIB communication was running, the noise was sent through the GPIB cables, which caused noise starting at 0.237 Hz.

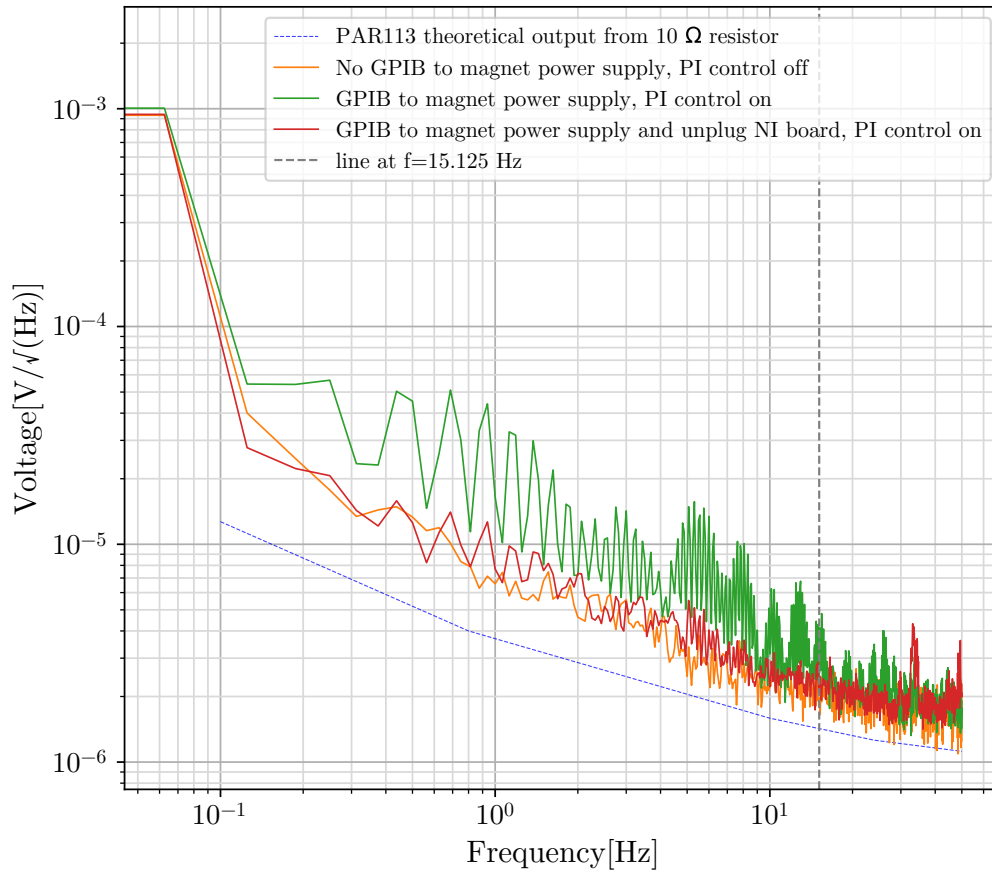


Figure 3.7: The spectrum of graphite sample when observing GPIB low frequency noise. The harmonic peaks (green line) proves the sample is not the noise source. Unplugged the BNC-2110/NI-PCI 6251 DAQ lowered the noise.

Agilent E3610A was then used as a +5 V DC voltage source instead of BNC-2110. Fig: 3.8 shows the spectrum of the Ks sample after fixing the GPIB problem. When running the PI control with the magnet power supply turned on (green line), there were no significant harmonic peaks detected. To characterize the noise down to 0.01 Hz, the figure combines the scan in 0.01~1 Hz and 1~50 Hz. The three lines from the experiment have the same trend as the blue line from the PAR 113 manual, which is the 1/f noise caused by the PAR 113. In conclusion, the temperature control does not introduce visible external noise to the Hall measurement.

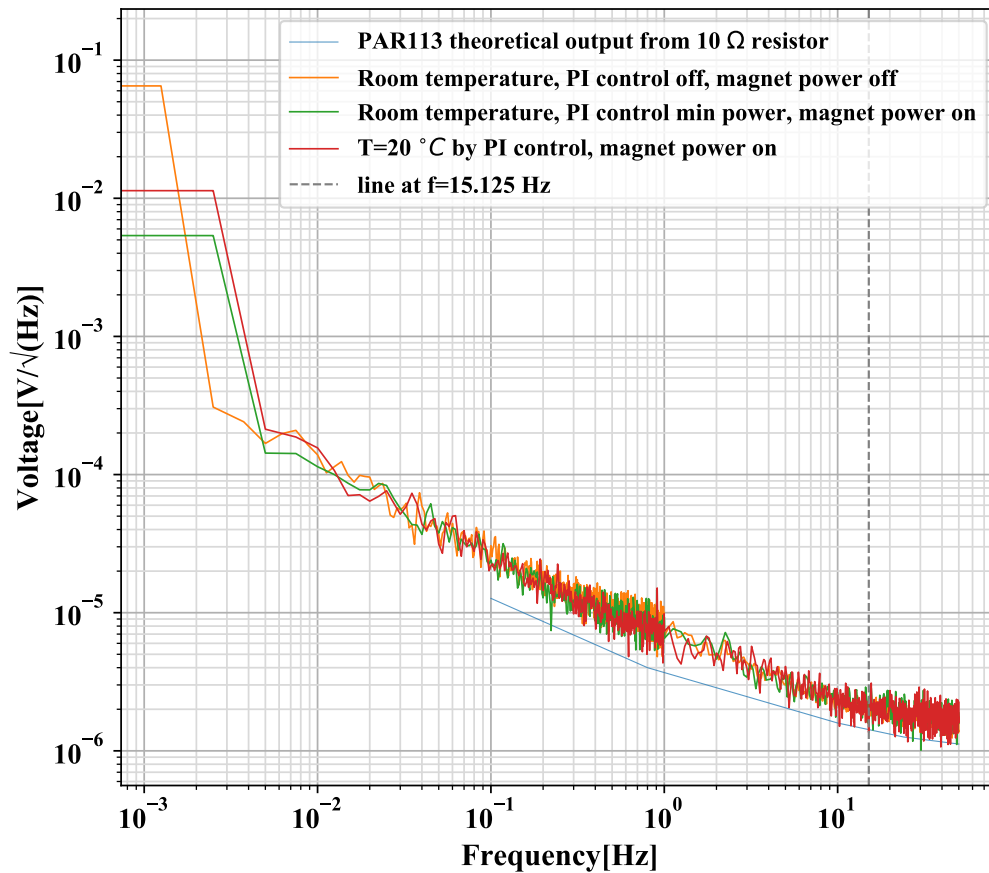


Figure 3.8: The spectrum of Ks sample after fixing the GPIB problem. The scan frequency combines 0.01~1 Hz and 1~50 Hz. The three lines overlap each others, which shows the temperature drift around the sample does not cause extra 1/f noise.

Fig: 3.9 and Fig: 3.10 show that the change of magnetic field during the Hall measurement can cause large noise starting at  $f = 20 \text{ Hz}$ . It is the magnetic EMF from changing the magnetic field.

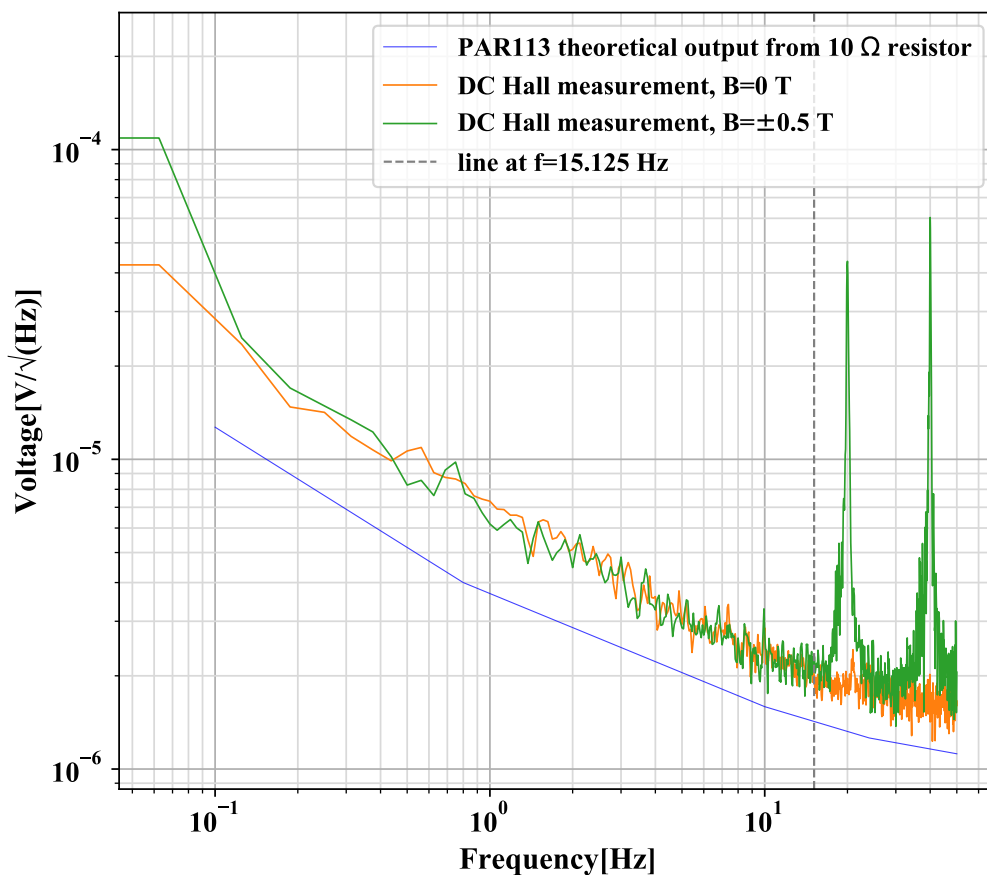


Figure 3.9: The spectrum of Ks sample when running the DC Hall measurement program. Switching magnetic field caused significant magnetic EMF noise peaks at  $f = 20 \text{ Hz}$  and  $40 \text{ Hz}$ .

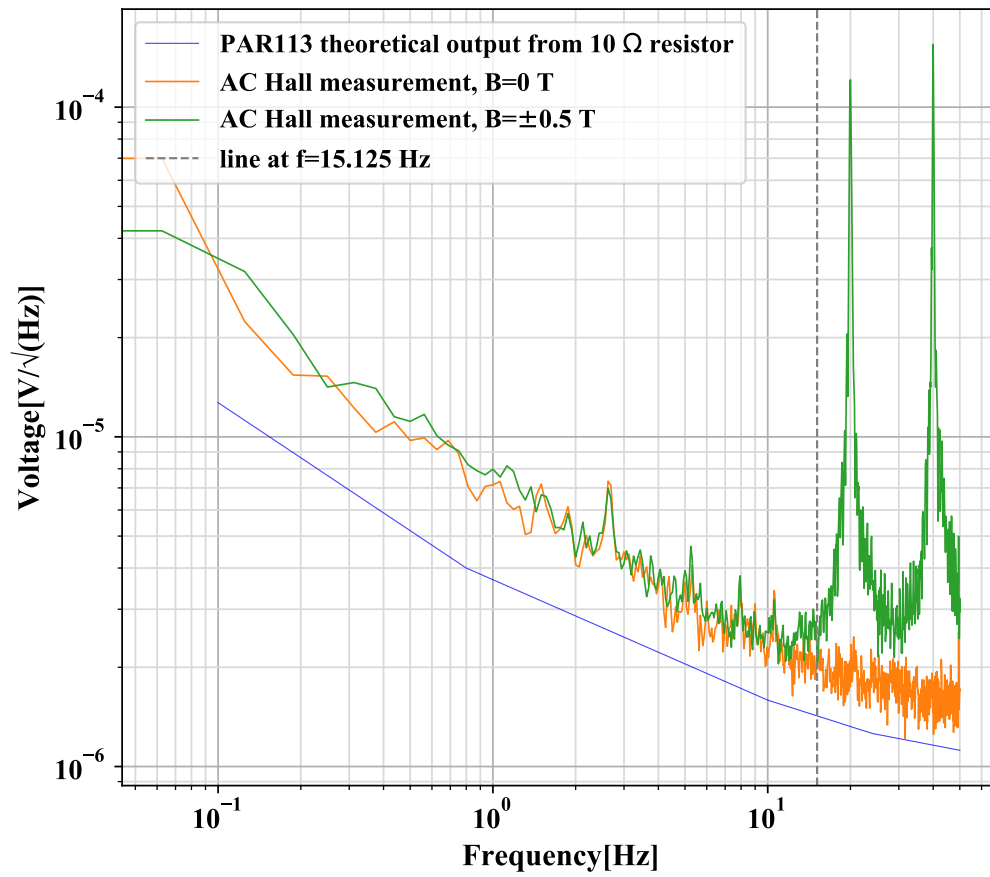


Figure 3.10: The spectrum of Ks sample when running the AC Hall measurement. Switching magnetic field causes significant noise with  $f = 20$  Hz.

### 3.2.4 Conclusions from the spectrum

Significant low-frequency noise was generated by running the PI temperature control and the magnet power supply simultaneously. The solution was to remove NI-PCI 6251 DAQ interface (NI 6251) and NI BNC-2110 accessory (BNC-2110) from the measurement setup.

The results from the spectrum showed that after fixing the GPIB problem, the noise level from the sample was similar to the thermal noise of a  $10\ \Omega$  resistor in the frequency range  $0.01\sim 50$  Hz. The  $1/f$  noise presented in the spectrum was caused by the PAR 113 preamplifier.

At  $f = 15.125\text{Hz}$ , the frequency in the AC Hall measurement, the noise from the sample is  $0.4\ \text{nV}/\sqrt{\text{Hz}}$ . The magnetic EMF is a significant noise source starting at  $f = 20\ \text{Hz}$  when changing the DC magnetic field. The solution is to delay the voltage reading in the Hall measurement until the magnetic field is steady.

The noise spectrum does not show temperature dependence. Therefore, the temperature control does not introduce noise to the Hall measurement.

# Chapter 4

## Hall measurement results and discussion

This chapter discusses the Hall measurement results. The experiment results of a thermoelectric sample, sample Ks, by both the DC and the AC Hall measurements are shown for comparing different methods. The sources of errors are also characterized and analyzed in this chapter.

### 4.1 Temperature dependence of the electrical resistivity

This section is to study the temperature dependence of the electrical resistivity of the sample Ks. The temperature change of the sample can be estimated by measuring the sample's real-time resistance.

The sample was mounted on the sample holder and connected to the AC Hall measurement setup without the transformer. The current leads were the lead *A* and lead *B* shown in the Fig: 2.1, and the voltage leads were lead *C* and lead *D*.  $I = 3.0 \text{ mA}$  and  $B = 0 \text{ T}$ . The voltage  $V_R$  between lead *C* and lead *D* was measured by the SR 830 lock-in amplifier. The temperature range was 17 °C to 21 °C controlled by the PI temperature control system.

From the measurement, the sample resistance  $R[\Omega]$  at temperature  $T[^\circ\text{C}]$  followed:

$$R = \frac{V_R}{I} = 1.28 \times 10^{-4}T + 1.95 \times 10^{-2} \quad (4.1)$$

The electrical resistivity  $\rho$  of the sample at  $20\text{ }^\circ\text{C}$  is  $\rho_0 = 3.51 \times 10^{-3}\ \Omega \cdot \text{cm}$ ; therefore, at room temperature,  $\rho$  follows:

$$\rho(T) = \rho_0 + 2.04 \times 10^{-5}(T - 20\text{ }^\circ\text{C})$$

In room temperature range,  $\rho$  increases 0.58% if temperature increases  $1\text{ }^\circ\text{C}$ .

Another test was to measure the electrical resistivity of sample Ks at  $T=20.5\text{ }^\circ\text{C}$  with different excitation current. The goal of the test is to find the best excitation current with small self-heating of the sample. The temperature dependence of  $\rho$  was used to monitor the self-heating of the sample. The result in Fig: 4.1 showed that the sample might be significantly overheated when  $I > 15\text{ mA}$ . Therefore, the excitation current was chosen to be  $12\text{ mA}$  for most of the tests.

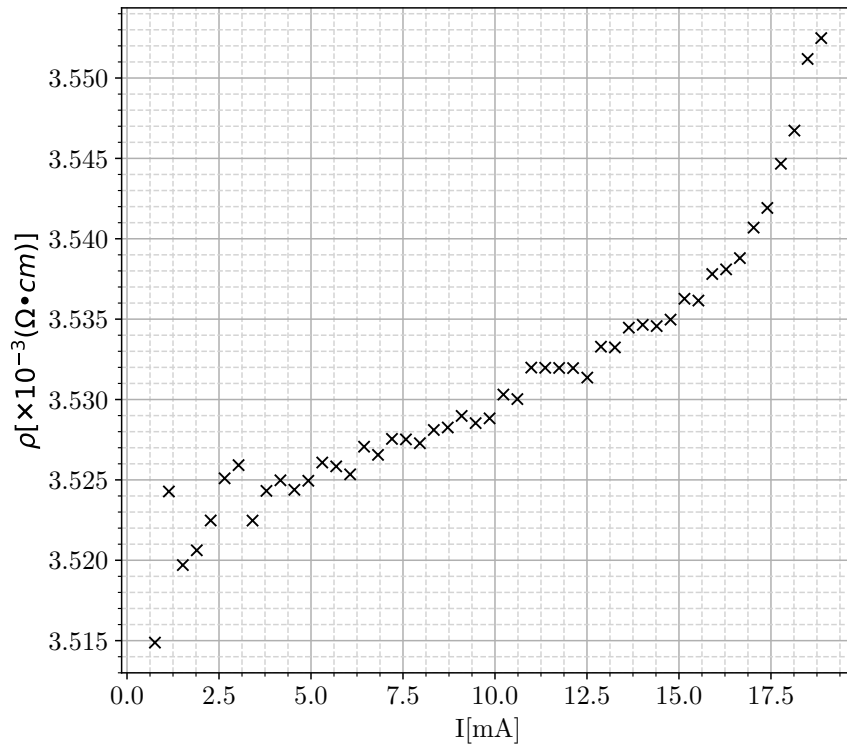


Figure 4.1: The electrical resistivity of sample Ks at  $T=20.5\text{ }^\circ\text{C}$  with different excitation currents.  $\rho$  changes quickly when  $I > 15\text{ mA}$ , so  $I = 12\text{ mA}$  was chosen as the best excitation current.

## 4.2 DC Hall measurement

### 4.2.1 Noise from thermal EMF

The assumption is that the thermal EMF,  $V_T$ , is from both the sample and the electronic leads to the sample. Fig: 4.2 is the temperature dependence measurement of thermal EMF using sample Ks. Neither the excitation current nor a magnetic field was applied, so the DC voltage  $V_{\text{raw}}$  measured by the Agilent 34420a nano-voltmeter was the sum of total thermal EMF  $V_T$  and the intrinsic voltage offset of the nano-voltmeter. Since there was no heat from the magnet,  $\Delta T = T_{\text{room}} - T_{\text{sample}}$ , and room temperature  $T_{\text{room}} = 20.85 \text{ }^\circ\text{C}$ .

Shown in Fig: 4.2, in the first 20 minutes, the PI control was not running. The sample holder box was slowly cooled down from  $20.85 \text{ }^\circ\text{C}$  to  $20.75 \text{ }^\circ\text{C}$ . Then, the PI temperature control changed the sample holder temperature to  $20.0 \text{ }^\circ\text{C}$ ,  $19.0 \text{ }^\circ\text{C}$  and  $18.0 \text{ }^\circ\text{C}$ . The voltage from the Hall voltage leads was continuously recorded, shown as the purple points. The voltage points show  $0.05 \text{ } \mu\text{V}$  peak-to-peak noise, or  $0.02 \text{ } \mu\text{V}$  RMS noise, which is due to the input noise of the voltmeter. The RMS noise could be lowered by averaging multiple data points. The solid purple line is the average result of 50 adjacent voltage data points. When the sample holder temperature decreased by  $1 \text{ }^\circ\text{C}$  per stage, the thermal EMF increased as  $\Delta V_T = (0.48 \mu\text{V}/^\circ\text{C})\Delta T$ .

Even if the temperature was well stabilized by the PI temperature control, the thermal EMF was still seen to be drifting. Fig: 4.3 is the zoom-in version of Fig: 4.2 during the time region 30~46 minute.  $T_s = (20.00 \pm 0.01)^\circ\text{C}$  and  $V(50 \text{ points average}) = (0.47 \pm 0.01) \text{ } \mu\text{V}$ . If choosing the voltage points with 1-minute interval and calculating the result of  $1/4(V_1 - V_2 - V_3 + V_4)$ , there will be  $\pm 2 \text{ nV}$  uncertainty which is usually considered as the noise of  $V_H$ . Knowing that  $B = 0 \text{ T}$  during the measurement, the  $\pm 2 \text{ nV}$  was a “fake”  $V_H$  signal; however, this signal is usually mistakenly counted in a real DC Hall measurement.

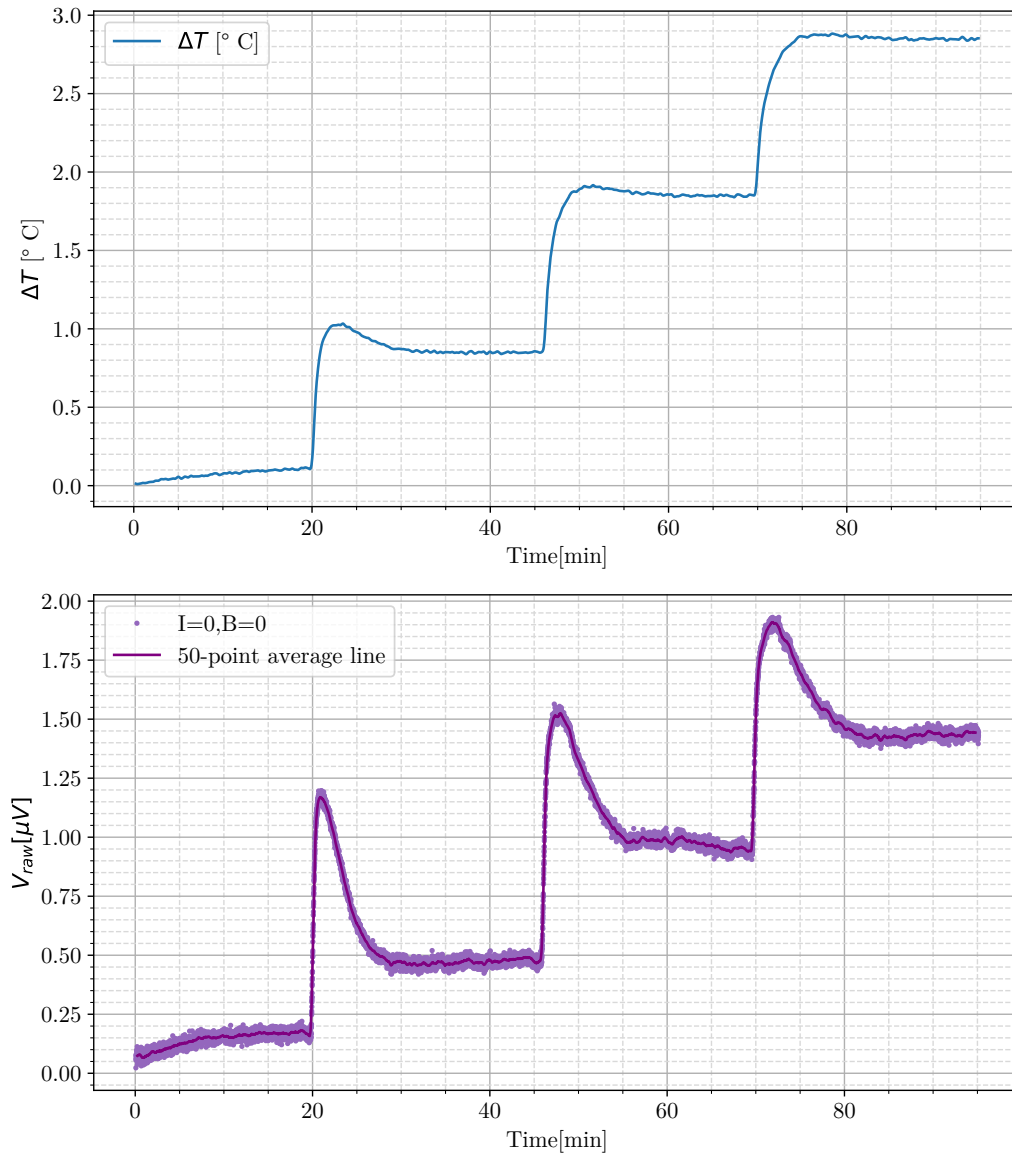


Figure 4.2: Thermal EMF measurement of sample Ks at different temperatures.  $\Delta T = T_{\text{room}} - T_{\text{sample}}$  and  $T_{\text{room}} = 20.85 \text{ }^\circ\text{C}$ . In the lower part,  $V_{\text{raw}} = V_T + V_{\text{offset}}$  which is shown as purple points. The purple line is the smoothed line calculated from the average of every adjacent 50 data points.

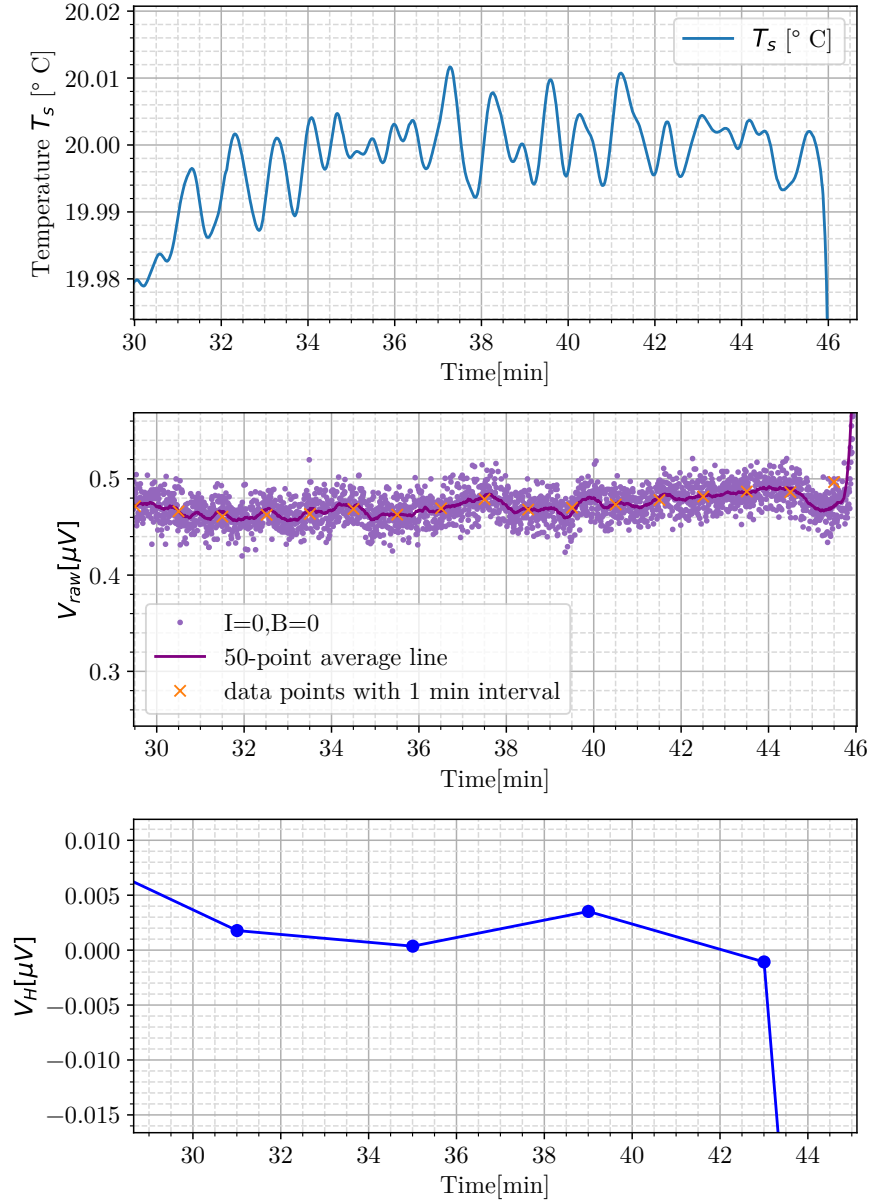


Figure 4.3: Thermal EMF measurement of sample Ks at 20.0 °C, with  $I = 0$  and  $B = 0$ . The figure is the zoom-in version of 30 ~ 46 min of Fig: 4.2. Ideally, the  $V_H$  should be zero because of no excitation current or magnetic field being applied; however, the calculated  $V_H$  are in  $\pm 2$  nV due to the drifting  $V_T$ .

Described by 3.5, a 50%*Pb* – 50%*Sn* soldering alloy sample and a graphite sample were tested within the same method. The goal was to measure the thermal EMF from the leads. The two samples had the same geometry as sample Ks. They have high thermal conductivity, high electrical conductivity, and weak thermoelectric behaviors. The voltage signal measured by the Agilent 34420a nano-voltmeter at different temperatures is shown in Fig: 4.4 to compare to the result when using sample Ks. From the figure,  $\Delta V = 0.2\mu V/^{\circ}C\Delta T$  when using the soldering sample and the graphite sample;  $\Delta V = 0.48\mu V/^{\circ}C\Delta T$  when using the thermoelectric sample Ks. Furthermore, when  $\Delta T = 0^{\circ}C$ , the voltage of the voltmeter is not always zero. It shows that there was  $0.28\mu V/^{\circ}C\Delta T$  thermal EMF caused by sample Ks,  $0.2\mu V/^{\circ}C\Delta T$  thermal EMF caused by the leads through the circuit, and  $\pm 0.05\mu V$  offset from the voltmeter.

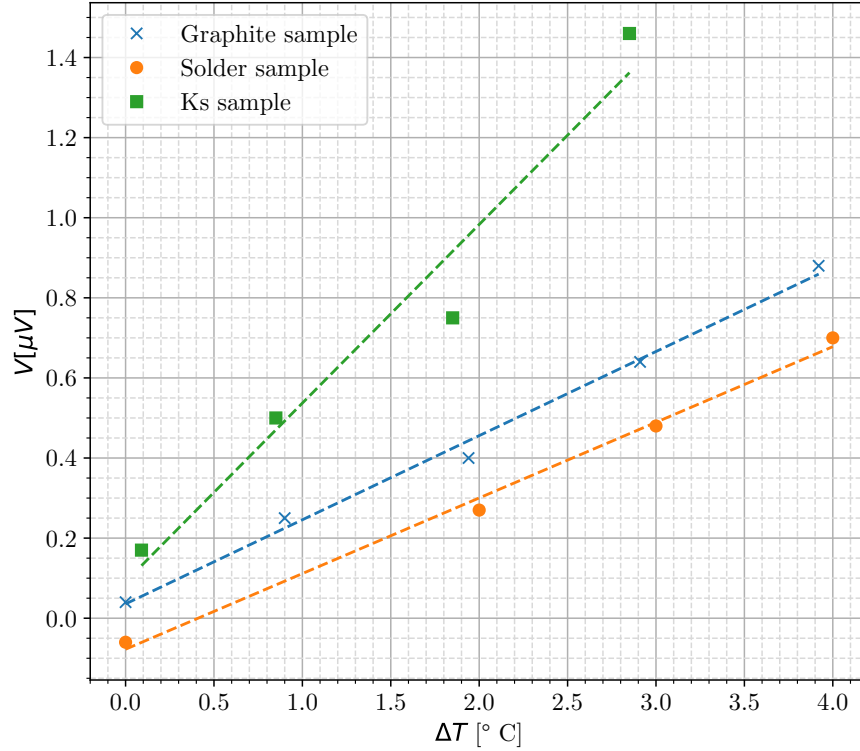


Figure 4.4:  $V_T$  of three samples, measured by Agilent 34420a voltmeter.  $\Delta T = T_{\text{room}} - T_{\text{sample}}$ . Thermoelectric sample Ks has higher  $V_T$  than non-thermoelectric solder sample and graphite sample. The  $V_T$  when using non-thermoelectric samples may be caused by the thermocouple effect of the contacts within the leads.

## 4.2.2 DC Hall measurement - before fixing the GPIB problem

Fig: 4.5 shows the measured voltage signal of sample Ks in a DC Hall measurement before fixing the GPIB problem. The excitation current  $I = 12 \text{ mA}$  and the magnetic field  $B = 0.5 \text{ T}$ . The sample holder temperature  $T_s$  drifted in the first 20 measurement cycles, or 104 minutes, without temperature control; then, the PI temperature control started to stabilize the  $T_s$  to  $26.0 \text{ }^\circ\text{C}$ .

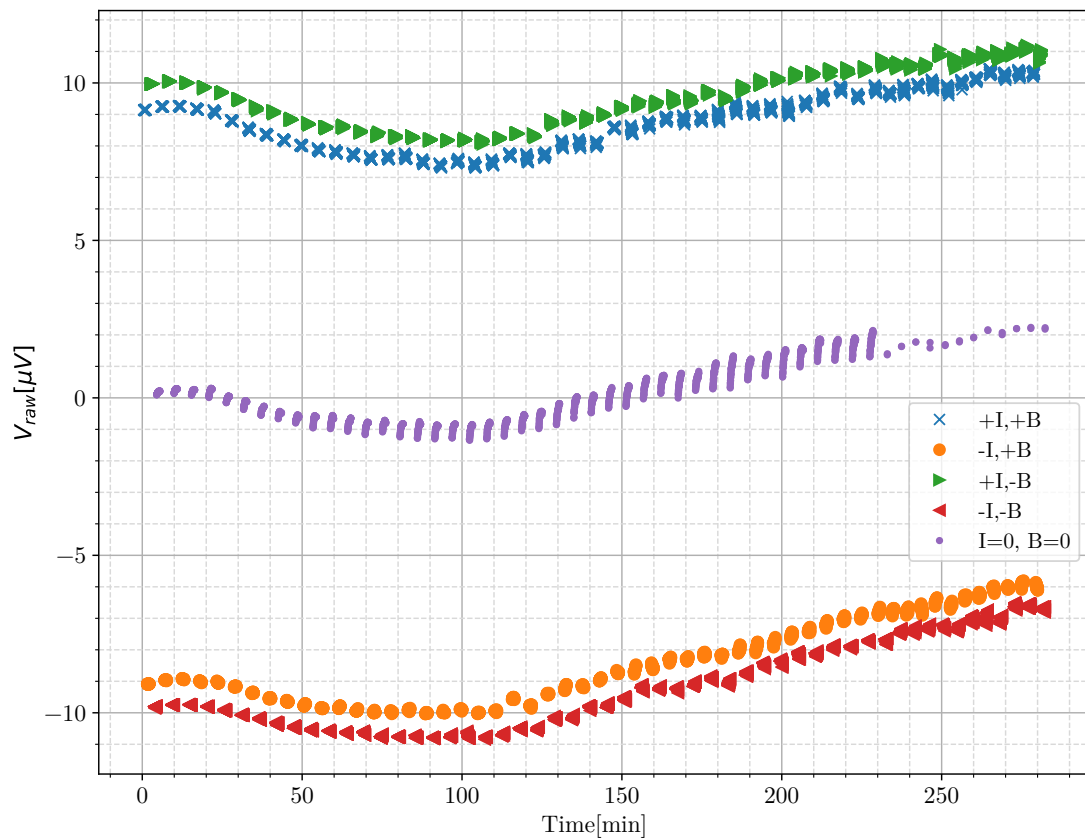


Figure 4.5: Voltage signal measured in DC Hall measurement. The PI temperature control did not work in the first 100 minutes, and then started to control  $T$  to  $26.0 \text{ }^\circ\text{C}$ .

The calculation result is shown in Fig: 4.6.  $R_H = (8.07 \pm 0.03) \times 10^{-8} V.m/AT$  without temperature control, and  $R_H = (8.10 \pm 0.08) \times 10^{-8} V.m/AT$  with temperature control.  $V_H = (-381 \pm 12) nV$  without temperature control, and  $V_H = (-382 \pm 39) nV$  with temperature control.

Fig: 4.6(e) shows that sample holder temperature  $T_s$  was controlled after 100 minutes; however,  $V_M$  drifts with the same speed, which means that the sample temperature was not effectively controlled. It might be the reason why the measurement uncertainty of  $R_H$  with temperature control is higher than that without temperature control.

Here is the calculation of uncertainty caused by the reading noise of the nano-voltmeter. The Agilent 34420a nano-voltmeter had [NPLC](#) set to 10, and its digital and analog filters were turned off. It caused 11  $nV$  RMS noise for each voltage reading. Therefore, the total noise is 1.7  $nV$  for an average of 40 reading points.  $V_H$  is at least ten times larger than the reading noise from the voltmeter, whether there was temperature control or not. In conclusion, the nano-voltmeter was not the main noise source of the large measurement uncertainty.

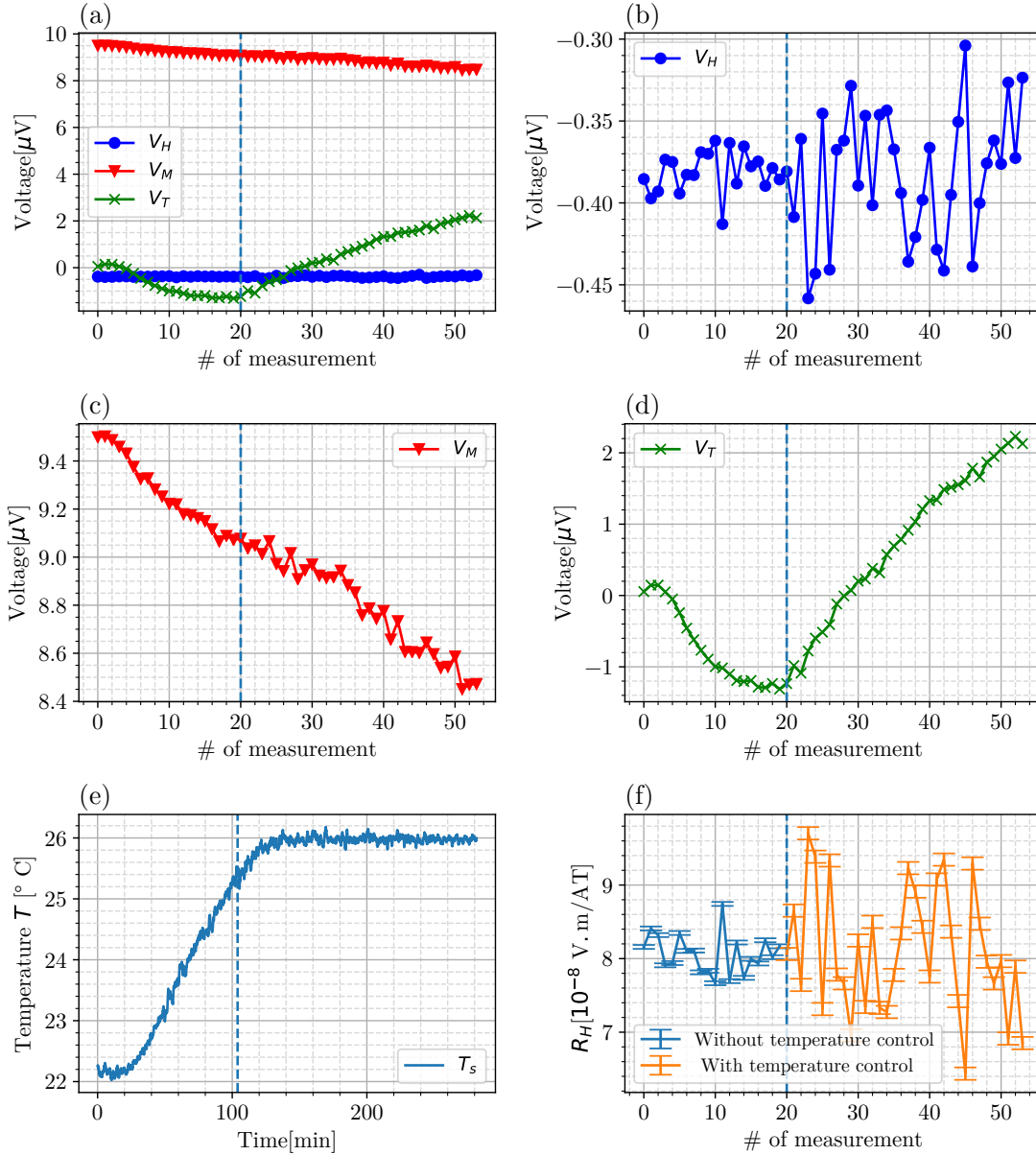


Figure 4.6: Calculation result of the Hall measurement in Fig: 4.5 before fixing the GPIB problem. (a)-(d) are the Hall voltage  $V_H$ , misalignment voltage  $V_M$  and thermal EMF  $V_T$  of the DC Hall measurement. (e) is the temperature in the sample holder box which rises in the first 100 minutes; the PI temperature control starts to work at  $t = 100 \text{ min}$  which stabilizes  $T$  to be  $26 \text{ }^{\circ}\text{C}$ . (f) shows the  $R_H$  during the measurement. (b) and (f) shows that in this situation, using PI temperature control causes higher measurement uncertainty than not using it.

### 4.2.3 DC Hall measurement - after fixing the GPIB problem

A DC Hall measurement of sample Ks was repeated after fixing the GPIB problem, with excitation  $|I|=12$  mA and  $|B|=0.5$  T. The raw voltage is shown in Fig: 4.7. In the first 150 minutes, the measurement was under the PI temperature control at  $(19.81\pm 0.01)$  °C. At time  $t=150$  minute, the PI temperature control was stopped, and the sample holder temperature drifted to room temperature. The calculation results of  $V_H$ ,  $V_M$ ,  $V_T$ , and  $R_H$  are shown in Fig: 4.8. In Fig: 4.8(b),  $V_H = (-398.4\pm 4.2)$  nV with temperature and  $V_H = (-396.3\pm 4.3)$  nV without temperature control. The temperature control is not seen to not significantly improve the uncertainty of the  $V_H$ . Fig: 4.8(c) shows that  $V_M$  stayed at  $-13.7$   $\mu$ V when PI temperature control was on, and drifted from  $-14.0$   $\mu$ V to  $-14.3$   $\mu$ V when temperature changed from  $26.0$  °C to  $30.0$  °C. In Fig: 4.8(e), the temperature was  $(19.81\pm 0.007)$  °C in the first 26 cycles and drifted quickly from  $19.8$  °C to  $26$  °C from the 26th to the 30th cycle; after that, the temperature drifts up linearly along with time as  $(+0.17\pm 0.036)$  °C per cycle. With the temperature being controlled in the range of  $(19.81\pm 0.01)$  °C, the noise caused by  $V_M$  should be  $\pm 0.8$  nV.

The drift of  $V_M$  and  $V_T$  may cause the dominant noise sources. When the temperature control was on,  $V_M = (-13666\pm 4.3)$  nV and  $V_T$  rose along with time with the average rate  $+71\pm 30.5$  nV in 5 minutes. When the temperature control was off,  $V_M$  changed smoothly at the rate of  $-8\pm 6.8$  nV in 5 minutes while  $V_T$  changed at the rate of  $+52\pm 46$  nV in 5 minutes. When without temperature control, both the drift and the uncertainty of  $V_M$  were smaller than those of  $V_T$ . From Fig: 4.3, the stabilized  $V_T$  in  $\pm 0.05\mu$ V can still cause  $\pm 3$ nV uncertainty in the calculation of  $V_H$ . The drifting  $V_T$  may have caused a similar or higher level of uncertainty in the DC Hall measurement. Furthermore,  $V_T$  in Fig: 4.8 kept drifting whether temperature control was working or not. It may be because the working magnet created a large amount of heat, which raised the temperature inside the copper shield room. The temperature gradient within the Hall measurement circuit may have changed as well, which caused the drifting  $V_T$ . Even if there might be a perfect temperature control of the sample holder box, the  $V_T$  caused by the thermocouple effect elsewhere would not be reduced. A water-cooling magnet or a permanent magnet may reduce the temperature drift and then reduce the noise caused by  $V_T$ . Applying temperature control on every part of the circuit may be another solution but not cost-efficient.

From the experiment,  $R_H = (8.43\pm 0.0092) 10^{-8}$  V.m/AT with the temperature control on and  $R_H = (8.39\pm 0.0094) 10^{-8}$  V.m/AT with the temperature control off. The standard error(n=100) of  $R_H$  is 0.11 % for both conditions. If there was a better temperature control system in which the temperature for the whole setup was kept constant during the measurement, then the thermal EMF noise would be canceled out by math; the dominant

noise sources would be the noise of excitation current and the input noise of the nano-voltmeter, which are  $\pm 1.7 \text{ nV}$  in total. The theoretical standard error of  $R_H$  would be 0.04 % in this ideal situation.

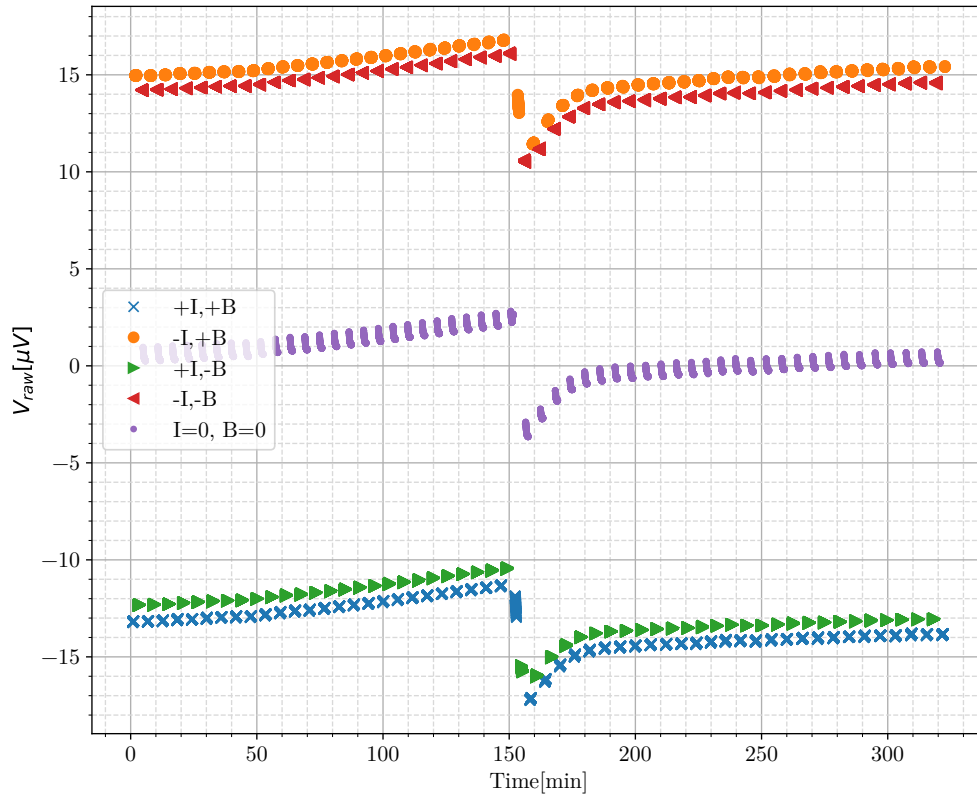


Figure 4.7: Raw voltage data of DC Hall measurement after fixing the GPIB problem. The temperature was controlled to  $19.8 \text{ }^\circ\text{C}$  before time  $t=150 \text{ min}$ , and the temperature control was off after  $t=150 \text{ min}$ . The  $V_{\text{raw}}$  spike at  $150 \text{ min}$  was due to suddenly turning off the temperature control

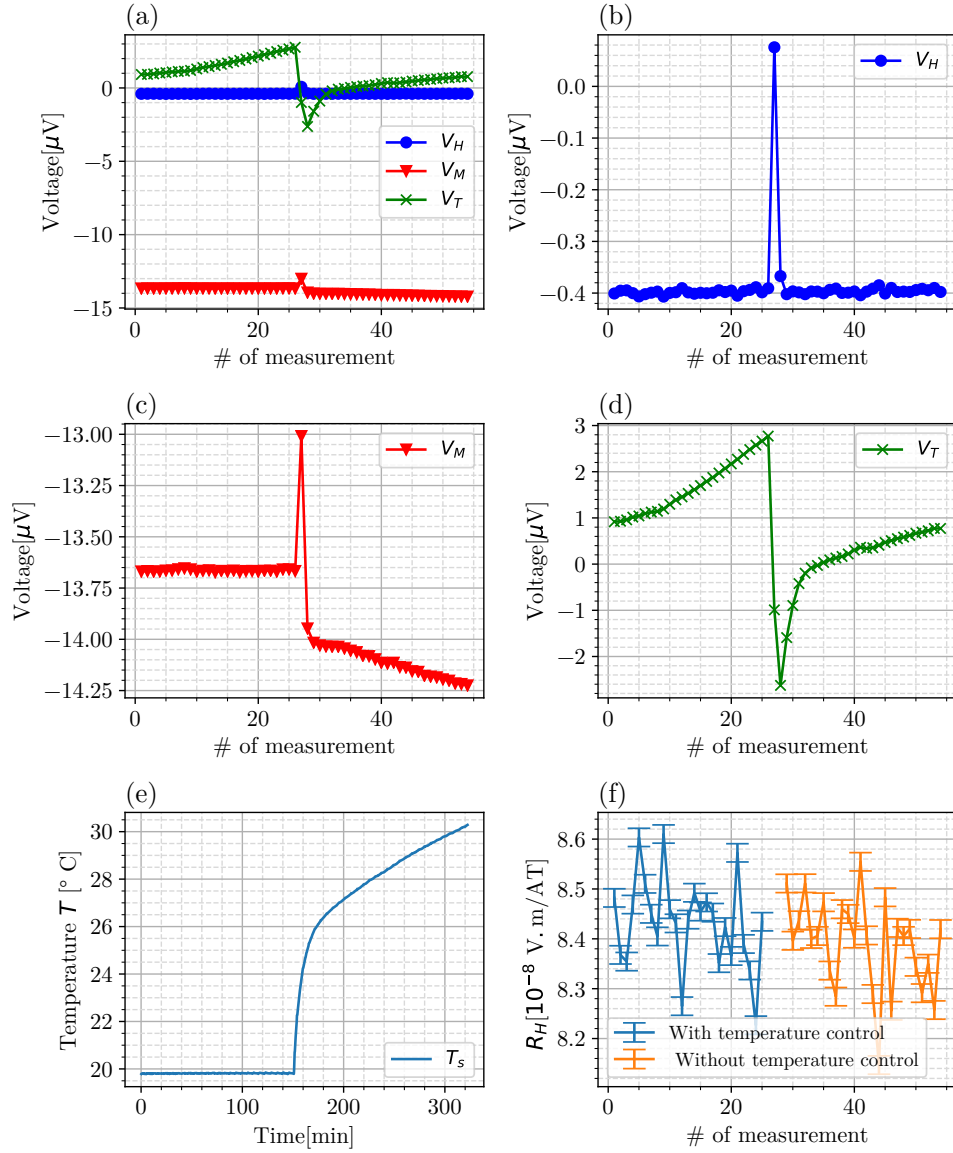


Figure 4.8: Voltages in the DC measurement, with and without temperature control after fixing the GPIB problem. (a)-(d) are the  $V_H$ ,  $V_M$  and  $V_T$  of the DC Hall measurement. The spike was caused by turning down the PI temperature control. (e) the temperature was at 20  $^{\circ}\text{C}$  in the first 150 minutes with the temperature on and rose to 30  $^{\circ}\text{C}$  the temperature control off. (f) shows  $R_H = (8.43 \pm 0.0092) \times 10^{-8} \text{ V}\cdot\text{m}/\text{AT}$  with the temperature control on and  $R_H = (8.39 \pm 0.0094) \times 10^{-8} \text{ V}\cdot\text{m}/\text{AT}$  without the temperature control. The temperature control did not improve the measurement uncertainty because of the drifting  $V_T$

## 4.3 AC Hall measurement

The AC Hall measurement has two benefits compared with the DC Hall measurement. One is that it can take advantage of using the lock-in amplifier. The noise from the drifting  $V_T$  at low frequency can thus be significantly reduced or ignored. The other benefit is its capacity to use a low noise transformer, which increases the signal-to-noise ratio.

The SR 830 lock-in amplifier has  $24 \text{ nV}/\sqrt{\text{Hz}}$  input noise, measured by its own noise reading function at  $f = 15.125 \text{ Hz}$ . The total input noise is  $24 \text{ nV}/\sqrt{\text{Hz}}$  where the input noise of the lock-in amplifier is dominant. Usually, its effective noise bandwidth  $ENBW = 0.26 \text{ Hz}$ , which brings the noise to  $1.9 \text{ nV}$  after averaging 40 points.

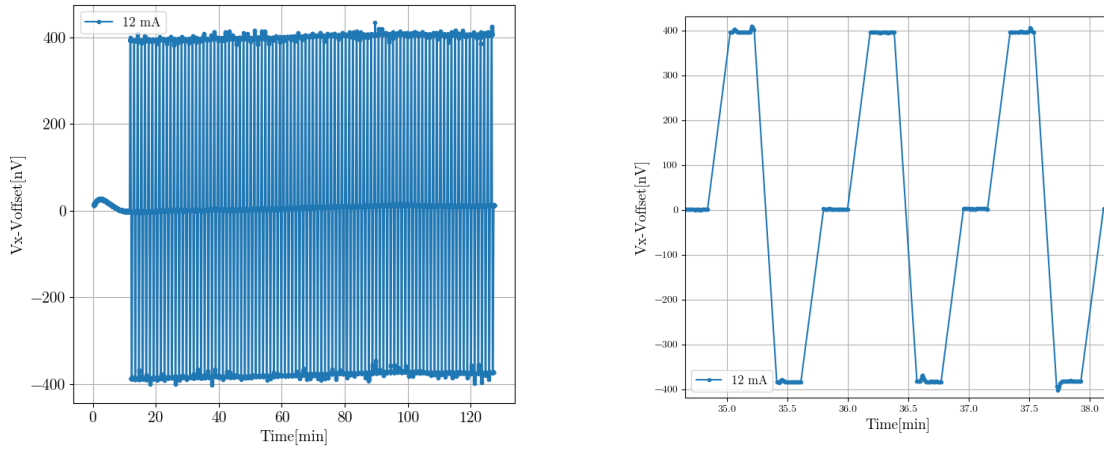
### 4.3.1 AC measurement with the transformer

To increase the signal-to-noise ratio, a PAR 190 transformer was used to amplify the sample signal. The noise at the input of the transformer is dominated by the thermal noise from the sample-pin contact resistance, which is  $0.4 \text{ nV}/\sqrt{\text{Hz}}$ .

Here is the calculation of the theoretical electronic noise limit. When using the transformer with a gain  $G = 100$ , the RMS noise at the transformer output is  $70 \text{ nV}/\sqrt{\text{Hz}}$  at  $f = 15.125 \text{ Hz}$ . Therefore, the total input noise of the lock-in amplifier is  $74 \text{ nV}/\sqrt{\text{Hz}}$ , which is reduced to  $38 \text{ nV}$  with  $ENBW = 0.26 \text{ Hz}$ . The excitation current causes  $30 \text{ nV}$  noise which is usually considered as the misalignment voltage. After taking the transformer gain into account, the noise, referred to the input of the transformer, is  $0.06 \text{ nV}$  after averaging 32 points, or  $0.08 \text{ nV}$  after averaging 20 points.

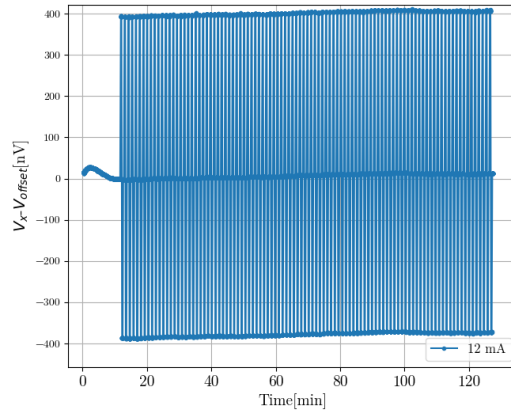
Fig: 4.9 shows the voltage during the AC Hall measurement with the transformer, and  $T_s = 23 \text{ }^\circ\text{C}$ . From the Fig: 4.9a, the Hall voltage  $V_H = (385.8 \pm 0.7) \text{ nV}$ . The voltage uncertainty from the experiment is about eight times of that found by the theoretical calculation. The Fig: 4.9b zooms in the Fig: 4.9a around  $Time = 36 \text{ min}$ . There are some glitches at the level of  $10 \text{ nV}$  which indicates another noise source exists. The glitches only exist when B is not zero. Therefore, its source might be the changing magnetic flux picked up by the measurement circuit. Considering the time constant and the  $ENBW$  of the lock-in amplifier are  $0.3 \text{ s}$  and  $0.26 \text{ Hz}$ , a sudden magnetic EMF point causes about 10 consecutive data points to leave the average voltage level. The ten maximum points and ten minimum points in each cycle steps are removed to clean the error caused by the glitches. Fig: 4.9c shows the voltage signal after cleaning the glitches, and the Hall voltage  $V_H = (385.8 \pm 0.3) \text{ nV}$ . Compared the uncertainty of  $V_H$  in Fig: 4.9a with that in

Fig: 4.9c, the noise from the magnetic EMF was reduced by  $0.6 \text{ nV}_{RMS}$ . However, the new uncertainty is still three times larger than that from the prediction.



(a) Noisy voltage signal caused by magnetic EMF. The glitches exist when  $B = \pm 0.5 \text{ T}$  but not  $0 \text{ T}$ , which indicates significant magnetic EMF noise.

(b) Zoom-in graph around Time  $t = 36 \text{ min}$  of part(a). There are some magnetic EMF glitches at  $t = 35.2 \text{ min}$ ,  $35.4 \text{ min}$ ,  $36.6 \text{ min}$ ,  $37.5 \text{ min}$  and  $37.3 \text{ min}$ .



(c) After cleaning the magnetic EMF glitches by programming

Figure 4.9: The raw voltage data of the AC Hall measurement with the transformer. (a) and (b) show the glitches from the magnetic EMF; (c) shows the voltage graph after cleaning the glitches by programming.  $V_{\text{offset}} = +7.697 \text{ } \mu\text{V}$

Fig: 4.10 are the  $I$ ,  $V_+$ ,  $V_-$ ,  $V_H$ ,  $T_s$ , and  $R_H$  of the measurement in Fig: 4.9c.  $V_M = 38.48 \mu V$  at the beginning of the first measurement cycle, and the misalignment resistance  $R_M = 3.205 m\Omega$ . Fig: 4.10(a) shows that the excitation current changed between  $12.007 mA$  and  $12.013 mA$  during the 100 measurement cycles. The  $0.005 mA$  difference can change  $V_M$  by  $3 nV$  if  $R_M$  does not change. Fig: 4.10(b) and Fig: 4.10(d) show that the  $V_M$  increased by  $18 nV$  in the first 75 cycles which indicates that not only the current but also the sample resistivity changed during the measurement cycles, which caused the drift of  $V_M$ . In Fig: 4.10(e),  $T_s$  increased from  $23.06 ^\circ C$  to  $23.16 ^\circ C$  in the first 75 cycles and then drifted to  $23.17 ^\circ C$  after the 100th cycle. The  $\rho - T$  relation of the sample corresponds to the increase of  $V_M$  by  $136.2 nV/^\circ C$ . The change of  $T_s$  between each two adjacent measurement cycle was  $0.001 \pm 0.012 ^\circ C$ . It corresponds to  $(0.14 \pm 0.9) nV$  of  $V_H$  uncertainty. The voltage noise caused by this temperature drift may explain the uncertainty of  $V_H$ , which is  $V_H = (385.8 \pm 0.3) nV$  in Fig: 4.10(c). As a result, the average and standard error of  $R_H$  shown in Fig: 4.10(f) is  $R_H = (7.996 \pm 0.001) 10^{-8} V.m/AT$ .

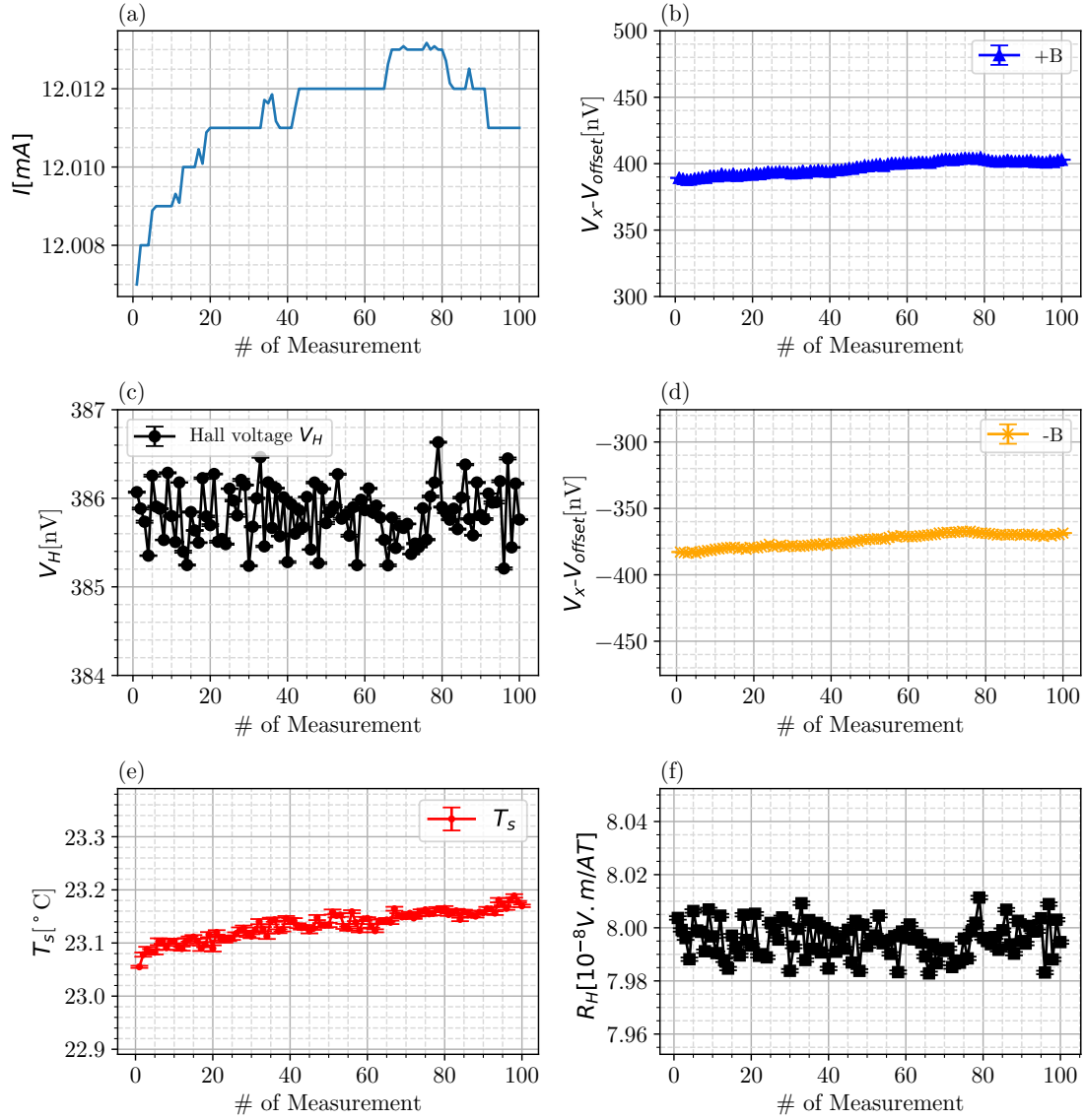
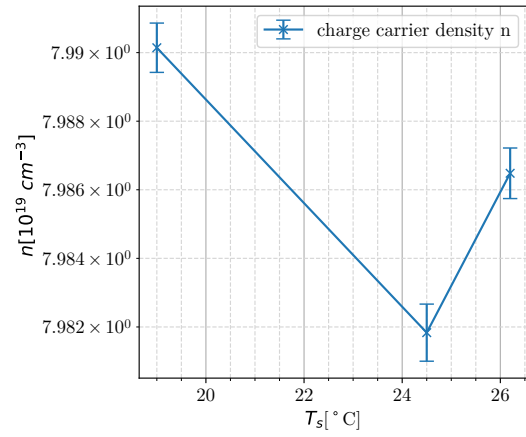
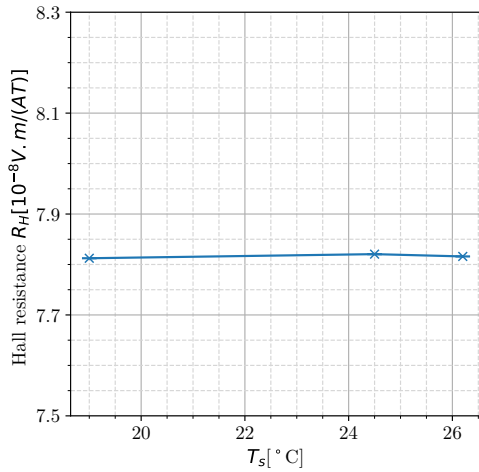
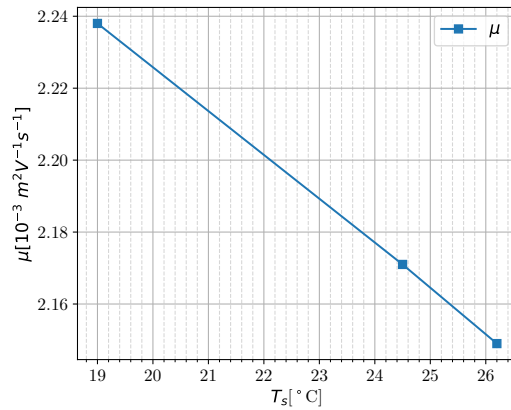
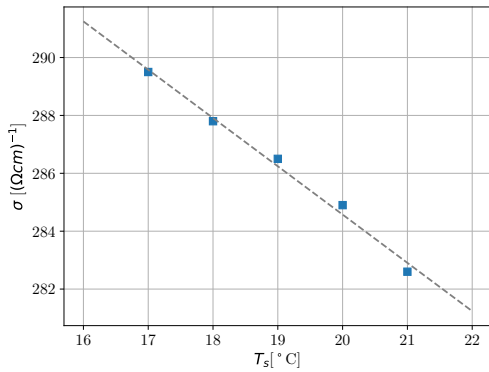


Figure 4.10: Voltage measured in the AC Hall measurement of sample Ks with the transformer,  $T=23\text{ }^{\circ}\text{C}$  under the PI temperature control. There were 100 measurement cycles; it took 70 seconds to run each cycle. (a) is the current, (b) and (d) are the voltage  $V_x - V_{\text{offset}}$  when the magnetic fields were +B and -B; (c) is the calculated Hall voltage  $V_H$ ; (e) is  $T_s$ ; (f) is  $R_H = (7.996 \pm 0.001) \cdot 10^{-8} \text{V.m/AT}$ .

$n$  and  $\mu$  of the sample are measured at different temperatures, shown in Fig: 4.11. In the  $8^\circ\text{C}$  room temperature range, the  $n$  does not show temperature dependence and,  $\mu$  shows linear dependence with  $T_s$ . It indicates that the sample is a heavily doped semiconductor.



(a) Temperature dependence of Hall resistance,  $R_H$  (b) Temperature dependence of charge carrier density,  $n$



(c) Temperature dependence of electrical conductivity,  $\sigma$  (d) Temperature dependence of charge carrier mobility,  $\mu$

Figure 4.11: Temperature dependence of  $R_H$ ,  $n$ ,  $\sigma$ , and  $\mu$  in the room temperature range.  $R_H$  and  $n$  are temperature independent;  $\sigma$  and  $\mu$  change linearly along with temperature.

Fig: 4.12 shows the voltage signal without temperature control. The glitches caused by the magnetic EMF were cleaned up by programming. The misalignment voltage drifted quickly along with the temperature, which was  $(0.005 \pm 0.011) \text{ }^\circ\text{C}$ . From the 100 measurement cycles, the Hall voltage  $V_H = (398.4 \pm 0.7) \text{ nV}$ . The noise level was still low compared with the measurement with temperature control. However, the heat generated by the magnet did not dramatically change the temperature until the 40th cycle. More details are shown in Fig: 4.13. In Fig: 4.13(e),  $T_s$  drifted from  $20.03 \text{ }^\circ\text{C}$  to  $20.06 \text{ }^\circ\text{C}$  in the first 40 cycles (1 minute per cycle); it drifted from  $20.06 \text{ }^\circ\text{C}$  to  $20.5 \text{ }^\circ\text{C}$  in the rest 60 cycles. The reason  $T_s$  changed relatively slowly in the first 40 cycles than later can be explained: the sample holder box needs time to be heated up by the magnet. If the Hall measurement was continued after the 100th cycle without PI temperature control, the  $T_s$  would increase as the rate of  $1 \text{ }^\circ\text{C}$  per hour. In Fig: 4.13(c)  $V_H = (398.5 \pm 0.5) \text{ nV}$  in the first 40 cycles, and  $V_H = (398.4 \pm 0.8) \text{ nV}$  in the rest 60 cycles. It shows that the measurement uncertainty of  $V_H$  increases when  $T_s$  drifts faster.

In the AC Hall measurement with the transformer, the most significant noise source was  $V_M$  related to the temperature drift. By using the PI temperature control, the noise level was lowered by 60%. If there was a temperature control, and the electrical conductivity of the sample stayed constant during the measurement, the dominant noise would be the voltage noise produced by the noise in the excitation current and the sample-lead contact resistance. Stabilizing  $V_M$  is also important when measuring the Hall voltage by the lock-in amplifier. A proper dynamic range of the lock-in amplifier is required. For example, if it was known that  $V_H$  was around  $400 \text{ nV}$ , a proper reading range would be  $\pm 500 \text{ nV}$ . Large  $V_M$  drift may cause the “overload” reading of the lock-in amplifier; this drift can be reduced by the PI temperature control. It is good to point out that the PI control function slightly lowers the speed of the LabVIEW program. If the goal is to qualitatively measure the  $R_H$  at room temperature, the measurement without the PI control may still satisfy the requirement. However, since  $n$  and  $\mu$  of thermoelectric samples at different temperatures, up to  $T = 1000 \text{ K}$ , are important information, good temperature control is required. In conclusion, the PI temperature control benefits the AC Hall measurement with the transformer.

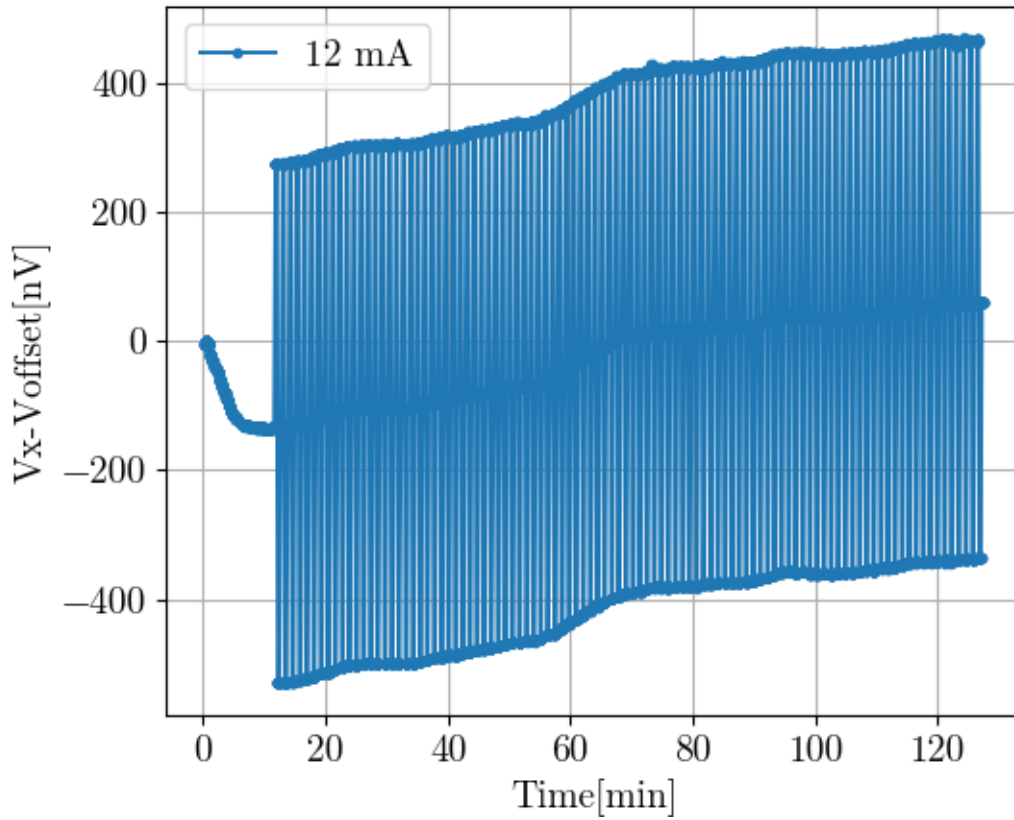


Figure 4.12: The voltage data of the AC Hall measurement with the transformer but without temperature control. The voltage shown in the figure is after taking the transformer  $\times 100$  gain into account. The voltage drifted about  $+200 \text{ nV}$  in 120 minutes.  $V_{\text{offset}} = +10.84 \mu\text{V}$ .

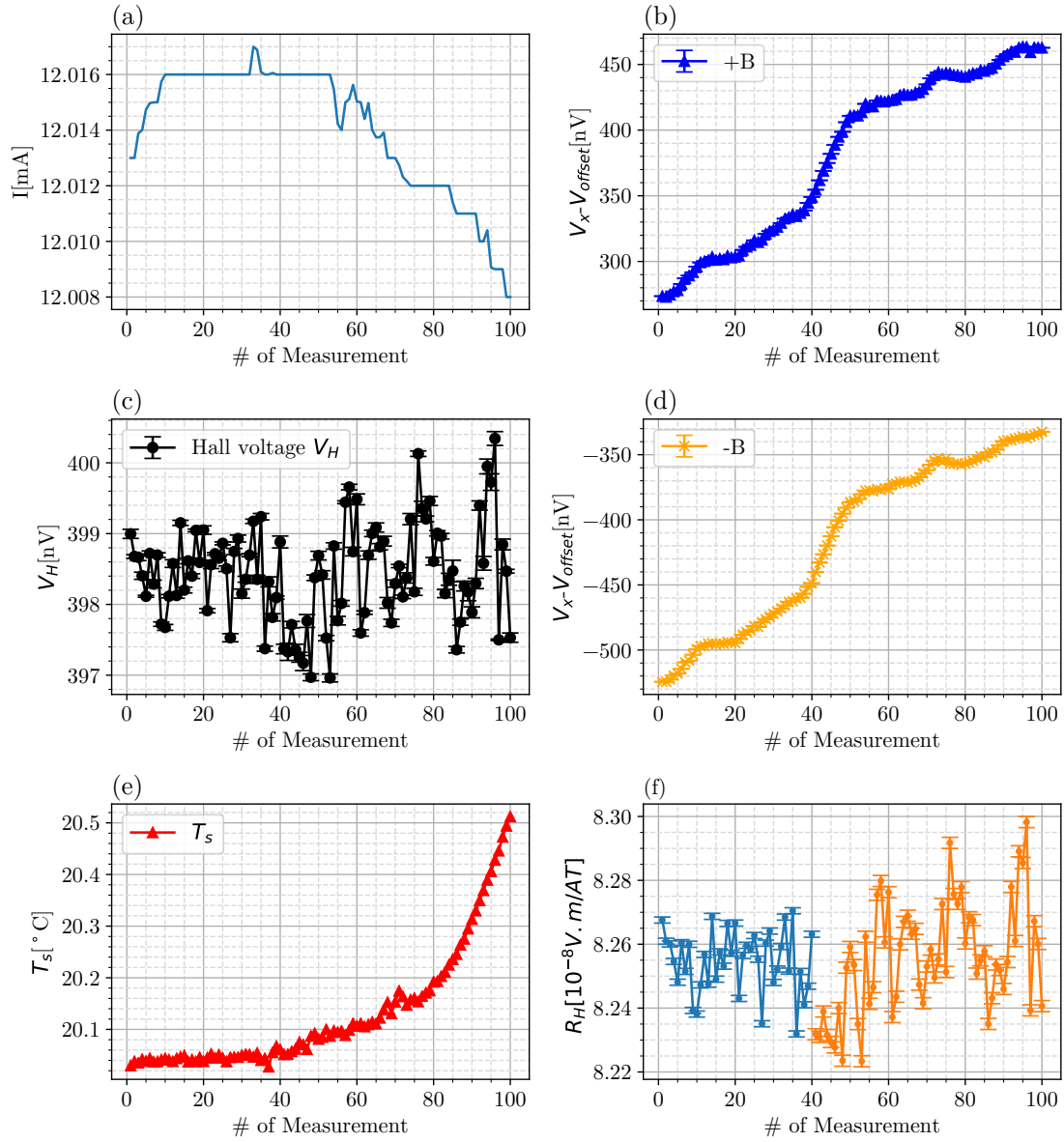


Figure 4.13: Details of the AC Hall measurement without temperature control. (a) is the excitation current. (b) and (d) are the voltage data when magnetic fields were  $+B$  and  $-B$ . (c) is the calculated Hall voltage. (e) is the temperature,  $T_s$ , during the test; it kept below  $20.5 \text{ }^\circ\text{C}$  in the first 40 measurement cycles and rose quickly to  $20.5 \text{ }^\circ\text{C}$  due to the heat from the magnet. (f)  $R_H = (8.25 \pm 0.001) \times 10^{-8} \text{V.m/AT}$  in the first 40 measurement cycles, and  $R_H = (8.25 \pm 0.002) \times 10^{-8} \text{V.m/AT}$  in the rest 60 measurement cycles. The temperature drift increased the uncertainty of  $R_H$ .

### 4.3.2 AC Hall measurement without the transformer

The Hall measurement can still take the benefits of the AC current and the lock-in amplifier without using the transformer. Furthermore, 10 MΩ input impedance is much better than that of the transformer. However, there is 88 dB CMRR between the input A and the input B, which causes voltage offset.

Fig: 4.14 is the voltage of the AC Hall measurement without the transformer. The magnetic EMF glitches were cleaned by programming.  $V_{\text{offset}} = -7.658 \mu\text{V}$  with  $I = 12 \text{ mA}$  and  $T$  was controlled to  $23 \text{ }^\circ\text{C}$ . The measurement results are:  $V_{\text{H}} = (413.9 \pm 6.6) \text{ nV}$  and  $R_{\text{H}} = (8.591 \pm 0.014) \times 10^{-8} \text{ V.m/AT}$ . The input noise of the lock-in amplifier caused  $\pm 5.7 \text{ nV}$  RMS noise after averaging 40 points, which was close to the uncertainty of  $V_{\text{H}}$ . From the Fig: 4.15, the common mode voltage drift also caused noise which was counted as  $V_{\text{H}}$ .

In Fig: 4.15(b) and Fig: 4.15(d), the voltage drift followed 0.01 V/A which was much higher than the misalignment resistance. The sample was under temperature control, and its electrical resistivity was stabilized. The excitation current in Fig: 4.15(a) showed the same drift trend. Therefore, one explanation is that the drifting voltage was caused by the common mode voltage of the lock-in amplifier. The voltage at the sense leads,  $V_{\text{A}}$ , is not zero because of the sample-lead contact resistance. Then the CMRR offset voltage,  $V_{\text{CMRR}}$ , can be written as:

$$V_{\text{CMRR}} = 4 \times 10^{-5} I R_{\text{contact}} \quad (4.2)$$

and:

$$I = \frac{V_{\text{OL}}}{R_{\text{load}} + 2R_{\text{contact}}} \quad (4.3)$$

where  $V_{\text{OL}}$  is the output voltage from the lock-in amplifier which is relatively constant;  $R_{\text{load}}$  is the total current limiting resistance which was  $260 \Omega$  in this measurement,  $R_{\text{contact}}$  is the contact resistance at one joint between the sample and the current lead. At the beginning this measurement,  $R_{\text{contact}} = 11 \Omega$ , so  $V_{\text{A}} = 0.132 \text{ V}$  when  $I = 12 \text{ mA}$ . With CMRR=88 dB, the offset voltage  $V_{\text{CMRR}} = 5.26 \mu\text{V}$ . The 0.01 mA or 0.083 % current change in Fig: 4.15(a) corresponds to  $0.12 \Omega$   $R_{\text{contact}}$  change, which is reasonable for a mechanical joint connection by the pogo pins.

In conclusion, in the AC Hall measurement without the transformer, the dominant noise sources are the CMRR offset voltage of the SR830 lock-in amplifier and  $V_{\text{M}}$ .

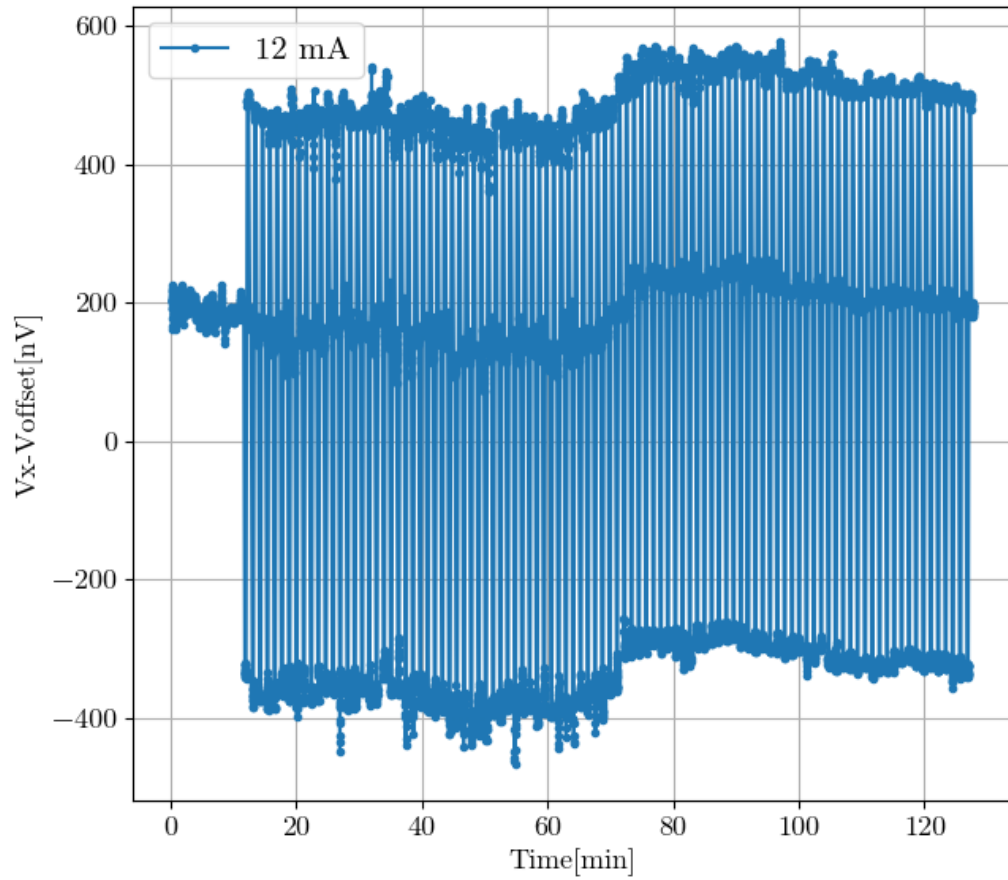


Figure 4.14: Voltage in the AC Hall measurement without the transformer.  $T = 23.0^{\circ}C$  by the PI temperature control.  $V_{\text{offset}} = -7.858 \mu V$ . In this figure, the voltage noise is more significant than that in Fig: 4.9.

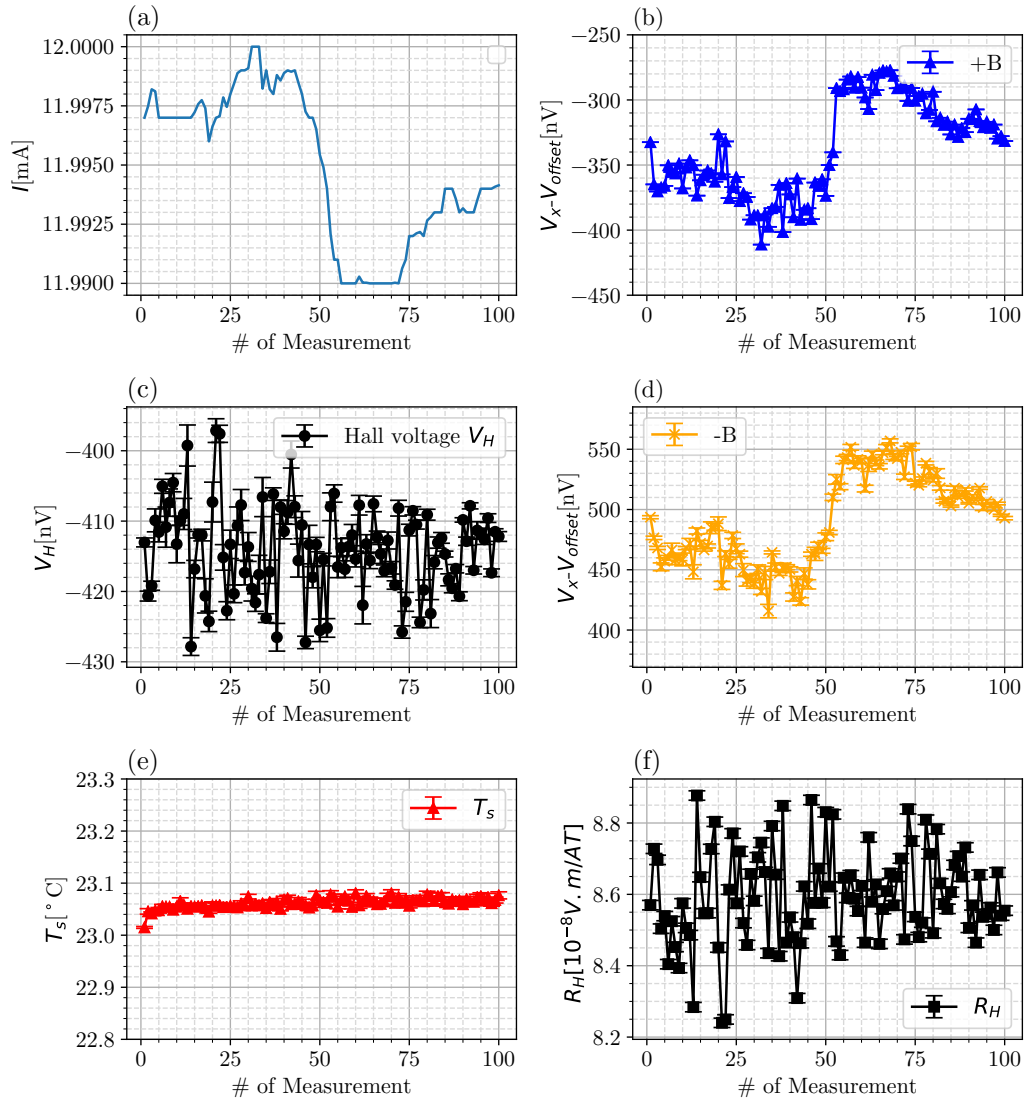


Figure 4.15: The AC Hall measurement without the transformer. (a) is the excitation current. (b) and (d) are the voltage data when the magnetic fields were  $+B$  and  $-B$ . (c) is the calculated Hall voltage. (e) is the temperature  $T_s$  under temperature control during the test. (f)  $R_H = (8.59 \pm 0.014) \times 10^{-8} \text{V} \cdot \text{m/AT}$

## 4.4 Discussions

### 4.4.1 Comparison of the three Hall measurement methods

In this thesis, three methods are introduced: the DC Hall measurement, the AC Hall measurement with the transformer, and the AC Hall measurement without the transformer.

From the experimental results, the most accurate way to measure the  $R_H$  of sample Ks is to use the AC Hall measurement with the transformer. The intrinsic noise of the voltmeter is one of the main noise sources. The transformer amplifies the signal from the sample by a factor of 100 while the noise from the voltmeter is kept at the same level. Therefore, the signal-to-noise ratio in the AC Hall measurement with the transformer is higher than that without the transformer.

The limitation of using the transformer is that it has a relatively low input impedance. It has a maximum input impedance of about  $600 \Omega$  at a frequency of  $15 \text{ Hz}$ , which means that the loading resistance at its input should not be over  $50 \Omega$ .<sup>[3]</sup> Therefore, the transformer method is not ideal for samples with high electrical resistivity.

Compared to the method with the transformer, the AC Hall measurement without the transformer has a high input impedance, but it is limited by its poor signal-to-noise ratio and lower CMRR.

By measuring the temperature dependence of the sample electrical resistivity, it is clear that  $V_M$  drifted along with temperature during the Hall measurement and caused significant noise. One way to slow the drift is to use the PI temperature control properly.

In the DC Hall measurement, the temperature control was disturbed by the noise through the GPIB cables. After fixing the GPIB problem, the comparison between the measurement with or without the PI control shows that the thermal EMF was one of the dominant sources of voltage noise.  $V_M$  can be stabilized by the temperature control; it drifted without temperature control but its noise contribution was overwhelmed by the noise from  $V_T$  which was more significant. Note that the heat from the electromagnet changed the thermal EMF through the electrical leads connecting to the sample and the nano-voltmeter. The PI temperature control can only stabilize the sample temperature  $T_s$  but not the temperature in the shielded room. The drift in  $V_T$  was not seen to be reduced with temperature control, so it must be caused by the various contacts in the leads running to the voltmeter. The uncertainty of  $V_H$  with temperature control was the same as that without temperature control.

In the AC Hall measurement, the noise due to  $V_T$  becomes insignificant, and  $V_M$  becomes a significant noise source. The PI temperature control can stabilize the sample temperature

and its electrical conductivity against the heat from the electromagnet. Compared with the measurement without the PI temperature control, the measurement with temperature control has slower  $V_M$  drift and lower uncertainty of  $V_H$ . The low noise measurement provides the chance to study the temperature dependence of the charge carrier density  $n$  and the mobility  $\mu$ .

#### 4.4.2 Normalized Hall resistance $R_H$

$R_H$  was normalized to be  $\Delta R_H/R_H$  to compare the measurement uncertainties of the different methods, where  $\Delta R_H$  is the standard error of 100 measurement data points. The result is shown in the Figure: 4.16. The dash lines in the figure are the theoretical limit from the electronics.

The AC Hall measurement with the transformer has the lowest experimental measurement uncertainty; it also has the lowest thermal noise because of the large signal-to-noise ratio. The temperature control was found to improve the measurement uncertainty by 30%.

The DC Hall measurement has eight times higher uncertainty than the AC Hall measurement with the transformer. Its experimentally determined noise was much higher than the theoretical limit, which may have been caused by the drifting thermal EMF. The uncertainties of the measurement with and without temperature control are almost the same, which indicates that the thermal EMF outside the sample holder box may be the dominant noise source.

The AC measurement without temperature control had the highest measurement uncertainty even with temperature control. Firstly, it had the highest noise, most of which came from the input noise of the lock-in amplifier. Secondly, there was a noticeable common mode voltage offset when using the method, which also increases the uncertainty while measuring the Hall voltage.

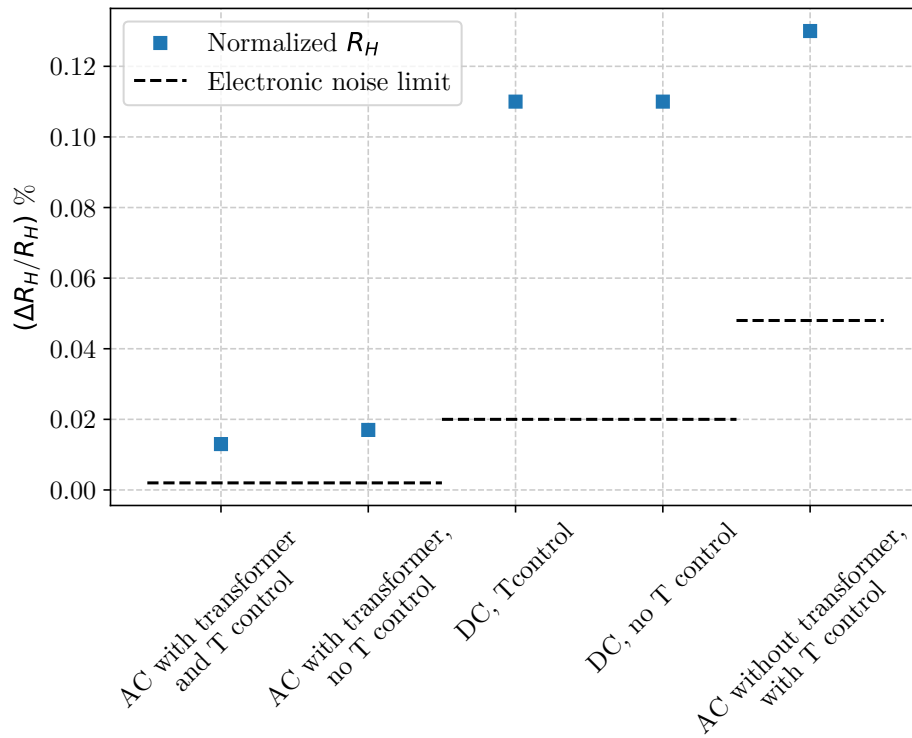


Figure 4.16:  $(\Delta R_H/R_H)$  % of different measurements. The dash lines are the theoretical limit of the methods only considering the electronic noise from the electronics.

### 4.4.3 Measurement speed

The DC Hall measurement had low measurement speed compared with the AC Hall measurement, shown in Fig: 2.9. The DC Hall measurement needed at least five steps in each measurement cycle, changing  $I$  or  $B$ , in order to collect enough voltage data to cancel out  $V_T$  and  $V_M$ . The AC Hall measurement, because of the AC current, only needed three steps, where only  $B$  was changed. If measuring 100 data points of  $R_H$  for low measurement uncertainty, the DC Hall measurement needed about seven more hours than the AC Hall measurement.

Another concern with the setups is that the heat dissipation of the electromagnet in the Hall measurement setup was significant. After continuously providing a 0.5  $T$  magnetic field for four hours, the magnet and surroundings would need about one day to cool back to room temperature. Therefore, more  $R_H$  data points can be taken in a single day with higher measurement speed.

In conclusion, considering the measurement speed, the AC Hall measurement with the transformer is recommended.

## 4.5 Summary

The DC Hall measurement is a simple method to measure the Hall resistance and the charge carrier density. It requires a low noise DC voltmeter to read small Hall voltage signals. The most important noise source is the drifting thermal EMF caused by the temperature drift. Furthermore, the directions of both the current and the magnetic field need be switched in the measurement, which causes low measurement speed. The standard derivation of the best measurement method can be 1.0%, which is good enough to qualitatively characterize the charge carrier densities of various samples.

The AC Hall measurement with the transformer has the highest signal to noise ratio. It can also eliminate the thermal EMF problem and common mode problem. The measurement uncertainty is sensitive to the misalignment voltage and the electrical resistivity of the sample, which requires good temperature control. The 600  $\Omega$  input impedance of the transformer limits the measurement to low electrical resistivity samples with low lead resistance and low contact resistance.

The AC Hall measurement without the transformer is capable of measuring samples with high  $\rho$  because of the high input impedance of the lock-in amplifier. The offset voltage caused by the common mode is the most important noise source in the measurement.

The PI temperature control can stabilize the sample holder box temperature and the samples' electrical conductivity, especially when the magnet heats up. Comparing the results with temperature control and without temperature control, the temperature control slightly improved the measurement uncertainty.

## 4.6 Conclusions

The three methods: the DC Hall measurement, the AC Hall measurement with the transformer, and the AC Hall measurement without the transformer are good to measure the Hall resistance of bulky thermoelectric samples at room temperature. If not considering the systematic error caused by the accuracy of the sample geometry, the uncertainties of the three methods were below 1%.

The DC Hall measurement is based on the working principle of Hall effects and has a simpler setup structure; however, it is slower than the AC Hall measurement. The thermal EMF is its main noise source.

The AC Hall measurement with the transformer is the best way to measure thermoelectric samples with low electrical resistivity. The benefits of using this method rather than the DC method are the lower measurement uncertainty and higher measurement speed. The thermal EMF problem, which bothered the DC method, was not seen in the AC Hall measurement.

The AC Hall measurement without the transformer is the most inaccurate method of the three methods because of the common mode voltage offset and the low signal-to noise ratio.

The PI temperature control may improve the measurement accuracy by stabilizing sample temperature and misalignment voltage  $V_M$ . It only slightly improved the AC Hall measurement but not in the DC Hall measurement because of the drifting thermal EMF.

## 4.7 Future work

The Hall measurement techniques discussed in this thesis are good but not perfect. Future work can be focused on improving the measurement accuracy and applying a larger temperature range during the measurement. Some improvements may be reached in the short term, while some are time-consuming. The first thing that can be completed in a

relatively short time is to develop a better temperature control system, such as adding a cooling system on the electromagnet and adjusting the effective temperature range of the PI temperature control. Second, the connection leads can to be altered to reduce the number of joints within dissimilar materials, which can lower the thermocouple effect in the DC Hall measurement.

More effort can be placed to develop the setup which will be capable of doing the Hall measurement at high temperatures. Problems will arise at high temperatures, such as the polystyrene sample holder blocks may melt.; the samples, which are often toxic, may have significant vapour pressure and become too hazardous to measure in this open configuration. These challenges is more likely to require redesigning a new measurement setup rather than simply tweaking the existing one. However, as many other high-temperature Hall measurement setups have already been designed, the work is feasible.

## Part II

# Subgap Leakage measurement of Josephson Junctions

# Chapter 5

## Introduction

### 5.1 Introduction of Josephson junctions and subgap leakage measurement

Josephson junctions are nonlinear electronic elements and operated at low temperature. One type of Josephson junctions is superconductor-insulator-superconductor(SIS), using niobium for its superconducting layers and oxidized aluminum for its insulator layer. Niobium is used for its relatively high superconducting transition temperature ( $T_c = 9.3 K$ ), and aluminium oxide is used for its ease of deposition. It has promising potential for various of applications, such as quantum computing and photon detectors.[16][29]

The subgap leakage measurement is a method that characterizes the quasiparticle conductance in Josephson junctions at low temperature.[31] When there is a small voltage bias across the junction, Cooper pairs break and turn into quasiparticles which penetrate through the insulator barrier.

A small current can be measured when applying non-zero bias voltage  $V < 2\Delta$  to the junction, where  $\Delta$  is the superconducting gap of the electrode. The current-voltage data points can be plotted in the same graph, which is the I-V curve of the junction. The lowest current value in the curve is usually seen as the smallest subgap current  $I_{sg}$ , and the resistance corresponding to  $I_{sg}$  is the subgap resistance  $R_{sg}$ . The BCS theory predicts that the  $R_{sg}$  is highly related to the temperature. When the junction approaches zero-temperature, the number of the quasiparticles generated by thermal excitation drops dramatically, and  $I_{sg}$  should be around zero, where  $R_{sg}$  is infinite large. An approximate

formula of  $I_{\text{sg}}$  is[45]

$$I_{\text{sg}} = \frac{2G_n}{e} e^{-\frac{\Delta}{k_B T}} \sqrt{\frac{2\Delta}{eV + 2\Delta}} (eV + \Delta) K_0\left(\frac{eV}{2k_B T}\right) \quad (5.1)$$

where  $\Delta$  is the superconducting gap of electrodes, and  $T$  is the temperature with  $T \ll \frac{\Delta}{k_B}$ . However,  $I_{\text{sg}}$  is often detected at low temperature, which is not expected. The experiment of determining the  $I_{\text{sg}}$  is called subgap leakage measurement.

## 5.2 Subgap leakage current

Subgap leakage current is caused by Andreev reflections, multiparticle tunneling, material defects, and pinholes.[13] A recent observation by using TEM and ATM clearly showed surface roughness between layers, diffusive spots, and pinholes.[17] The subgap leakage current decreased after the layer surface structure was improved. However, by comparing the subgap resistance of different junctions, another paper proved that pinholes may not be a dominant source of the subgap leakage in SIS tunnel junctions with high resistance.[13] Although the junction layers could be directly observed, there might be defects that are caused by some ultra-fine particles, which is hard to observe.[17] For example, some particles may be located between the layers of the junction and cause the rough surface. The critical current,  $I_c$ , and subgap leakage current could be affected by those particles, which could be clearly detected in the subgap leakage measurement. Therefore, the I-V characteristics of the junctions at different positions under the same wafer can provide information to improve the fabrication processes.

In quantum computing, Josephson junctions are the essential element of qubits which have well-determined  $|0\rangle$  and  $|1\rangle$  states. They are required to have long coherence time,  $T_1$ , in order to function the qubits.[7] However, subgap leakage can limit  $T_1$ . A study showed that the quasiparticles which tunnel through the junctions could cause decoherence by several mechanisms.[24] For example, it may generate noises with certain frequencies, which causes the transition between states. It is also the source of energy dissipation. The electrical circuit connections to the qubits may also be the reason of decoherence, which may cause  $I_{\text{sg}}$  to be temperature-independent at low temperature.[31][30] The quantum quality factor,  $Q$ , is also related to the subgap leakage, which requires the junctions to have more than 1  $G\Omega$  resistance when  $Q \geq 10^6$ . [34]

## 5.3 I-V curves of Josephson junctions

The research in this thesis used Josephson junctions from D-wave Inc. The junctions were unshunted  $Nb/AlOx/Nb$  tunnel junctions. The  $I_{sg}$  values of the junctions were measured by characterizing their I-V curves. There are two types of methods: current bias and voltage bias.

The current bias method has a DC current applied to the junction while voltage is measured. The voltage bias method has a DC bias voltage applied and the current through the junction is measured. The two methods show very different I-V curves for the same junction.

### 5.3.1 Current bias

The promising applications of Josephson junctions come from their non-linear current-voltage relationship below the critical temperature of the junctions. Fig: 5.1 shows the theoretical I-V curves of Josephson junctions at low temperature with current bias.[\[44\]](#)

When increasing the bias current from zero, the junction stays superconducting with zero voltage. When the current exceeds  $I_c$ , the junction turns non-superconducting and the voltage quickly approaches the gap voltage  $V_g = 2\Delta/e$ ; if the current increases further, the junction turns to the normal region and behaves like a normal resistor with its normal resistance,  $R_n$ . Then decreasing the bias current from  $I > I_c$ , the junction voltage stays at  $V_g = 2\Delta/e$  until  $I$  reaches a return current,  $I_r$ . A similar characteristic occurs for negative applied currents. The direction of the voltage change during the scan is indicated by the arrows in Fig: 5.1.

The region where  $0 < V < 2\Delta/e$  is considered to be the subgap region. With this method, the subgap leakage current cannot be clearly identified.

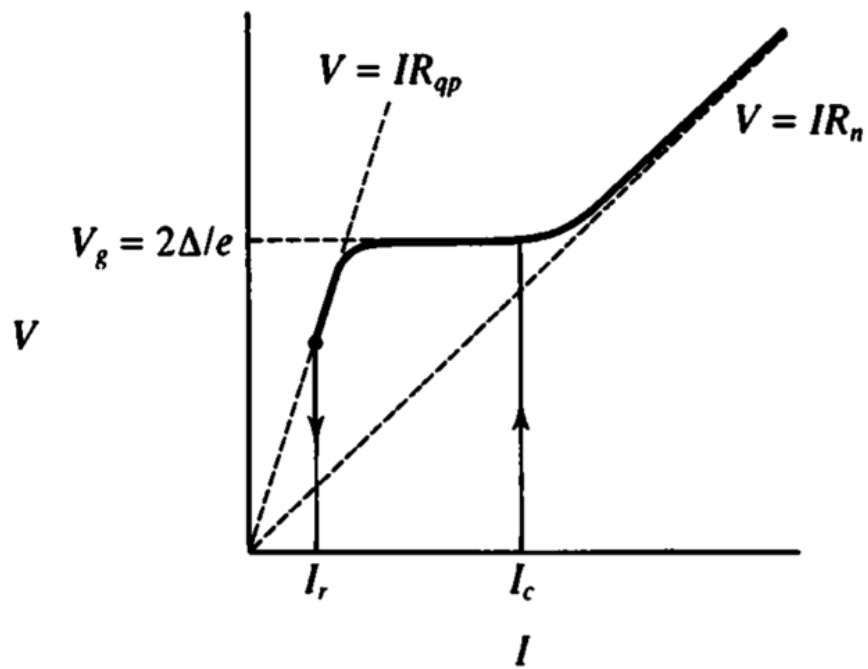


Figure 5.1: Hysteresis I-V curve of unshunted Josephson junctions.[44] The errors indicate how junction voltage  $V$  change along with bias current  $I$ .

### 5.3.2 Voltage bias

Unlike current bias, the voltage bias method measures the junction current while applying DC voltage to the junction. The I-V curve of an unshunted Josephson junction from the voltage bias method is usually non-hysteretic, which shows more details of the subgap region than the current bias method.

For a  $Nb/AlOx/Nb$  junction, although there are different methods and standards, one general characterization of the subgap leakage is to measure the current  $I_{sg}$  with bias voltage  $V_{t\text{extbias}}=0.5$  mV:

$$R_{sg} = \frac{V_{t\text{extbias}}}{I_{sg}} \quad (5.2)$$

For a junction to be suitable for quantum computing applications,  $R_{sg}$  is expected to be larger than  $1$   $G\Omega$ . Previous research has focused on the subgap leakage characterization of Josephson junctions.[31][14] As shown in Fig: 5.2, there are some peaks and valleys below  $1.0$  mV, which poses an unsolved puzzle. One possible reason may be the existence of a resonance frequency, even through the bias is a DC voltage.[12]

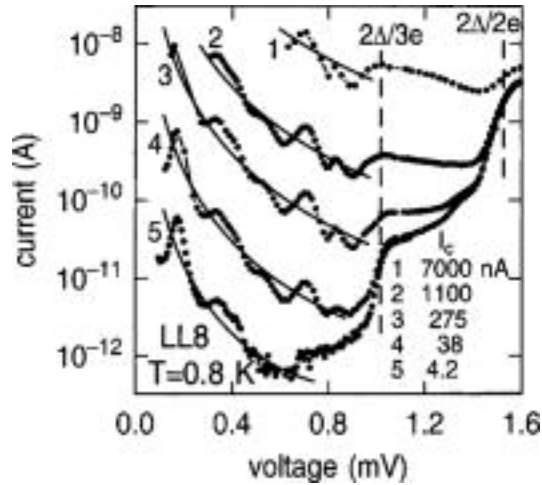


Figure 5.2: subgap leakage curve of a Nb Josephson junction at  $T = 0.8$  K. Its critical current  $I_c$  is changed by applied magnetic field. [31]

The  $I_c$  and  $R_n$  of the junctions are different because of the difference in sizes, materials, and layered structure. A method to compare different junctions is to plot  $R_n I - V$  curves or  $eR_n I/\Delta - eV/\Delta$  curves. Based on the equation derived by Ambegaokar and Baratoff,

the junctions with same superconducting electrodes have the same  $I_c R_n$ :[\[2\]](#)

$$I_c R_n = \frac{\pi \Delta}{2e} \tanh\left(\frac{\Delta}{2k_B T}\right) \quad (5.3)$$

Figure: [5.3](#) and Figure: [5.4](#) show the comparison using normalized I-V curves of different Nb Josephson junctions.[\[23\]](#) The calculation from Ohm's law is shown as the straight line (c) in both figures. Figure [5.3](#) shows that junction (a) and junction (b) have different  $J_c$  and I-V characterization in the subgap region where  $0 < V < 2.5 \text{ mV}$ . The significant current change near  $V = 2.7 \text{ mV}$  corresponds to the superconducting gap of Nb. When  $V > 3.0 \text{ mV}$ , curve (a) and curve (b) turn to straight lines, which shows that both junctions behave as normal ohmic resistors. Figure: [5.4](#) shows the comparison between an ideal Josephson junction, shown as curve (a), and a junction with pinholes, shown as (b). Because the pinholes short the two electrodes, the junction with pinholes does not show the Josephson effect in the curve (b). In conclusion, the normalized I-V curves can clearly compare the quality of different junctions.

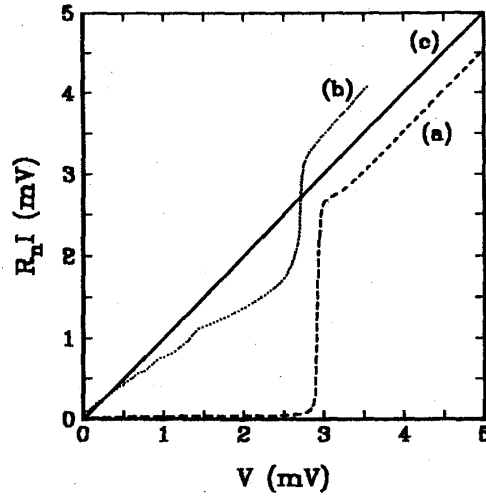


Figure 5.3: Typical 4.2 K I-V curves for (a) low critical current density  $J_c$ , (b) high  $J_c$  junctions and (c) Ohm's law prediction.[\[23\]](#)

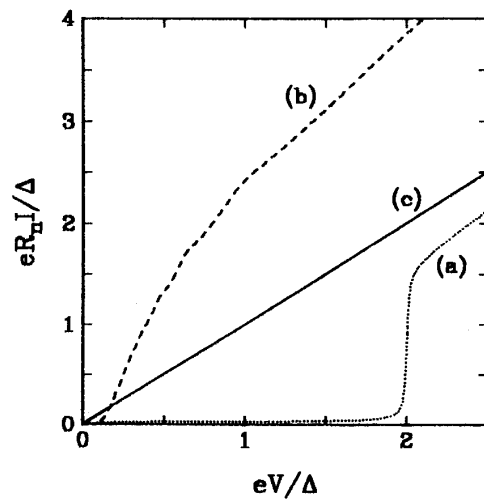


Figure 5.4: Theoretical I-V characteristics used to describe the junctions: (a)an ideal tunnel junction; (b)a junction with pinholes; (c) Ohm's law.[23]

### 5.3.3 Magnetic suppression

As shown in Fig: 5.2, the supercurrent can be suppressed by the outer magnetic field. For a junction with rectangle geometry, the magnetic field should be perpendicular to the direction of the supercurrent. If the thickness of the insulation layer is  $d$ , the field penetration depth is  $\lambda$ , then the magnetic flux  $\Phi$  is

$$\Phi = (d + 2\lambda)LB \quad (5.4)$$

where  $L$  is the width of the junction, and  $B$  is the applied magnetic field.

The maximum supercurrent under  $\Phi$ ,  $I_m(\Phi)$ , follows the eq. 5.5 and shown in Fig: 5.5:[44]

$$I_m(H)/I_m(0) = |\sin(\pi\Phi/\Phi_0)/(\pi\Phi/\Phi_0)| \quad (5.5)$$

where  $\phi_0 = 2.07 \text{ mT} \bullet \mu\text{m}^2$ . By changing the magnetic flux to certain values, the supercurrent can be suppressed to be nearly zero, which helps to observe  $I_{sg}$ .

Furthermore, the supercurrent-flux curve is highly related to the current density distribution of the junctions.[5] It provides the feedback information of pinholes or imperfect edges of the Josephson junctions.

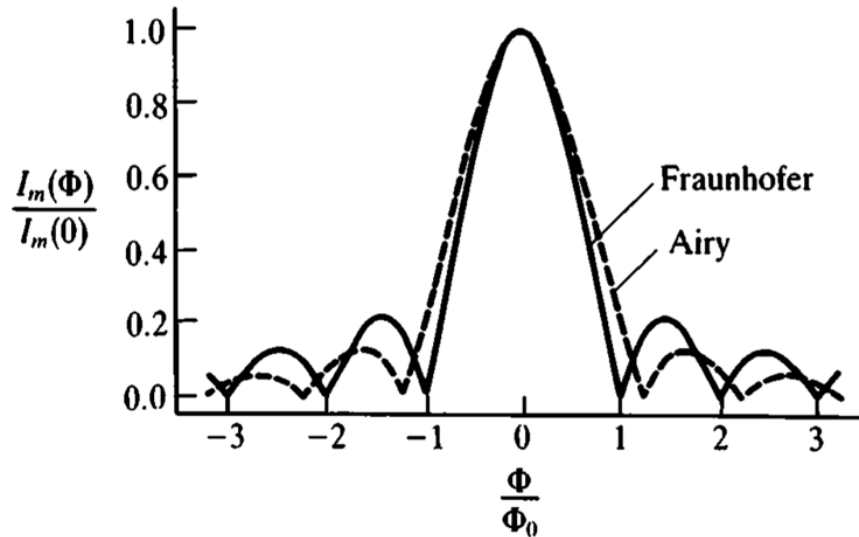


Figure 5.5: Maximum supercurrent of Josephson junctions suppressed by magnetic flux.[44]

## 5.4 Temperature dependence

Described as Eq. 5.1, the smallest subgap leakage current  $I_{min}$  of the junction LL8 shows strong temperature dependence at low temperature, shown in Fig: 5.6.[31] Two different magnetic field values are applied which causes the two  $I_c$ . The relationship between  $\ln I_{min}$  and  $T^{-1}$  is linear above  $T = 1 K$  as the prediction of the BCS theory; when below  $T = 1 K$ ,  $I_{min} - T^{-1}$  curve becomes flat and  $I_{min}$  approaches a constant when  $T$  decreases. What causes the flat curves is of the utmost interest. This could be due to mechanical defects, pinholes, or external noise. By characterizing this residual leakage current, process conditions can be altered to make better junctions or better circuit configurations with lower leakage.

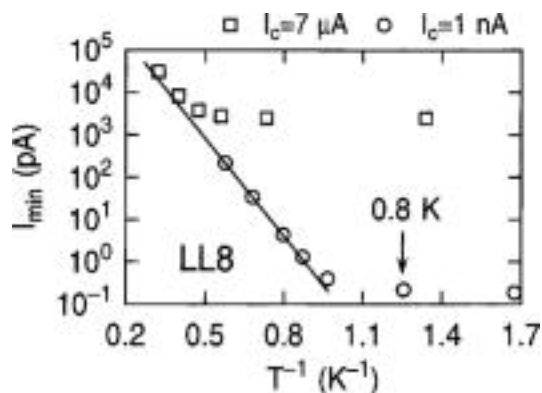


Figure 5.6: Subgap leakage current temperature dependence in the experiment. [31] The curves are linear above  $T = 1 K$  which follows the BCS theory prediction; they are flattened when  $T < 1 K$ .

## 5.5 Motivation and challenges

The research about the subgap leakage measurement in this thesis is part of the collaboration among Jan Kycia's group at the University of Waterloo, JPL and D-wave Inc.. The goal is to test the quality of Josephson junctions manufactured by different techniques. For this thesis, the motivation is to put together a experimental system that can accurately characterize the I-V curves and subgap leakage current of different Josephson junctions at low temperature. Therefore, this part is to introduce the technique of characterizing the Josephson junctions at low temperature. The sample preparation steps will be introduced

first and then the measurement setup, which includes an adiabatic demagnetization refrigerator (ADR) and a superconducting magnet. After that, the experiment results from different sample junctions will be described.

There are some challenges related to the subgap leakage measurement. Some of these are associated with the low-level subgap leakage current which can be as low as  $1\text{ pA}$ . The interesting signal from the sample may be buried in the electrical noise through the circuit; therefore, the noise sources of the measurement should be analyzed and reduced. A sensitive and low noise current amplifier is necessary as well. Furthermore, some challenges are related to the environment temperature of the sample. The lowest temperatures the ADR can reach is  $130\text{ mK}$ , which is sufficient to enter the interesting flat region of the subgap leakage measurement. It was found that the system has a poorly defined region in the temperature range,  $1.2 \sim 1.4\text{ K}$ . This has been attributed to the superconducting transition of aluminium support parts near the sample. Last but not least, the samples are fragile to high currents and static. It was challenging to protect the sample from being overloaded during the sample preparation period and the measurement period.

# Chapter 6

## Subgap leakage measurement setup

### 6.1 Sample preparation

The samples are chips containing multiple Josephson junctions, manufactured and sent to our group from D-wave Inc. The junction chip is glued to a copper chip holder by GE varnish and electrically connected by wire bonds. The chip holder is mounted to a copper sample holder with copper shield, shown in Fig: 6.1.

Each junction has four wire bonding electrodes. The current bias method needs to wire all four electrodes of the junction; the voltage bias method only needs two. The sample holder is capable of wiring two to four junctions at the same time.

The sample holder is mounted to the base temperature stage of an adiabatic demagnetization refrigerator (ADR) for low-temperature measurements. The model name of the ADR is High Precision Devices SHASTA 106 adiabatic demagnetization refrigerator. It is designed to lower the temperature of small samples from several Kelvins to down to 50  $mK$  by reducing the spin entropy of paramagnetic salt crystals inside the ADR.[35]

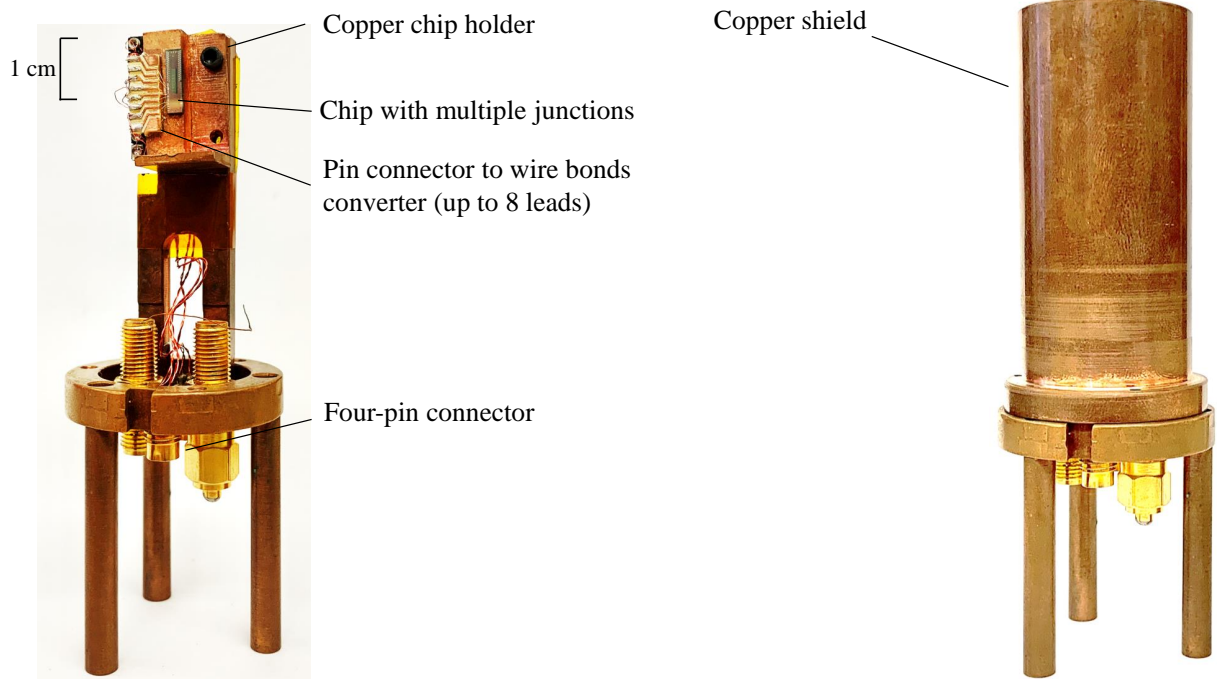


Figure 6.1: The copper sample holder, without(left) and with(right) the copper shield, for the subgap leakage measurement.

Fig: 6.2 shows the experimental steps of the subgap leakage measurement. It takes about one week from the sample preparation step to the time when the first junction is fully tested.

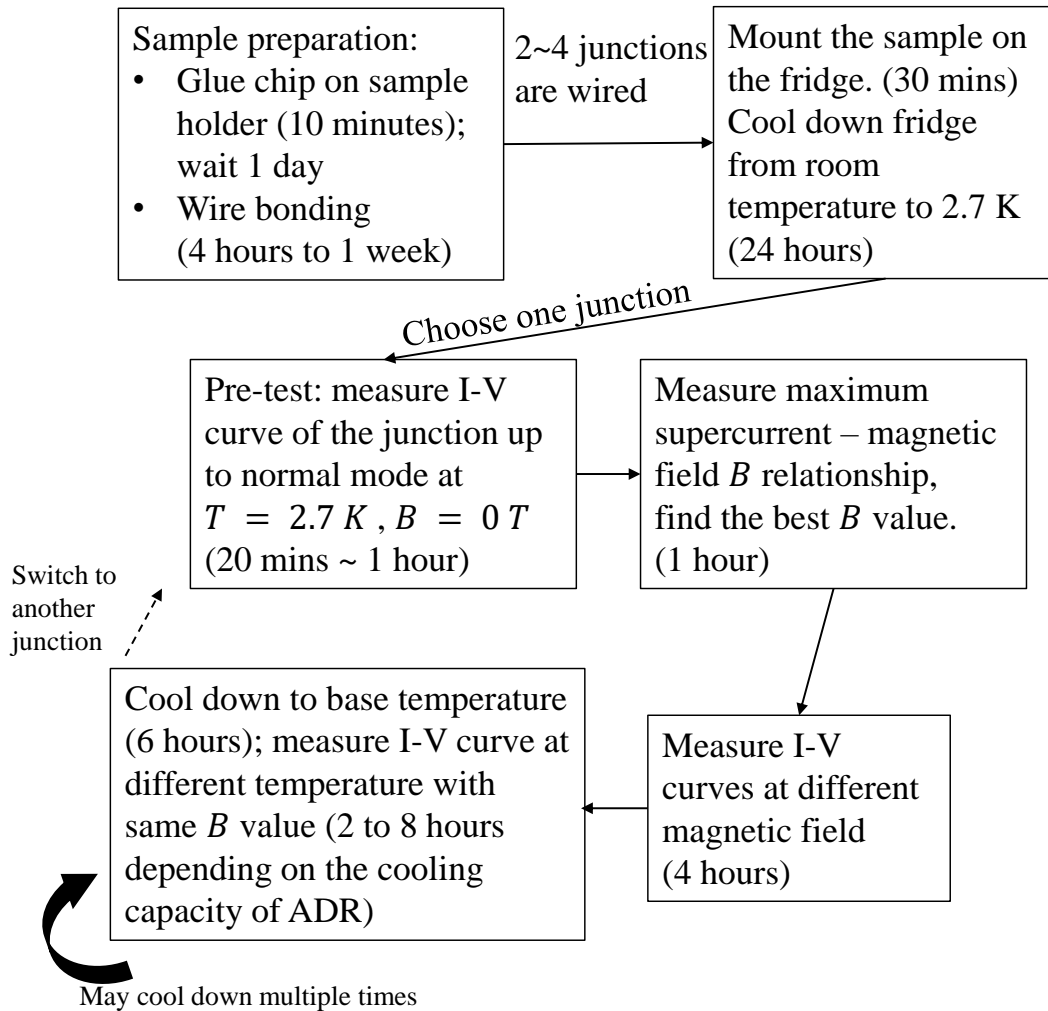


Figure 6.2: Experimental steps of subgap leakage measurement.

## 6.2 Current bias circuit

The current bias circuit is shown in Fig: 6.3. An SR 830 lock-in amplifier was used to provide the DC voltage source. By using the four-wire measurement, the junction voltage was amplified by a PAR 113 preamplifier with  $10\text{ M}\Omega$  input impedance and then be read by an Agilent 34401a multimeter. This setup was designed to characterize the I-V curves of the junctions whose subgap resistances are much smaller than the resistance of the current limiting resistor.

The sample holder cell was on the base temperature stage, which could be cooled down to  $50\text{ mK}$  in principle. In practice, the base temperature was  $130\text{ mK}$  due to the heat load on the cold stage. The sample holder. The sample holder was also at the center of a small made-in-house NbTi superconducting magnet which connected to the  $2.7\text{ K}$  stage. A heat switch connects the two stages. A Lakeshore germanium resistance thermometer(GRT) was on the base temperature stage and measures its temperature.

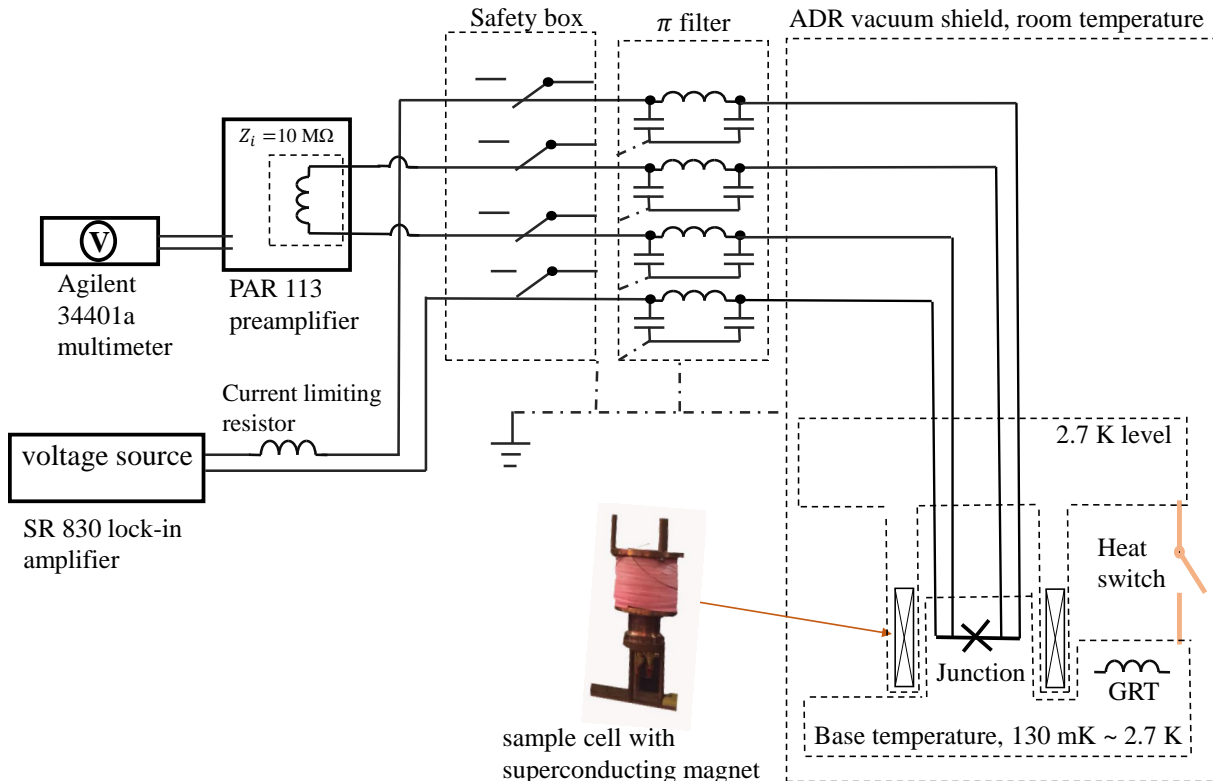


Figure 6.3: Current bias circuit of the subgap leakage measurement

**Safety box:** Josephson junctions can be destroyed by unexpected electronic spikes; therefore, a safety box with double pole double throw switches was installed to protect the junctions. During the experiment, the switches were opened, and the leads to the junction were floating; when not measuring the junction, the switches were closed, shortening the junction to the ground.

### 6.3 Voltage bias circuit

Fig: 6.4 is the voltage bias circuit. The SR 830 lock-in amplifier with a DC voltage divider was the voltage source. The junction current was measured by an Ithaco model 1211 preamplifier and an Agilent 34401a multimeter. The set up is designed to measure junctions with high subgap leakage resistance.

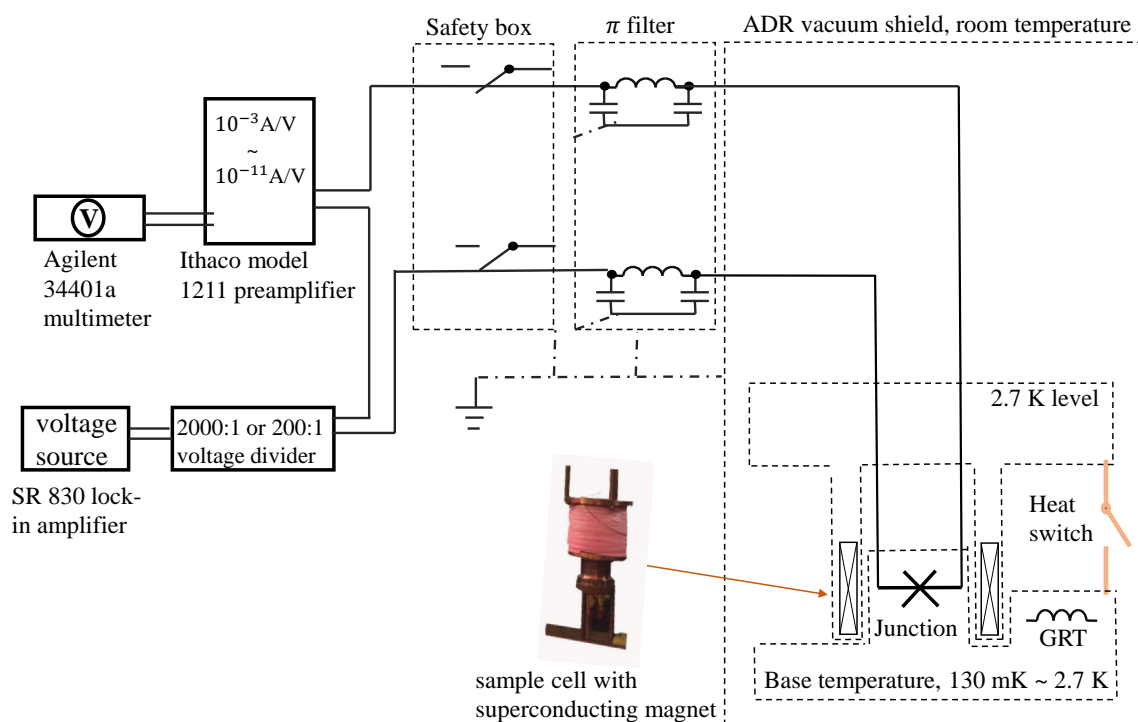


Figure 6.4: Voltage bias circuit of the subgap leakage measurement

### 6.3.1 Electrochemical effects

Electrochemical effects are parasitic effects in this case, where the measurement circuit is shorted by chemicals between two leads.[19] The electrochemical leakage current is typically on the level of  $10^{-8} \sim 10^{-13}$  A which may cause large noise in the low-level current measurement. In this measurement setup, the effects were caused by the dirty soldering flux on the switches of the safety box, shown in Fig: 6.5. This problem was solved by carefully performing soldering with a small amount of flux.

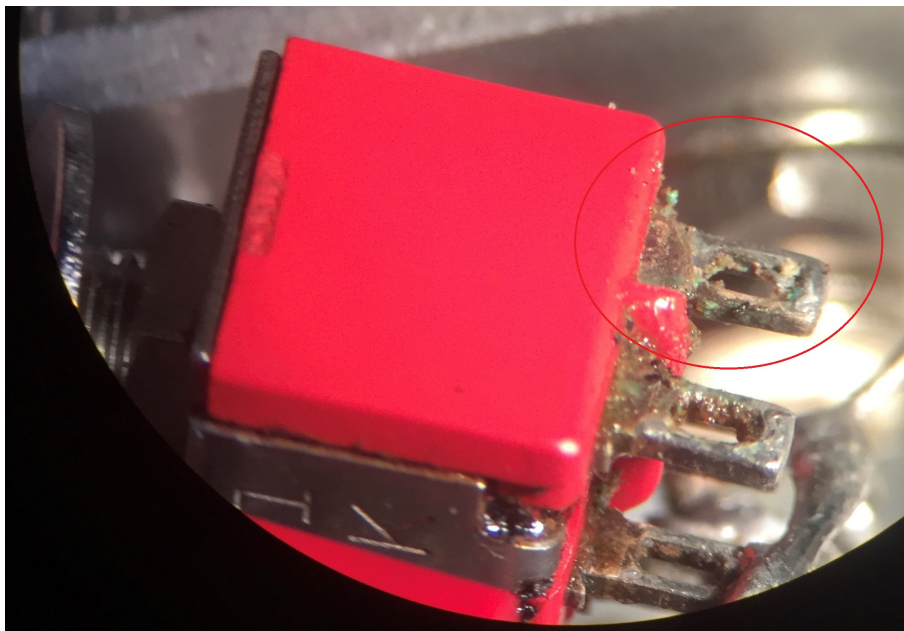


Figure 6.5: A dirty switch in the safety box covered by soldering flux. The red circle in the figure shows the dirty lead of the switch and the remaining flux

# Chapter 7

## Subgap leakage measurement: results and discussions

### 7.1 Current bias versus voltage bias

Junction JJ1-0.4um is a junction with the size of  $0.4 \mu m \times 0.4 \mu m$ . Fig: 7.1 are the I-V curves of the junction by using the current bias method, with  $T = 2.7 K$  and different magnetic fields. At  $B = 0 mT$ , the critical current  $I_c = 0.115 \mu A$ , the return current  $I_r = 5 nA$ , and  $\frac{2\Delta}{e} = 2.7 mV$ . The hysteresis I-V curves are typical for unshunted Josephson junctions. When increasing the magnetic field  $B$ ,  $I_c$  decreases and finally turns to zero when  $B = 68 mT$ ;  $\frac{2\Delta}{e}$  slightly decreases when increasing  $B$ .

Fig: 7.2 shows the I-V curves of the voltage bias method, using the same junction at  $T=2.7 K$ . The curves are not hysteretic as compared with those measured with current bias. The reason is that the bias current forces the junction to past the subgap region. When increasing the bias current, the junction is forced to turn to the high voltage region when its current is over the junction's critical current; when decreasing the bias current, the junction directly returns to the zero voltage stage when  $I < [I_c]$ . Therefore, if switching to the current bias method from the voltage bias method in a very short time, the I-V curves in Fig: 7.2 will follow the dash lines instead of the solid lines.

On the other hand, the voltage bias method can probe the subgap region. For example, the I-V curves of the voltage bias method show four current peaks (at 0 mV, 0.25 mV, 0.6 mV, and 1 mV), which are not observed by the current bias method. The highest peak corresponds to the largest supercurrent, while the reason causing the peaks are possibly due

to Andreev reflections. In conclusion, the voltage bias method is better than the current bias method when studying the subgap leakage current.

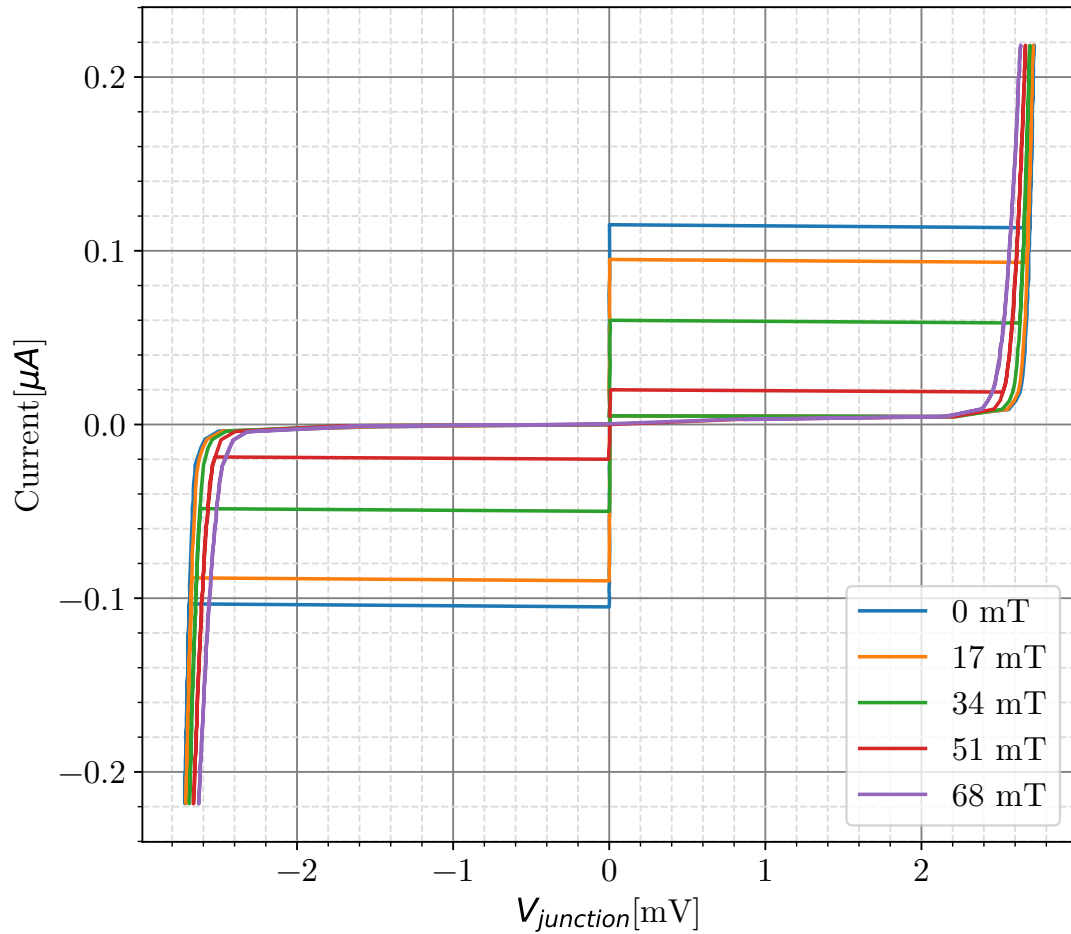


Figure 7.1: I-V curves of junction JJ1-0.4um at  $T = 2.7 K$  and different magnetic fields,  $B$ , measured by the current bias method. The curves are hysteretic. The critical current  $I_c$  decreases when increasing  $B$ .

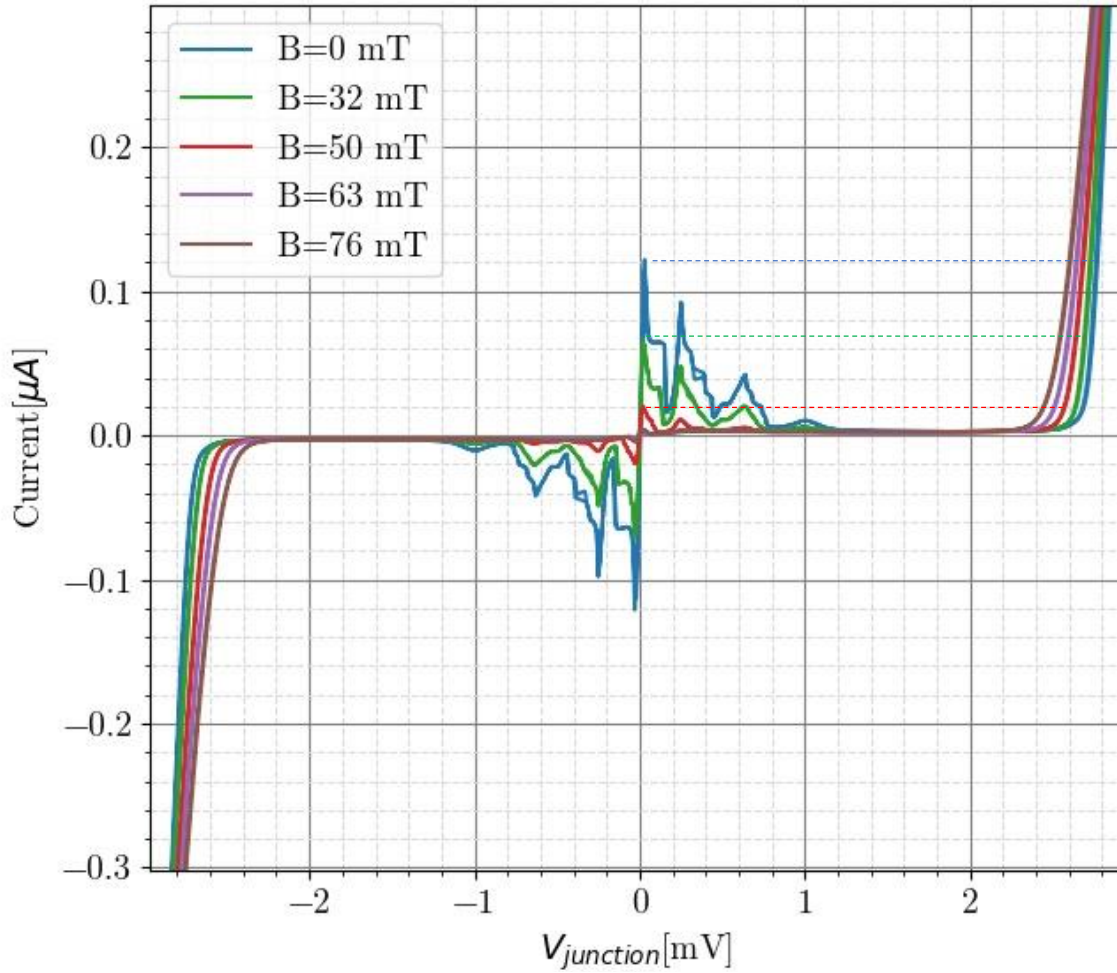


Figure 7.2: I-V curves of junction JJ1-0.4um at  $T = 2.7 K$  and different magnetic field, measured by the voltage bias method. The solid lines are from the experiment which are non-hysteresis. The dash lines are from the prediction of using current bias in the same experiment, which match the I-V curves in Fig: 7.1.

In Fig: 7.2, the  $I_c$  and  $I_{sg}$  turn from the  $\mu A$  level to the  $nA$  level when increasing  $B$ . The semi-log graph of I-V curves in Fig: 7.2 is then applied which helps to locate the smallest current, shown in Fig: 7.3. The smallest current is located at  $V = 2.0 mV$  which is  $2.6 nA$  and does not change much with changing  $B$ . Therefore, the subgap current of this junction is determined to be  $I_{sg} = 2.6 nA$  at  $T = 2.7 K$ .

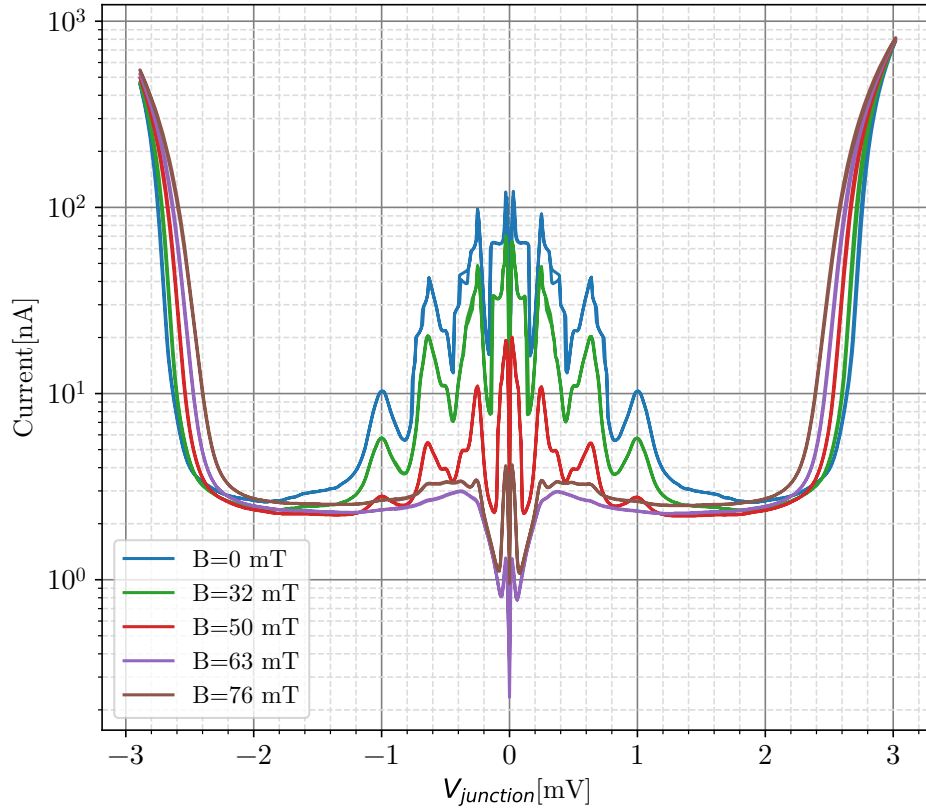


Figure 7.3: The log(I)-V curves of junction JJ1-0.4um at  $T = 2.7 K$  by using the voltage bias method, which use the same data of Fig: 7.2. It shows that the subgap current is the lowest near  $V_{junction} = 2.0 mV$ . When increasing the magnetic field, the height of the peaks decreases.

Similar to the method in Fig: 5.4, the normalized I-V curves of three junctions are shown in Fig: 7.4. Junction JJ0-0.7um and junction JJ0-1.0um behave as regular Josephson junctions. Notice that when increasing the bias voltage from 0 mV, their I-V curves behave as “load lines”. The reason is that the subgap resistance of the junctions is much smaller than the resistance of the signal wires. Junction JJ0-0.8um does not go into the normal state when  $eV > 2\Delta$ . This indicates that there are some serious defects in the junction.

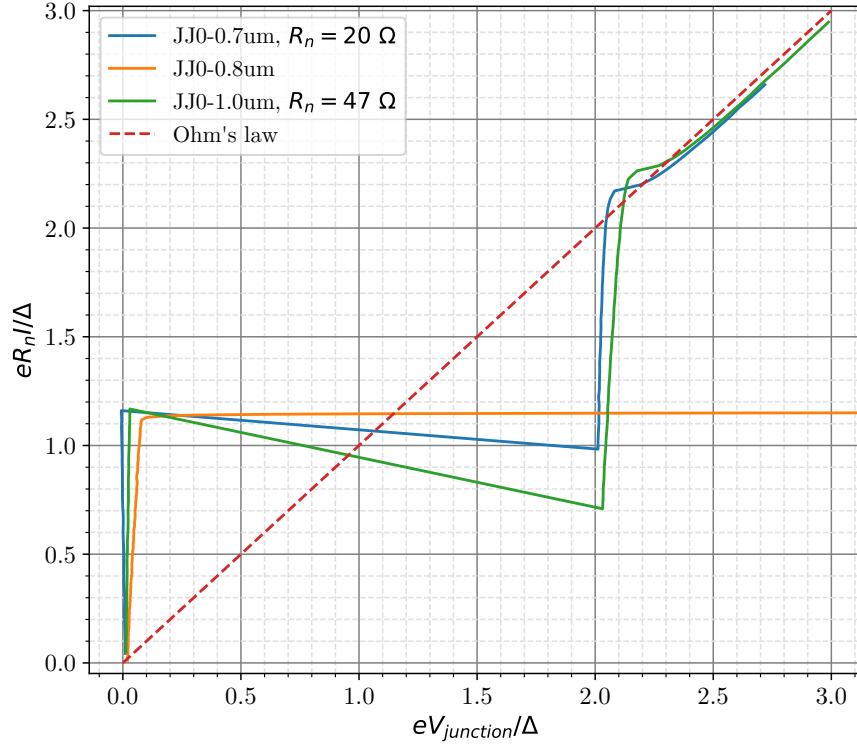


Figure 7.4: Normalized I-V curve of three Nb Josephson junctions on a same chip: junction-0.7um(blue), junction-0.8um(orange), and junction-1.0um(green). The curves are measured only when increasing the bias voltage  $V_{\text{junction}}$ . The red dashed line represents Ohm's law.  $T = 2.6 K$ ,  $B = 0 mT$ .

## 7.2 Magnetic suppression

The supercurrent can be suppressed by an external magnetic field. By measuring the maximum supercurrent when changing the magnetic field, the best fit value  $B_n$  can be found. By using Eq. 5.4 and Eq. 5.5,  $\Phi = (0.056 \mu m^2) \bullet B$  if the penetration depth is  $\lambda = 70 nm$ . The first smallest  $I_m(\Phi)$  corresponds to  $B_1=74 mT$ . The Fig: 7.5 is the experimental data for the maximum supercurrent of junction JJ1-0.4um at  $T = 2.7 K$ . The supercurrent is close to zero when the magnetic field is  $67 mT$ .

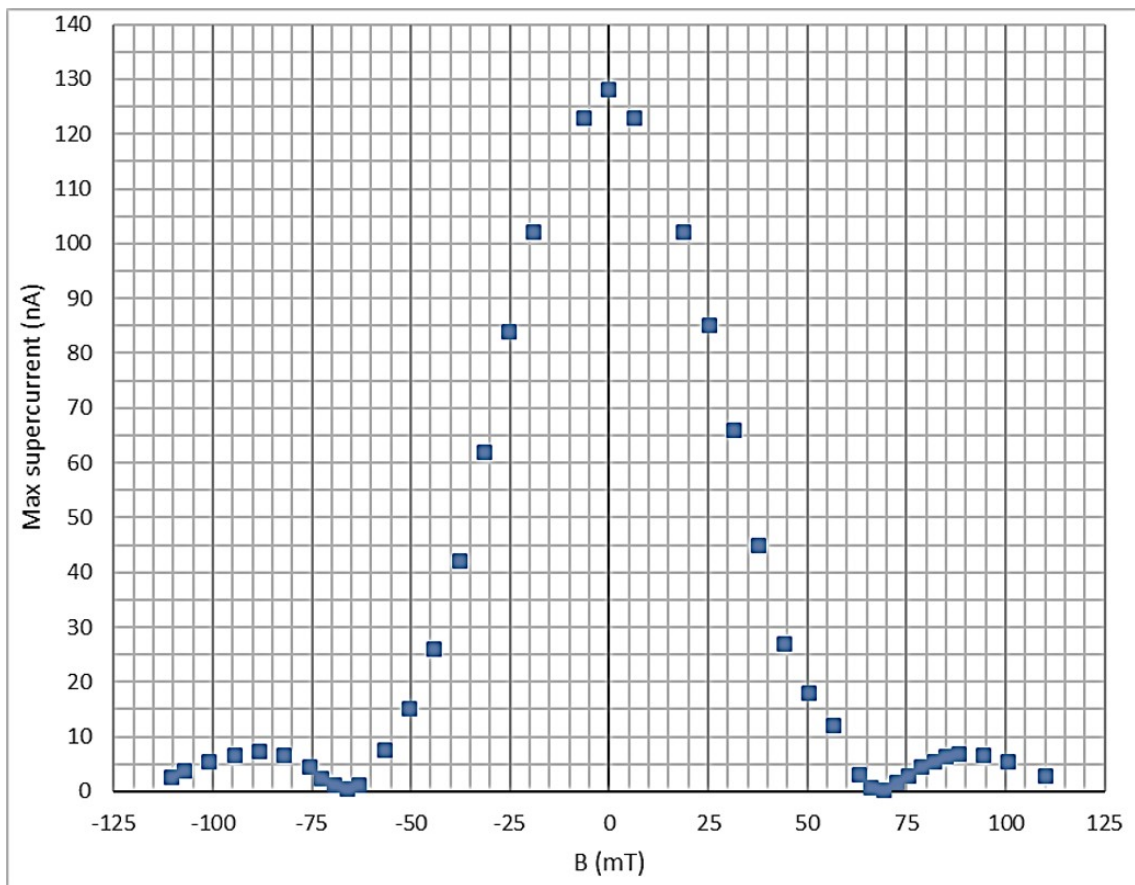


Figure 7.5: The maximum supercurrent of junction JJ1-0.4um at 2.7 K, changed by the applied magnetic field  $B$ .

Fig: 7.6 is the relationship between the maximum supercurrent and the magnetic flux applied to the junction. The experiment curve is from the result in Fig: 7.5; the calculation curve is based on Eq. 5.5. Both curves are symmetric along with the y-axis. The first smallest  $I(\Phi)/I(0)$  value is at  $\Phi/\Phi_0=2$  in the experiment which should be at  $\Phi/\Phi_0=1$  base on the calculation; however, the second smallest point of  $I(\Phi)/I(0)$  in experiment matches the third smallest  $I(\Phi)/I(0)$  point in calculation. Furthermore, the second-highest  $I(\Phi)/I(0)$  is 5% of the highest  $I(\Phi)/I(0)$  in the experiment, which does not match the calculation either. One explanation is the density of the tunneling current through the junction area was nonuniform.[5] Another more likely explanation is that the magnetic fields in the experiment were not accurate.

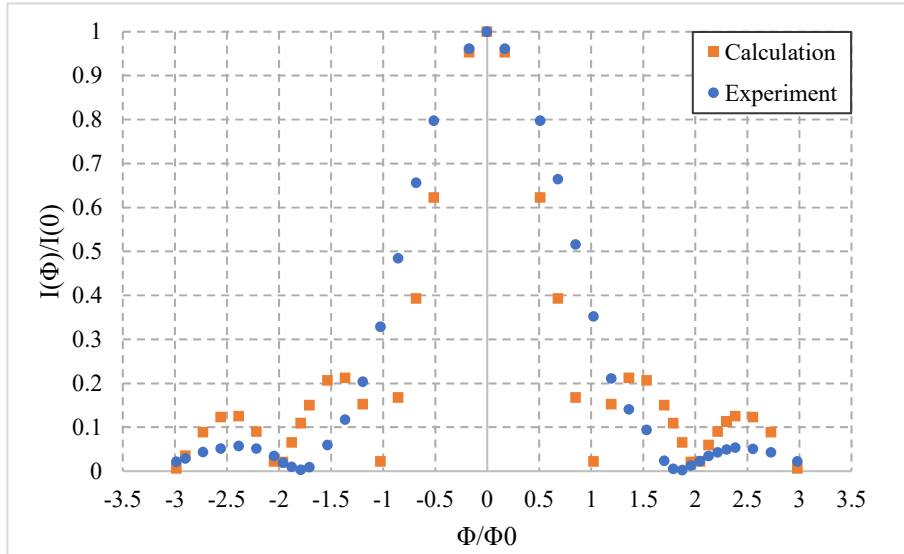


Figure 7.6: The relationship between the maximum supercurrent and the magnetic flux of junction JJ1-0.4um at  $T = 2.7K$ . The calculation is based on Eq. 5.5.

This characterization found the best fit  $B$  corresponding to the smallest possible supercurrent. By applying this magnetic field to the junction, the maximum subgap resistance  $R_{sg}$  may be obtained, and the I-V curves at the subgap region can be well characterized with the minimized supercurrent.

### 7.3 Temperature dependence

The Fig: 7.7 shows the I-V curves of junction JJ1-0.4um by the voltage bias method, at  $B=66 \text{ mT}$  and at different temperature. When the temperature is below  $1.0 \text{ K}$ , the curves are at similar positions with weak temperature dependence; when the temperature is higher than  $1.0 \text{ K}$ , the subgap region of the curves start to rise. The reason that the measured leakage current is temperature independent when  $T < 1.0 \text{ K}$  is the electrochemical effect of the soldering flux in the safety box. The external leakage resistance,  $R_{\text{ex}}$ , in this case was around  $160 \text{ M}\Omega$  which is much smaller than the  $R_{\text{sg}}$  of the junction. The problem was fixed by cleaning the safety box, which raised the  $R_{\text{ex}}$  to be over  $10 \text{ G}\Omega$ .

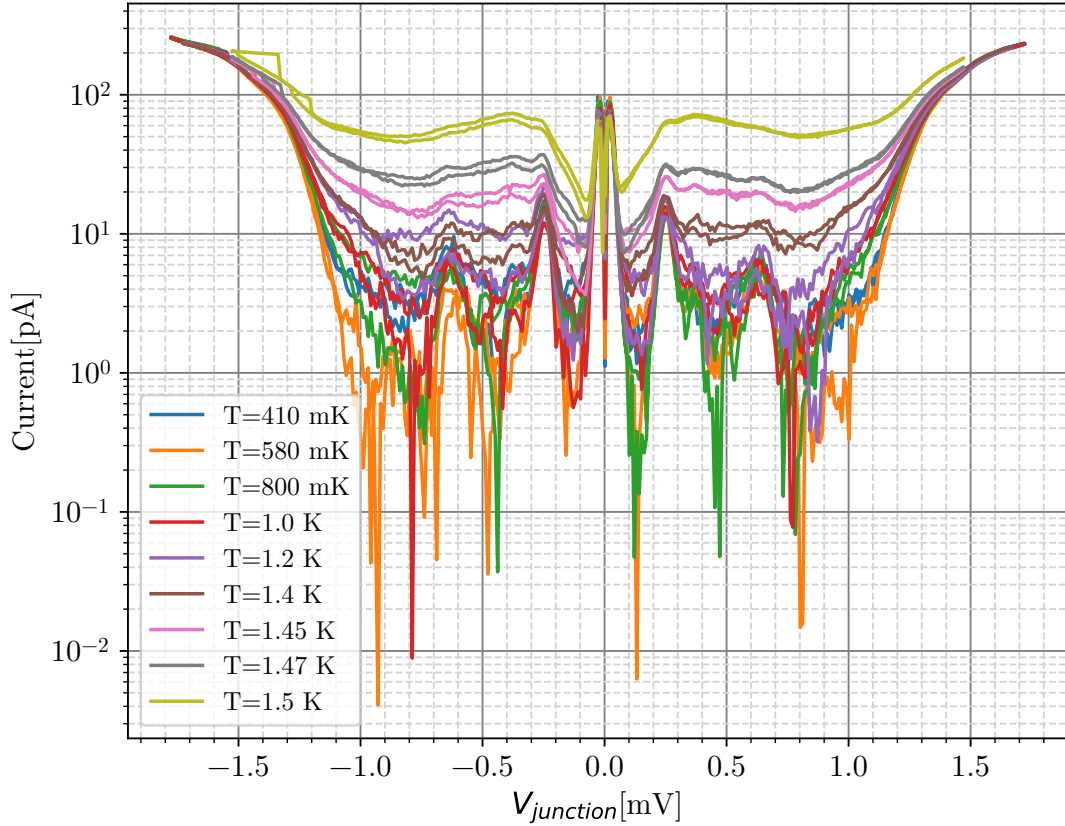


Figure 7.7: The I-V curves of junction JJ1-0.4um by voltage bias at  $B=66$  mT and different temperatures. The current at  $V_{junction} = 0.5$  mV was used to determine the subgap current,  $I_{sg}$ . It is seen to stay at the same level, 1 pA, when  $T < 1.0$  K; it is seen to increase along with temperature when  $T > 1.0$  K. The reason which causes peaks at  $V_{junction} = \pm 0.25$  mV and  $\pm 0.25$  mV is still not fully understood.

The I-V curves of another junction, junction JJ2-4um, were measured after fixing the electrochemical leakage problem. The results are shown in Fig: 7.8. The  $I_{sg}$  is as low as 0.1 pA when temperature is lower than 800 mK. Because of the capacity of the Ithaco preamplifier, the current below 0.1 pA cannot be measured.

$I_{sg}$  increases from 0.1 pA to 35 nA when raising temperature  $T$  from 520 mK to 1.75 K. However, the I-V curves show hysteresis in the loops only when  $T$  is below 1 K. Using the curve at  $T = 850$  mK (red) as an example: when increasing  $V_{junction}$  from 0.2 mV to 0.6 mV,  $I$  changes slowly from 0.1 pA to 1 pA and dramatically increases to 40 pA at  $V_{junction} = 0.6$  mV; when decreasing  $V_{junction}$  from 0.8 mV, the similar current transition is at  $V_{junction} = 0.45$  mV. It is still unclear what is the cause of the hysteresis.

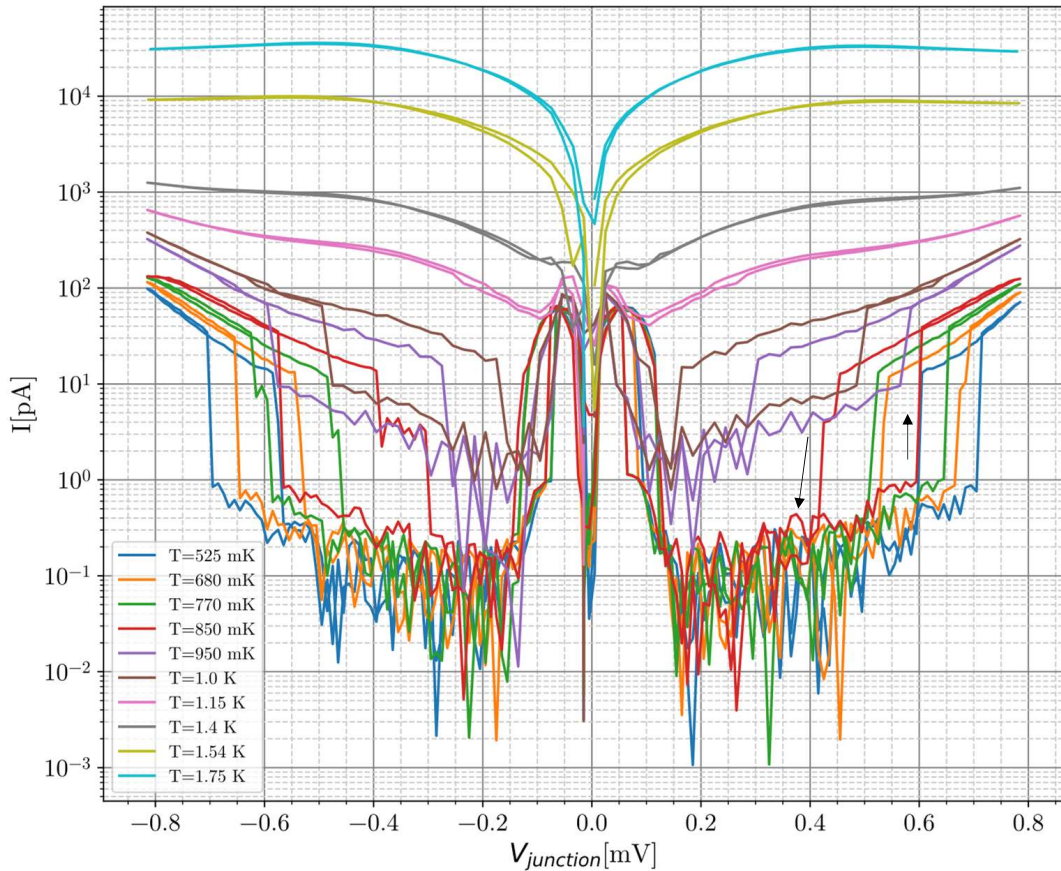


Figure 7.8: I-V curves of junction JJ2-4um by voltage bias at  $B=74$  mT and different temperature. The black arrows are the drift directions of the current along with the bias voltage method.

Since the  $R_{\text{sg}}$  was increasing when cooling down the sample, the temperature dependence of the normalized maximum subgap resistance  $R_{\text{J}}/R_{\text{n}}$  is shown in Fig: 7.9. When  $T > 1.0 \text{ K}$ , the curves follow the prediction of the BCS theory; when  $T < 1.0 \text{ K}$ , the subgap resistance of all three junctions approach to finite values. The possible reasons for this is the subgap leakage current of the junctions, or an the external leakage current is being seen, or the measured current has become smaller than the sensitivity of the current amplifier.

It should be pointed out that the temperature measurement was inaccurate when  $1.1 \text{ K} < T < 1.4 \text{ K}$  due to the superconducting transition of the aluminium frame connecting to the base temperature stage.

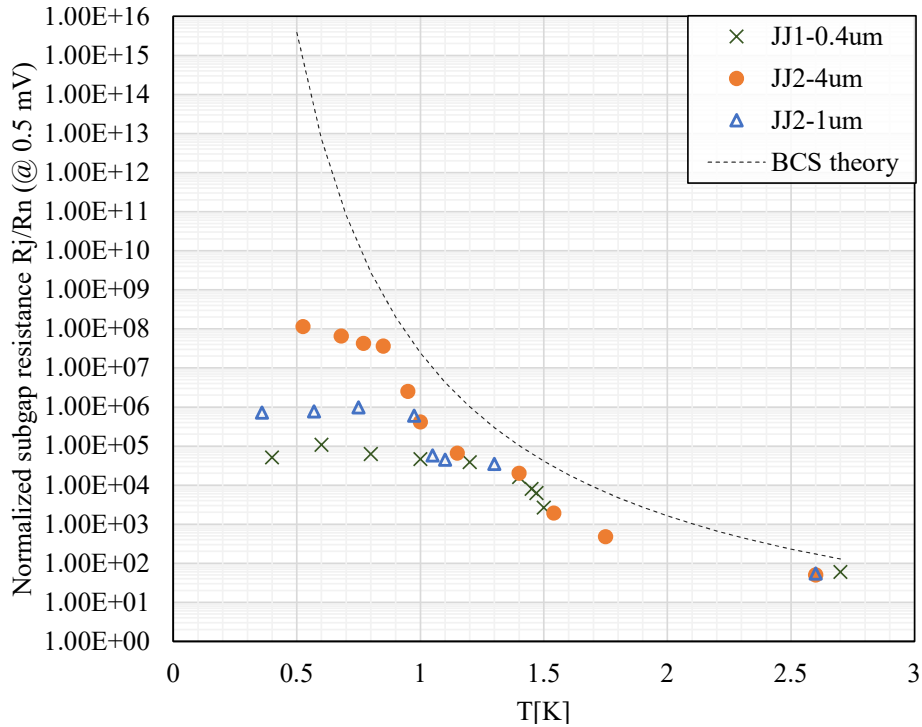


Figure 7.9: Temperature dependence curves of normalized subgap resistance of different junctions. Their trend follows the prediction of the BCS theory when  $T > 1.0 \text{ K}$ .

## 7.4 Summary

The goal was to test the quality of Josephson junctions from D-wave inc.. With the setup, the I-V curves and the low-level subgap leakage current of the junctions were characterized at low temperatures. The  $I_{\text{sg}}$  could be measured down to  $0.1 \text{ pA}$ ; the lowest available temperature of the setup was  $130 \text{ mK}$ .

Both the current bias method and the voltage bias method were used to measure the I-V curves. Because  $I_{\text{sg}}$  can be extremely small, the voltage bias method is preferred for the subgap leakage measurement.

The applied magnetic field  $B$  suppressed the supercurrent of the junctions so that large subgap resistance could be obtained with the best fit  $B$ . The supercurrent- $B$  relation and the  $I(\Phi)/I(0) - \Phi/\Phi_0$  relation were characterized.

The I-V curves of the junctions can directly show the current level; the normalized I-V curves such as  $R_n I - V$  curves and  $eR_n/\Delta - eV/\Delta$  are better for the comparison between samples. Junctions with intrinsic defects such as pinholes showed abnormal I-V curves, which can be easily distinguished from healthier junctions.

The I-V curves and the lowest  $I_{\text{sg}}$  showed their temperature dependence, and their trends followed the prediction of the BCS theory. However, some details of the I-V curves have not been fully explained.

## 7.5 Future work

The future work in the short term is to improve the measurement techniques. For now, only up to four junctions can be loaded at the same time, and it takes about one week to finish the characterization of one junction. Therefore, the first priority would be to improve the sample holder so that more samples could be loaded and tested together. The second work would be to replace the aluminum parts in the frame at the base temperature stage in order to fix the inaccurate temperature measurement problem when  $1.1 \text{ K} < T < 1.4 \text{ K}$ . The base temperature should be better characterized.

In the long term, the working mechanisms of Josephson junctions should be better understood. For example, the peaks at low bias voltage in Fig: 7.7 and the hysteresis loops in Fig: 7.8 have not been explained yet. More research work needs to be done on these.

# References

- [1] L. Adnane, A. Gokirmak, and H. Silva. High temperature Hall measurement setup for thin film characterization. *Review of Scientific Instruments*, 87(7):075117, 2016.
- [2] Vinay Ambegaokar and Alexis Baratoff. Tunneling between superconductors. *Phys. Rev. Lett.*, 10:486–489, 1963.
- [3] inc. Ametek advanced measurement technology. *Model 1900 precision low-noise signal transformer instruction manual*, 2002.
- [4] Ashoka Bali, Heng Wang, G. Jeffrey Snyder, and Ramesh Chandra Mallik. Thermoelectric properties of indium doped  $PbTe_{1-y}Sey$  alloys. *Journal of Applied Physics*, 116(3):033707, 2014.
- [5] Antonio Barone. *Physics and applications of the Josephson effect*. A Wiley-Interscience publication. Wiley, New York ; Toronto, 1982.
- [6] Isil Berkun. *High temperature Hall effect measurement system design, measurement and analysis*. PhD thesis, 2015. Copyright - Database copyright ProQuest LLC.
- [7] M.F Bocko, A.M Herr, and M.J Feldman. Prospects for quantum coherent computation using superconducting electronics. *IEEE Transactions on Applied Superconductivity*, 7(2):3638–3641, 1997.
- [8] Daniel M. Boerger, John J. Kramer, and Larry D. Partain. Generalized Hall–effect measurement geometries and limitations of van der Pauw–type Hall–effect measurements. *Journal of Applied Physics*, 52(1):269–274, 1981.
- [9] Kasper A. Borup, Eric S. Toberer, Leslie D. Zoltan, George Nakatsukasa, Michael Errico, Jean-Pierre Fleurial, Bo B. Iversen, and G. Jeffrey Snyder. Measurement of the electrical resistivity and Hall coefficient at high temperatures. *Review of Scientific Instruments*, 83(12):123902, 2012.

- [10] C.L. Chien and C.R. Westgate. The Hall effect and its applications. New York, 1980. Johns Hopkins University, Plenum Press.
- [11] McMaster-Carr Supply Company. Spring test probes.
- [12] T Greibe. Improvement of chip design to reduce resonances in subgap regime of Josephson junctions. *Journal of Physics: Conference Series*, 150(5), 2009.
- [13] Tine Greibe, Markku P V Stenberg, C M Wilson, Thilo Bauch, Vitaly S Shumeiko, and Per Delsing. Are "pinholes" the cause of excess current in superconducting tunnel junctions? a study of andreev current in highly resistive junctions. *Physical review letters*, 106(9), 2011.
- [14] M. A. Gubrud, M. Ejrnaes, A. J. Berkley, R. C. Ramos, I. Jin, J. R. Anderson, A. J. Dragt, C. J. Lobb, and F. C. Wellstood. Sub-gap leakage in  $Nb/AlO_x/Nb$  and  $Al/AlO_x/Al$  Josephson junctions. *IEEE Transactions on Applied Superconductivity*, 11(1):1002–1005, 2001.
- [15] Murat Gunes, Hisanori Sato, Loreynne Pinsard-Gaudart, David Berardan, and Nita Dragoë. Aversatile system for Hall effect measurements at high temperature. *Measurement Science and Technology*, 28(10):8, 2017.
- [16] R. Harris, J. Johansson, A. J. Berkley, M. W. Johnson, T. Lanting, Siyuan Han, P. Bunyk, E. Ladizinsky, T. Oh, I. Perminov, E. Tolkacheva, S. Uchaikin, E. Chapple, C. Enderud, C. Rich, M. Thom, J. Wang, B. Wilson, and G. Rose. Experimental demonstration of a robust and scalable flux qubit. *Superconductor Science and Technology*, 23(6):065004, 2010.
- [17] M. Hidaka, S. Nagasawa, T. Satoh, and K. Hinode. Defects of  $Nb/AlO_x/Nb$  Josephson junctions caused by underneath fine particles. pages 1–3, 2015.
- [18] Paul Horowitz. *The art of electronics*. Cambridge University Press, Cambridge, third edition. edition, 2015.
- [19] Keithley Instruments. *Low level measurements: precision DC current, voltage, and resistance measurements*. Keithley Instruments, Cleveland, OH, 4th edition, 1993.
- [20] EG&G instruments Corporation. *Model 113 Low noise preamplifier instruction manual*, 1990.

- [21] Parisa Jafarzadeh, Abdeljalil Assoud, Daniel Ramirez, Nader Farahi, Tianze Zou, Eckhard Mller, Jan B. Kycia, and Holger Kleinke. Thermoelectric properties and stability of  $Ba_3Cu_{16-x}Se_{11-y}Te_y$ . *Journal of Applied Physics*, 126(2):025109, 2019.
- [22] Parisa Jafarzadeh, Maegan R. Rodrigues, Yixuan Shi, Abdeljalil Assoud, Tianze Zou, Jan B. Kycia, and Holger Kleinke. Effect of mixed occupancies on the thermoelectric properties of  $BaCu_{6-x}Se_{1-y}Te_{6+y}$  polychalcogenides. *Dalton Trans.*, 48:9357–9364, 2019.
- [23] A. W. Kleinsasser, W. H. Mallison, R. E. Miller, and G. B. Arnold. Electrical characterization of Nb/Al-oxide/Nb Josephson junctions with high critical current densities. *IEEE Transactions on Applied Superconductivity*, 5(2):2735–2738, 1995.
- [24] K.M Lang, S Nam, J Aumentado, C Urbina, and J.M Martinis. Banishing quasiparticles from Josephson-junction qubits: why and how to do it. 13(2):989–993, 2003.
- [25] Thanh Phong Le. Hall effect measurement on thermoelectric materials. Fourth year undergraduate student research project report, 2015.
- [26] Min Ho Lee, Jae Hyun Yun, Kyunghan Ahn, and Jong-Soo Rhyee. Thermoelectric properties and chemical potential tuning by Cu-doping in n-type ionic conductors  $Cu_xAg_{2-x}Se_{0.5}Te_{0.5}$ . *Journal of Physics and Chemistry of Solids*, 111:214 – 218, 2017.
- [27] Sang Kyung Lee, Chang Goo Kang, Young Gon Lee, Chunhum Cho, Eunji Park, Hyun Jong Chung, Sunae Seo, Hi-Deok Lee, and Byoung Hun Lee. Correlation of low frequency noise characteristics with the interfacial charge exchange reaction at graphene devices. *Carbon*, 50(11):4046,4051, 2012-09.
- [28] L.R. Macario, Y. Shi, P. Jafarzadeh, T. Zou, J.B. Kycia, and H. Kleinke. Thermoelectric and mechanical properties of environmentally friendly  $Mg_2Si_{0.3}Sn_{0.67}Bi_{0.03}/SiC$  composites. *ACS Applied Materials and Interfaces*, 11(49):45629–45635, 2019.
- [29] S. Maggi, N. De Leo, M. Fretto, V. Lacquaniti, A. Agostino, and P. Verhoeve. Superconducting tunnel junction x-ray detectors with ultra-low subgap current. In *2007 2nd International Workshop on Advances in Sensors and Interface*, pages 1–6, 2007.
- [30] John Martinis. Superconducting phase qubits. *Quantum Information Processing*, 8(2):81–103, 2009.
- [31] F. P. Milliken, R. H. Koch, J. R. Kirtley, and J. R. Rozen. The subgap current in  $Nb/AlOx/Nb$  tunnel junctions. *Applied Physics Letters*, 85(24):5941–5943, 2004.

- [32] Alan S. Morris. *Measurement and instrumentation theory and application*. Academic Press, Waltham, MA.
- [33] C. D. Motchenbacher and J. A. Connelly. *Low-noise electronic system design*. Wiley-Interscience publication. J. Wiley Sons, New York ; Toronto, 1993.
- [34] V. Patel, Wei Chen, S. Pottorf, and J. E. Lukens. A fast turn-around time process for fabrication of qubit circuits. *IEEE Transactions on Applied Superconductivity*, 15(2):117–120, 2005.
- [35] Plesha, Clifford. Setup and design of a cryogenic testing station with focus on characterization of superconducting devices. Master’s thesis, University of Waterloo, 2019.
- [36] Everett Charles Technology Contact Products.
- [37] E.H Putley. *The Hall Effect and Semi-Conductor Physics*. New York, Dover Publications (1968), 1968.
- [38] N. Rando, P. Videler, A. Peacock, A. van Dordrecht, P. Verhoeve, R. Venn, A. C. Wright, and J. Lumley. Transmission electron microscopy and atomic force microscopy analysis of nbalaloxnb superconducting tunnel junction detectors. *Journal of Applied Physics*, 77(8):4099–4106, 1995.
- [39] Friederike Reissig, Barbara Heep, Martin Panthfer, Max Wood, Shashwat Anand, G. Jeffrey Snyder, and Wolfgang Tremel. Effect of anion substitution on the structural and transport properties of argyrodites  $Cu_7PSe_{6x}S_x$ . *Dalton Trans.*, 48:15822–15829, 2019.
- [40] Standard research Systems. *MODEL SR830 DSP Lock-In Amplifier*, 2011.
- [41] Robert E Simpson. *Introductory electronics for scientists and engineers*. Allyn and Bacon, Boston, 2nd edition, 1987.
- [42] G. Jeffrey Snyder and Eric S. Toberer. Complex thermoelectric materials. *Nature Materials*, 7(2), 2008.
- [43] Dawn Tilbury and Bill Messner. *PID Control*. National Instrument tutorial website, 2012.
- [44] Michael Tinkham. *Introduction to superconductivity*. Dover Publications, Mineola, N.Y., second edition. edition, 2004.

- [45] Theodore Van Duzer. *Principles of superconductive devices and circuits*. Elsevier, New York, 1981.
- [46] Bernd Wölfing, Christian Kloc, Jens Teubner, and Ernst Bucher. High performance thermoelectric  $Tl_9BiTe_6$  with an extremely low thermal conductivity. *Phys. Rev. Lett.*, 86:4350–4353, 2001.

# Glossary

**ADR** Adiabatic demagnetization refrigerator [79](#)

**CMRR** Common mode rejection ratio [28](#)

**EMF** electromotive force [6](#)

**NF** Noise figure [30](#)

**NPLC** Number of power line cycles [47](#)

**RMS** Root mean square [24](#)

**VDP** Van der Pauw [6](#)